Coherent X-ray Studies of Non–Equilibrium Processes

Andrei Fluerasu

Centre for the Physics of Materials
Department of Physics, McGill University
Montréal, Québec

A thesis submitted to the
Faculty of Graduate Studies and Research
in partial fulfillment of the requirements for the degree of
Doctor of Philosophy

2003/11/10

Library and
Archives Canada

Published Heritage
Branch

395 Wellington Street
Ottawa ON K1A 0N4
Canada

Bibliothèque et
Archives Canada

Direction du
Patrimoine de l'édition

395, rue Wellington
Ottawa ON K1A 0N4
Canada

Your file Votre référence
ISBN: 0-612-98253-X
Our file Notre référence
ISBN: 0-612-98253-X

NOTICE:
The author has granted a non-exclusive license allowing Library and Archives Canada to reproduce, publish, archive, preserve, conserve, communicate to the public by telecommunication or on the Internet, loan, distribute and sell theses worldwide, for commercial or non-commercial purposes, in microform, paper, electronic and/or any other formats.

The author retains copyright ownership and moral rights in this thesis. Neither the thesis nor substantial extracts from it may be printed or otherwise reproduced without the author's permission.

AVIS:
L'auteur a accordé une licence non exclusive permettant à la Bibliothèque et Archives Canada de reproduire, publier, archiver, sauvegarder, conserver, transmettre au public par télécommunication ou par l'Internet, prêter, distribuer et vendre des thèses partout dans le monde, à des fins commerciales ou autres, sur support microforme, papier, électronique et/ou autres formats.

L'auteur conserve la propriété du droit d'auteur et des droits moraux qui protège cette thèse. Ni la thèse ni des extraits substantiels de celle-ci ne doivent être imprimés ou autrement reproduits sans son autorisation.

In compliance with the Canadian Privacy Act some supporting forms may have been removed from this thesis.

While these forms may be included in the document page count, their removal does not represent any loss of content from the thesis.

Conformément à la loi canadienne sur la protection de la vie privée, quelques formulaires secondaires ont été enlevés de cette thèse.

Bien que ces formulaires aient inclus dans la pagination, il n'y aura aucun contenu manquant.

Canada

To,

Cezar, from whom I always tried to learn the art of clear thinking
Corina, from whom I always tried to learn the art of sound thinking
Anca, for being the person who understands me best

and

Meme, for her love

Résumé

La spectroscopie des fluctuations d'intensité avec des rayons X cohérentes est une technique qui permet de mesurer la dynamique des fluctuations dans les solides. Depuis son invention, cette technique a été utilisée pour étudier la dynamique des fluctuations d'intensité dans plusieurs systèmes à l'equilibre. Dans cette thèse, nous avons utilisé la diffraction des rayons X coherentes pour étudier la dynamique d'un système hors d'equilibre. En particulier, nous nous sommes focalisé sur la transition de phase ordre-désordre dans l'aliage Cu_3Au. Ce dernier est un cas typique pour une transition de phase de première espece avec parametre d'ordre non-conservé (modèle A). Les experiences decrites dans cette thèse sont les premieres mesures quantitatives de la dynamique des fluctuations dans un tel système. Nos résultats ont confirmé les prédictions théorique pour un système de type "modèl A". Les fluctuations temporelles des patrons de diffractions tachetés (speckles), c'est a dire les fonctions de corrélations des fluctuations d'intensité à deux temps t_1 et t_2, sont bien déctrites par une lois d'échelle qui dépend non seulement de la différence $|t_1 - t_2|$, comme dans un système en état d'équilibre, mais aussi du temps moyen, $\bar{t} = \frac{t_1+t_2}{2}$. En même temps, on a montré que des déviations à cette lois d'échelle étaient présentes au début de la transition.

Pour étudier la physique des systèmes hors d'équilibre, un bon controlleur de temperature est souvant requis. Pour déclancher la transition de phase, la temperature doit etre changée par des centaines de degrées dans les plus bref delais, en évitant, en même temps, tout oscillation autour de la valeure finale. Pour cette raison, on a construit un controleur de temperature de type "KPPID", basé sur un algorithme de feedback de type PID, sur des calcules thermiques et sur une technique de type "filtre Kalman" pour le filtrage du bruit. Le controlleur de temperature "KPPID" a été mis en place à Argonne National Laboratories et a été utilisé avec succes dans les éxperiences decritent dans cette thèse.

Abstract

X-ray Intensity Fluctuation Spectroscopy (XIFS) is an ideal technique to perform measurements on the dynamics of fluctuations in condensed matter systems. Over the past few years, XIFS has been used in several studies of dynamics in both hard condensed matter and soft condensed matter equilibrium systems. Its extension to study the dynamics of non-equilibrium systems is currently under way. In this thesis, we present the first applications of XIFS to study dynamics during a first order phase transition with non-conserved order parameter (model A). The order-disorder phase transition in the binary alloy Cu_3Au has been chosen as a case study for such a non-equilibrium process and has been studied using XIFS. Our experiments have confirmed the theoretical predictions for the scaling laws describing the evolution of the density-density correlation functions, which are measured by the autocorrelation function of the scattered intensity. The covariance of the scattered intensity was found to be proportional with scaling functions with natural variables $\delta t = |t_1 - t_2|$ and $\bar{t} = \frac{t_1+t_2}{2}$, as predicted by theory. However, some significant early-time deviations from this scaling picture have been observed and are currently under investigations.

In order to study non-equilibrium processes in condensed matter systems, a very precise and fast temperature control system is often required. In order to trigger the particular process under study and to obtain meaningful experimental data, the temperature has to change by hundreds of degrees in very short times, while completely avoiding any over/under shooting. To achieve this, we designed and implemented a computer-controlled temperature tracking system which combines standard Proportional-Integral-Derivative (PID) feedback, thermal modeling and finite difference thermal calculations (feedforward) and Kalman filtering of the temperature readings in order to reduce the noise. The resulting Kalman-Predictive-Proportional-Integral-Derivative (KPPID) algorithm allows us to obtain accurate control, to minimize the response time and to avoid over/under shooting, even in systems with inherent noisy temperature readings and time delays. The KPPID temperature controller was successfully implemented at the Advanced Photon Source at Argonne National Laboratories and was used to perform the coherent X-ray diffraction experiments described in this thesis.

Acknowledgments

When I rock-climb, reaching the top of the route or the summit is only part of the thrill. And it is not even the most important one. After all, reaching the top of the climb is only a moment between two climbs. What I always felt was more important is the process; the journey between the base of the cliff and the drive back home. As I write this Acknowledgments section of my Ph.D. thesis, I find myself feeling the same about this research. The answer to "why I did it" lies somewhere between the first discussions I had with Mark Sutton, my supervisor, when I arrived at McGill four years ago, and the current attempts to fix the last details of this manuscript. And my thoughts at this moment go to all the people who, in one way or another, helped me during this process. Despite the hardships, it's largely due to them that I feel now good about the journey and even feel I would like to go further.

I was very fortunate to work not only with an expert in the experimental technique I used in this research, but with the person who actually invented it. But in the end, I think the most important things that I tried to learn from Mark reach far beyond the subtleties of a particular experimental technique, following his great intuition about the physics of materials or mining his vast knowledge of Unix and computers in general. This very important and inspiring things are Mark's passion for what he is doing, for our research, and his continuous search for simple and clear pictures supported by experimental results that are beyond any doubt. These lessons I'll take with me in my future journeys and for this I wish to thank Mark.

The McGill Physics Department provides an extremely nice environment to work in. Many formal or informal meetings and discussions between students and professors, experimentalists and theorists, high energy physicists or astrophysicists and material scientists, all encourage and maintain a high level of passion in the department. In particular I benefited from many discussions with my colleagues Khosrow, Khalid, Jean-Francois and Frédéric and I often used programs written by them in my data analysis. During my stay at McGill Zaven Altounian has been a constant support and friend, and his advice on my research, teaching, or life as a graduate student in general were always helpful. Juan and Paul provided me and everybody else in the department with great IT support. Whether I was stuck in a bug trying to write a driver for our new data acquisition card or was lost trying to install Linux on my laptop, they always provided extremely competent and almost immediate support. So did Paula when I was befuddled by administrative issues.

Much of my current balance, of what I am and most importantly, of what I would like to become, is related to my friends. It is impossible for me to imagine my life in Montreal and implicitly what this research would have been like without them. They are my friends, the "climbers"; Bruce, Elaine, Mike, Simon, Brian, Christiane, Rachel, Sebastien, Nathan, Jim, Scott... Thanks for keeping me "on belay"! And they are my friends the "tangueros"; the teachers, Antonio, Luce and Mary-Ann, who shared their knowledge with love and passion, and the very special people I so much enjoyed dancing with, Marie, Kim, Karen, Elizabeth, Johanne... Thanks for sharing that undescribable tango something...

And there are other with whom I danced, I climbed, I laughed, I talked about past, future, physics or hydrology. Thanks April for being such a good friend! Thanks for keeping your head on your shoulders. It's a good example to follow!

Thanks Dave and Lyn, for sharing or having shared an apartment with me, for sharing many stories and for being the friends you are! It's largely due to you that now I call Montreal a second home. On top of everything, you are also my best English teachers. Thanks Dave for helping me, among so many other things, with proof reading my thesis.

The hardest thing when I left Romania 8 years ago to come to North America for graduate studies was to leave my friends behind. In the end it turned out that in some sense, the distance has become smaller than it seemed at that time. Now we are all in the "new world" within 1500 km from each other. Thank you Radu, Matei for your friendship and for being there. Thank you for worrying for me! Anda is one of these persons I could thank for so many things, from great vacations to many meaningful discussions ... Thanks Anda for being!

Last but not least, I am grateful to my dear ones, my sister Anca and our parents Cezar and Corina, for being there, for constantly supporting us. I'm aware that it's you, C&C who suffered the most, with both of us so far away. I can only hope it was worthwhile and I will try to do my best to make it so.

Contents

List of Figures

List of Tables

Chapter 1

Introduction

For more than a century, since their discovery by Röntgen in 1895, X-rays have been an invaluable probe into the structure of condensed matter at atomic length scales. With the advent of the so-called third-generation synchrotron sources, many new types of X-ray experiments have become possible in the last decade. Most of these studies take advantage of the high brilliance of the synchrotron sources. Compared to "standard", laboratory X-ray tubes, a modern synchrotron radiation facility is a factor of 10^{12} times brighter [1]. Another important advantage of synchrotron radiation is its relatively high degree of coherence [15, 37]. When coherent radiation illuminates a condensed-matter system, the scattered intensity is determined by the exact configuration of the system. Mathematically stated, intensity scattered by a wavevector $\mathbf{Q}$ is proportional to the exact structure factor of the scatterer

$$I_{coh}(\mathbf{Q},t) \sim S(\mathbf{Q},t). \tag{1.1}$$

In contrast, a scattering experiment with "conventional" (incoherent) X-rays provides information only about a configurational average of the exact structure factor. Mathematically, this can be written

$$I_{incoh} \sim \langle S(\mathbf{Q},t)\rangle, \tag{1.2}$$

where $\langle\rangle$ denotes an ensemble average over all the possible configurations. In other words, incoherent radiation is incapable of "seeing" fluctuations in the structure factor $S(\mathbf{Q},t)$.

As a consequence, if coherent radiation is scattered by a system, a graininess in the scattered intensity, called speckle, is observed. The scattered radiation is the superposition of the average or incoherent scattered intensity $\langle I(\mathbf{Q},t)\rangle$ and the speckles due to the diffuse scattering from the randomly distributed disorder present in the system. Sutton et. al. [60], first demonstrated that one can get sufficient coherent flux from high-brilliance synchrotron X-ray sources to observe speckle patterns in the radiation scattered by systems which contain some randomness. Specifically, they have observed speckle patterns in the diffraction of coherent X-rays from randomly distributed antiphase domains in a single crystal of the binary alloy Cu_3Au (Fig. 1.1 [60]).

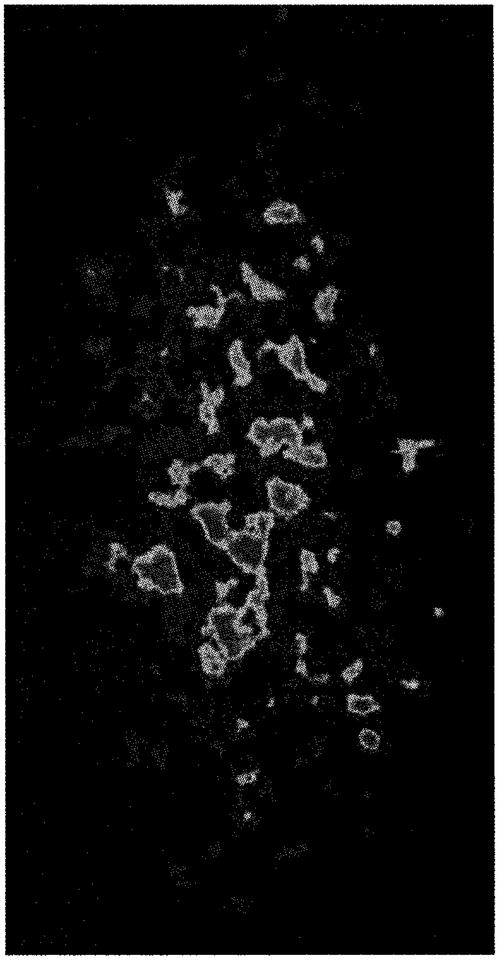

Fig. 1.1 Speckle pattern in the diffuse scattering from randomly distributed antiphase domain walls in a Cu_3Au single crystal (from [60]).

Speckle is an effect often seen with laser light and was at the basis of the development of a technique called Intensity Fluctuation Spectroscopy (IFS) or Dynamic Light Scattering [14]. IFS with laser light has long been employed to investigate the dynamics of transparent condensed matter systems on micrometer length scales. A sample is illuminated with coherent light, resulting in a speckle pattern which varies in time as the sample undergoes thermal fluctuations. The time autocorrelation of the speckle pattern yields information about the dynamics of thermal fluctuations and the characteristic times involved [53].

Over the past few years, the IFS technique has been transfered to the X-ray range and has been applied to study the dynamics of fluctuations in condensed matter systems at atomic length scales by using scattering with partially coherent X-rays obtained from third-generation synchrotron sources. The technique is usually referred to as X-ray Intensity Fluctuation Spectroscopy (XIFS) or X-ray Photon Correlation Spectroscopy (XPCS). Investigations of dynamic properties in equilibrium systems such as a metallic alloy near a second order phase transition by Brauer et. al. [7] or a fractal aggregate composed of small Pd particles by Thurn-Albrecht et. al. [63] have demonstrated the power of XIFS.

An even more recent direction of research is the use of XIFS to study dynamical properties of non-equilibrium systems. In such a system, not only the speckle pattern fluctuates in time, but also the average scattered intensity changes as a result of the process taking place. The time evolution of the speckle pattern from a Cu_3Au sample undergoing an order-disorder phase transition is shown in Fig. 1.2.

The development of long-range order out of a disordered system is a well studied class of non-equilibrium processes. In particular binary metallic alloys are very well suited systems to be studied by XIFS. The photon counting statistics can be enhanced by measuring fluctuations in the speckle pattern around Bragg peaks (as it was done in the experiments shown in Fig. 1.2) and structural phase transition such as order-disorder transitions or phase separation are easily detected by X-ray scattering techniques. Such processes are most typically triggered by temperature quenches and involve first order phase transitions associated with the sudden apparition of phases characterized by long-range order (i.e. discontinuities of the order parameter and other extensive parameters).

The theoretical foundations of XIFS with non-equilibrium phenomena have been understood for systems undergoing first order phase transitions with both non-conserved order parameter (NCOP) [9] and conserved order parameter (COP) [10]. However, experimental evidence for the proposed scaling laws describing the dynamics of fluctuations have been obtained only for first order phase transition with COP [44, 38]. This thesis reports the first experimental study and the first experimental confirmation of the proposed theory for XIFS in a system undergoing a first order phase transition with NCOP.

In Chapter 2 we review some essential concepts about the kinetics of materials during

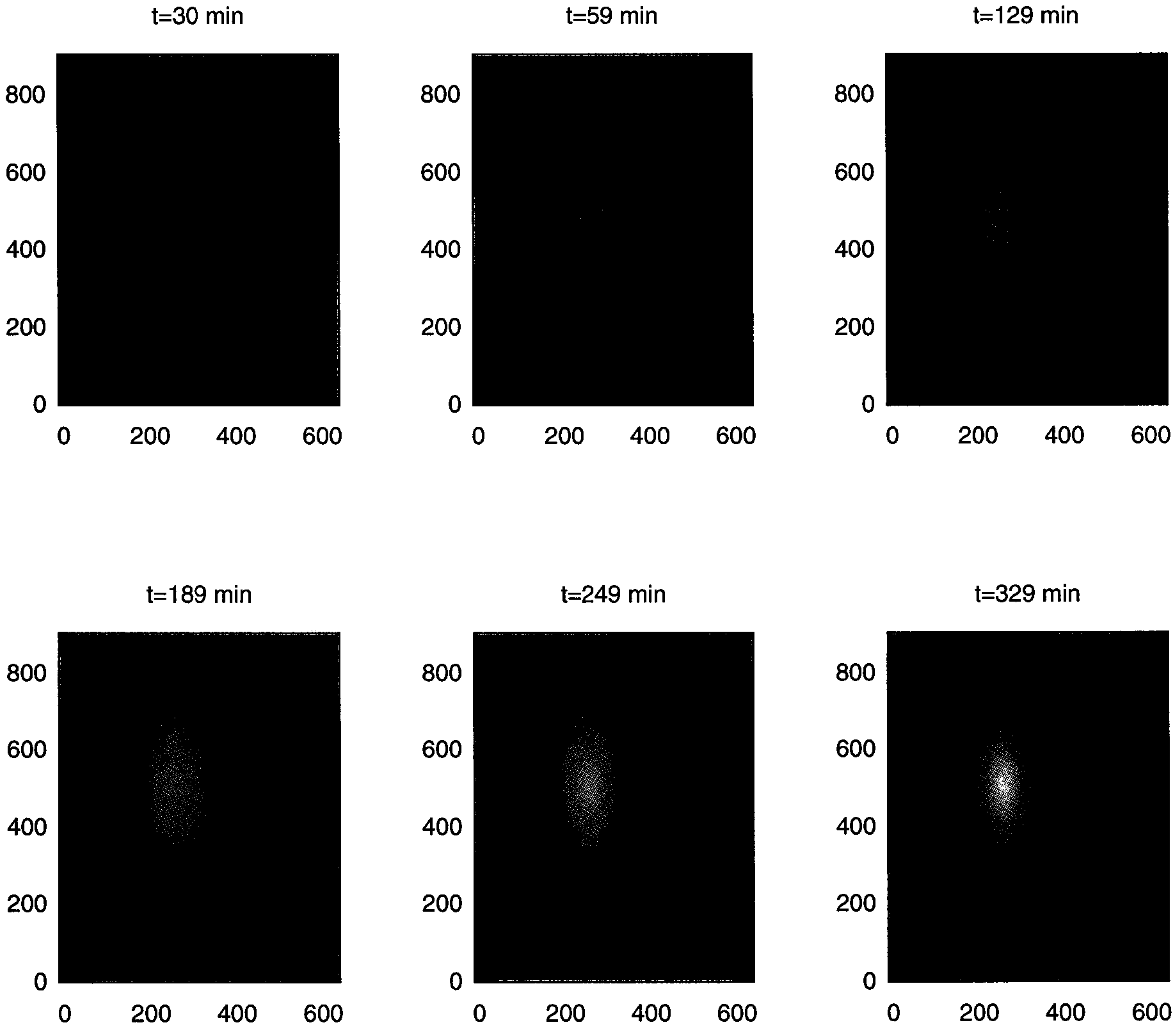

Fig. 1.2 Time evolution of the speckle pattern in a non-equilibrium system. The growth of a Bragg peak associated with an order-disorder phase transition in the binary alloy Cu_3Au is recorded by an area CCD detector (details will follow in Chapter 4

non-equilibrium processes with an emphasis on phase field theories describing the time evolution of systems undergoing first order phase transitions with NCOP. This discussion is followed by some some basic concepts about X-ray diffraction, coherence, coherence of synchrotron radiation and scattering with coherent X-rays. In order to trigger the ordering process a fast and accurate temperature control system is required to perform precise temperature quenches. To achieve this, we designed and implemented a computer-controlled temperature tracking system which combines standard Proportional-Integral-Derivative feedback, thermal modeling (feedforward) and Kalman filtering of the temperature readings. The resulting temperature controller is presented in detail in Chapter 3. This work has been published recently [23].

The main results of this thesis are presented in Chapter 4. The order-disorder phase transition in the binary alloy Cu_3Au has been chosen as a case study for a first order phase transition with NCOP and has been studied by XIFS. The experimental results are in good agreement with theoretical predictions [9]. However, the early-time deviations from the proposed scaling form have been found to last for times much longer than previously thought.

This thesis is concluded in Chapter 5 with an outlook to future work on the order-disorder phase transition in Cu_3Au aimed to provide a better understanding of the early stages of the process. Possible applications of XIFS to other non-equilibrium systems are also being discussed.

Chapter 2

Background

2.1 Introduction to the statistical description of non-equilibrium processes in materials

2.1.1 Non-equilibrium processes in materials

This section reviews some essential aspects of the theoretical description of non-equilibrium processes in materials, with an emphasis on the dynamical properties of a large class of first-order phase transitions. Very good references on this subject are the review article by Gunton et. al. [29] and the textbook on phase transitions by Goldenfeld [25]. The reader can also find a basic introduction to this field in [61].

In a typical situation which will be considered in this discussion and is studied experimentally in this thesis, a system such as a binary alloy or binary fluid is rapidly quenched from a one-phase , thermal-equilibrium state into a new state which is characterized by two coexisting phases.

The phase diagram for such a system is schematically shown in Fig. 2.1 and is usually referred to as the "coexistence curve". In the area above the coexistence curve (solid line), the system is in a thermodynamically stable state. After a temperature quench inside the coexistence curve, the "old" phase becomes a non-equilibrium state. Depending on the exact quench (see for example the quenches labeled (m) and (u) in the figure) this initial state can be either metastable or unstable. From this point, the system gradually evolves towards a new equilibrium state which consists of two coexisting phases, and it does so by the temporal development of spatial fluctuations. To study such a system

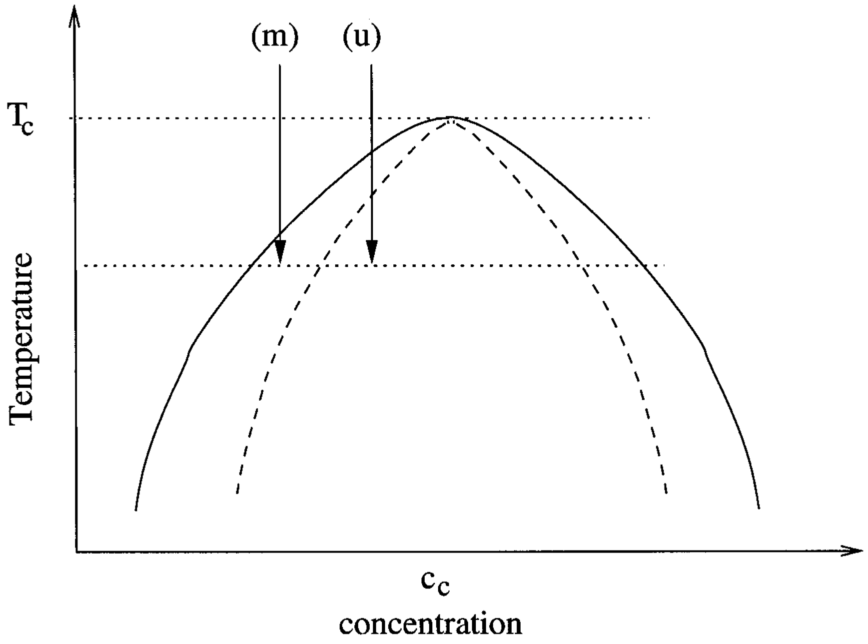

Fig. 2.1 The coexistence curve (solid line) and the spinodal curve (dashed line) for a binary alloy or a binary fluid. A quench (m) into the area between the two lines brings the system to a state where the old phase is metastable. A quench (u) into the area below the spinodal curve brings the system to a state where the old phase is unstable. In both situations, the system evolves towards a new equilibrium state.

means to understand the creation and the time-evolution of the patterns created by the two coexisting phases.

Such a process consists of at least two distinct stages. In the initial phase the system evolves locally towards the new equilibrium state. For example, after a quench inside the metastable region of the phase diagram, a so-called "nucleation and growth" process will cause "droplets" of the new phase to appear and subsequently grow in the matrix formed by the "old", non-equilibrium phase. A quench inside the unstable area of the phase diagram will cause a spontaneous decay to the equilibrium state, also called spinodal decomposition. Once the domains are well-formed, the system keep evolving towards an equilibrium state and "big" domains grow at the expense of smaller domains. This process is driven by the reduction of the surface energy associated with the boundaries between domains in different ground states and is called "coarsening".

Such non-equilibrium processes obviously involve first-order phase transitions since discontinuities in the relative densities of different phases characterize the two-phase equilibrium states.

2.1.2 Langevin description of the kinetics of materials

In order to describe non-equilibrium processes in materials, like the first order phase transitions described above, two "ingredients" are required. One is a way to describe the state of the system at each stage during the process. This is often done in terms of a phase field or order parameter labeled $\psi(\mathbf{r}, t)$, which describes the local order. Depending on the particular system, this can be the local density, concentration, atomic order, magnetization, or many other possibilities. The second "ingredient"needed is an equation of motion for ψ. The time-evolution of the order parameter is driven by the reduction of free energy in the system. The order parameter is also expected to have an average that varies slowly on large length scales but fluctuates on atomic length scales. These fluctuations enable the evolution of the system towards an equilibrium state. An appropriate free energy functional $F\left[\psi(\mathbf{r}, t)\right]$, describes how much these fluctuations "cost" in terms of energy and this determines how large is the "driving force" that tends to reduce the fluctuations and restore the equilibrium values of the order parameter. It is natural thus to expect that such a system is overdamped and to consider a thermodynamic force on a deviation from equilibrium that is proportional to the slope of the free energy cost. This leads to the following Langevin-type of equation that describes the time-evolution of the order parameter ψ:

$$\frac{\partial \psi}{\partial t} = -M\frac{\delta F}{\delta \psi} + \eta(\mathbf{r}, t). \tag{2.1}$$

In this equation, the constant M is the atomic mobility and $\eta(\mathbf{r}, t)$ a noise term, which is assumed to exist only on short length scales. Within the framework of this model, it is natural to consider that the noise term is Gaussian and uncorrelated in space and time with

$$\begin{aligned} &\langle \eta(\mathbf{r}, t)\rangle = 0, \\ &\langle \eta(\mathbf{r}, t)\eta(\mathbf{r}', t')\rangle = 2k_BTM\delta(\mathbf{r}-\mathbf{r}')\delta(t-t'). \end{aligned} \tag{2.2}$$

The second relationship in Eq. 2.2 is also known as the fluctuation-dissipation theorem.

The theoretical model introduced above describes the time evolution of a time-dependent Landau-Ginzburg field theory called model A [1] in the Hohenberg and Halperin classification scheme [31]. This model is used to predict the equilibrium and non-equilibrium properties of a large class of condensed-matter systems, including binary alloys undergoing order-disorder phase transition.

The free-energy functional describing such a process is given by

$$F[\psi] = \int \left(\frac{k\nabla\psi(\mathbf{r}, t)^2}{2} + f(\psi)\right), \tag{2.3}$$

with $f(\psi)$, the potential density, being equal to:

$$f(\psi) = \frac{r\psi^2}{2} + \frac{w\psi^4}{2} \tag{2.4}$$

The potential density $f(\psi)$ changes shape, from a single-well potential for values of $r > 0$ to a double-well potential for values of $r < 0$ (Fig. 2.2)

The equations 2.1 and 2.3 completely define the dynamics of a model A system in which the final state is doubly degenerate. The binary alloy studied in this thesis, Cu_3Au is a system that can be described by such a model when it undergoes an order-disorder phase transition. The only important particular aspect is the fact that the final (ordered) state is not doubly degenerate but four-fold degenerate. However, most of physical aspects of the ordering process are well described by a simple model like the one introduced above. The

---

[1] by replacing M with $-M'\nabla^2$, the model can be used also for conserved order-parameters such composition (model B)

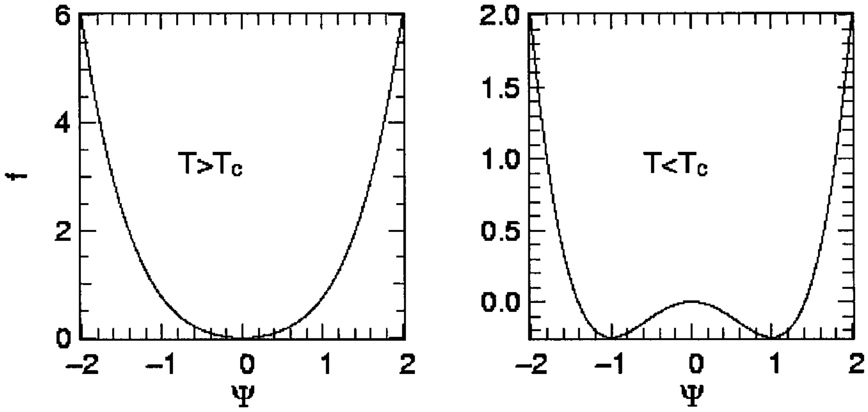

Fig. 2.2 The potential density (Eq. 2.4) before (left panel) and after (right panel) a temperature quench from the disordered state inside the unstable region which is delimited by the spinodal curve (see Fig. 2.1).

order-disorder phase transition and the free energy functional describing the equilibrium and non-equilibrium states will be introduced in Section 4.1.1 of this thesis.

One of the important aspects of the kinetics of a model A process is the time-evolution of the characteristic length in the system (L), which measures the average domain size. Theoretical investigations on such processes [29] predict a scaling law of the form

$$L \sim t^{1/2}. \tag{2.5}$$

This prediction was confirmed by experimental investigations on prototypical systems (see for example [49]).

It is also easy to "guess" the scaling law that describes the time evolution of L by simple dimensional analysis. From the Langevin equation (Eq. 2.1), we can write $[1/t] = [1/L^2]$ and this indicates that a scaling form given by the equation 2.5 must be valid.

The characteristic length L contains all the time-dependence in the system. If scaled by L the system looks invariant in time. This scaling hypothesis describes correctly, at least in the late stages of the processes, many real systems that are described by model A dynamics. Some deviations can however be observed in the early stages of the processes.

In this thesis, XIFS is used to investigate the time-dependent fluctuations around the scaling behavior. The X-ray intensity scattered by the ordered phase is proportional to the

Fourier transform of the order parameter $\psi(\mathbf{r},t)$

$$I(\mathbf{Q},t) = \left[\int d\mathbf{r} e^{i\mathbf{Q}\mathbf{r}}\psi(\mathbf{r},t)\right]^2 = \widehat{\psi}(\mathbf{Q},t)\widehat{\psi}^*(\mathbf{Q},t). \tag{2.6}$$

The ensemble average of $I(\mathbf{Q},t)$ over all the possible micro-configuration in the random disorder is the "average" structure that would be measured by diffraction with incoherent photons,

$$\langle S(\mathbf{Q},t)\rangle \sim \langle I(\mathbf{Q},t)\rangle \tag{2.7}$$

2.2 Introduction to X-ray diffraction

Scattering is one of the most direct ways to probe the structure of condensed matter systems, especially at Ångstrom scale. In order to probe bulk properties of a system, thermal neutrons and photons in the X-ray range are excellent probes because their wavelengths match the interatomic distances. Neutron and X-ray scattering can be seen as complementary techniques in condensed matter physics and each method has specific advantages and disadvantages. The experiments presented in this thesis used only X-ray scattering techniques and, as a consequence, this introduction will concentrate only on X-ray diffraction. Among the main advantages associated with X-ray diffraction, the high brilliance and the high degree of coherence of third generation synchrotron sources play a central role. One of the most quoted disadvantages associated with X-ray scattering are the strong absorption for lower energy photons, the weak scattering from light elements and of course, the radiation-induced damage to samples.

For more than a century, since the discovery of X-rays by Röntgen in 1895, there have been a huge number of publications on the topic. Applications of X-rays span a very large number of fields of science and technology. The short introduction to the elementary theory of X-ray diffraction that will follow in this thesis was inspired mainly by the excellent textbook on condensed matter physics by Chaikin and Lubensky [13], and a more recent, and very nice introduction to modern (synchrotron-based) X-ray diffraction by Als-Nielsen [1]. Other excellent sources on this interesting topic are the classic monograph by Warren [64] and other general books on optics like the text by Born and Wolf [6], which does not deal with X-ray diffraction directly, but is still of major relevance to many of the topics discussed in this thesis, including coherence and coherence-enabled fluctuation spectroscopy. In order to get a full introduction to this very rich field, all these sources should be used instead of, or at least in addition to, this chapter, as it only "scratches the surface".

2.2.1 Elementary X-ray scattering theory

One of the easiest examples of scattering yielding structural information about a scatterer is that of Bragg reflection from a set of equally spaced, partially reflecting planes. In the situation shown in Fig. 2.3, the condition for constructive interference between waves scattered by different planes is given by Bragg's law

$$2dsin\theta = n\lambda, \tag{2.8}$$

where n is an arbitrary integer. The basic physical idea behind Bragg's law, which remains true for any scattering experiment is that a wave scattered at an angle of 2θ reflects an inhomogeneity in the system with periodicity $\frac{\lambda}{2sin\theta}$.

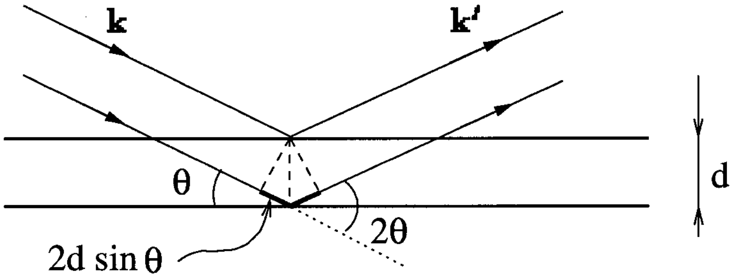

Fig. 2.3 Scattering from parallel planes illustrates the basic ideas behind Bragg's law. The incident wave vector is **k** ($\mathbf{k} = \frac{2\pi}{\lambda}$) and the reflected wave vector is $\mathbf{k}'$. If the distance between planes is d, the path difference between waves reflected by successive planes is $2dsin\theta$, where θ is the angle between the incident wave and the scattering planes. (Note that 2θ is the angle between incident and scattered waves.)

In a slightly more advanced approach, the scattering of the incident wave **k** into $\mathbf{k}'$ is described in terms of a quantum mechanical transition rate of the X-ray photons from an initial state $|\mathbf{k}\rangle$ into a final state $|\mathbf{k}'\rangle$, with respective linear momenta $\hbar\mathbf{k}$ and $\hbar\mathbf{k}'$. If the particles are scattered by a weak potential $U(\mathbf{r})$, which is weak enough to be able to neglect multiple scattering, than the transition rate is given by the Fermi golden rule,

$$W_{\mathbf{k}\to\mathbf{k}'} = \frac{2\pi}{\hbar}\left|M_{\mathbf{k},\mathbf{k}'}\right|^2 = \frac{2\pi}{\hbar}\langle\mathbf{k}|U|\mathbf{k}'\rangle^2 = \frac{2\pi}{\hbar}\left[\int d^d r e^{-i\mathbf{k}\mathbf{r}}U(\mathbf{r})e^{i\mathbf{k}'\mathbf{r}}\right]^2. \tag{2.9}$$

Here d is the dimensionality of the space. (Most commonly, d=2 or 3.) If Φ is the incident flux of photons $[s^{-1}cm^{-2}]$, the following cross sections can be defined for the scatterer:

i) Partial, differential cross-section,

$$\frac{d^2\sigma}{d\Omega dE} = \frac{N}{\Phi d\Omega dE}, \tag{2.10}$$

with N being the number of scattered particles in a solid angle $d\Omega$ and with energies between E and $E + dE$.

ii) Differential cross-section,

$$\frac{d\sigma}{d\Omega} = \frac{N}{\Phi d\Omega} = \int_0^\infty \frac{d^2\sigma}{d\Omega dE}dE, \tag{2.11}$$

with N being the total number of scattered particles in a solid angle $d\Omega$.

iii) And finally, the cross-section,

$$\sigma = \frac{N}{\Phi} = \int_0^\infty dE \int d\Omega \frac{d^2\sigma}{d\Omega dE}, \tag{2.12}$$

with N being the total number of scattered particles, in any direction and with any energy.

The quantity obtained in a typical X-ray diffraction experiment is the differential cross-section (Eq. 2.11. The dispersion relationship for photons is

$$\epsilon = \hbar\omega = \hbar ck = \frac{hc}{\lambda}. \tag{2.13}$$

A wavelength of 1.6Å corresponds to an energy of $\epsilon \simeq 7.66$keV. Probing the structure of condensed matter at atomic length scales requires thus, energies of $10^3 - 10^5$ eV. Since the energies of typical excitations in condensed matter systems are of the order of a fraction of an eV and such small energy shifts are difficult to measure, most X-ray detectors detect all the photons scattered in a given direction regardless of their (small) energy change. This property makes X-rays very well suited tools to measure static structural properties.

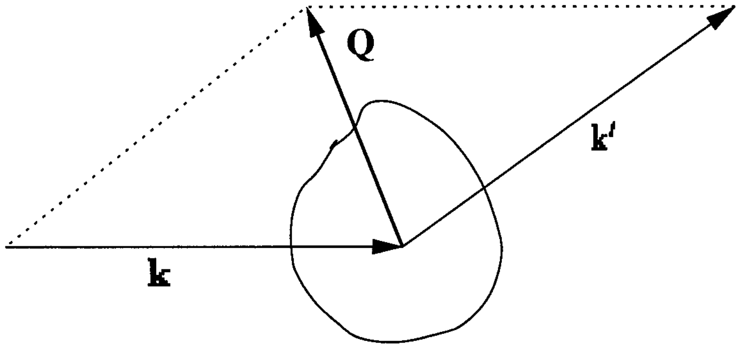

Fig. 2.4 Typical scattering geometry. The incident wave **k** scatters into **k'**. The transfered wavevector is **Q=k'-k**

For a typical X-ray scattering experiment like the one schematically shown in Fig. 2.4, the differential cross-section (Eq. 2.11) measured by a detector is given by Fermi's golden rule (Eq. 2.9). Thus,

$$\frac{d\sigma}{d\Omega} = \frac{2\pi}{\hbar} \left| M_{\mathbf{k},\mathbf{k}'} \right|^2 . \tag{2.14}$$

In complex systems, the scattering potential is a sum of contributions from individual particles

$$U(\mathbf{r}) = \sum_{\alpha} U_\alpha(\mathbf{r} - \mathbf{r}_\alpha) \tag{2.15}$$

By bringing this form into the matrix element in the Eq. 2.9 [13], the scattering from a set of identical individual scatterers located at fixed positions r_α can be separated into a contribution from only one scatterer $|U_\alpha((\mathbf{Q})|^2$, called the form factor, and a sum which depends only on the positions r_α and not on the nature of interaction between the system and the scattering probe, called the structure factor. The differential cross section from such a system is,

$$\left(\frac{d\sigma}{d\Omega}\right) \sim |U_\alpha((\mathbf{Q})|^2 S(\mathbf{Q}), \tag{2.16}$$

with the structure factor defined by

$$S(\mathbf{Q}) = N^{-1}\langle\sum_{\alpha,\alpha'} e^{i\mathbf{Q}(\mathbf{r}_\alpha - \mathbf{r}_{\alpha'})}\rangle \tag{2.17}$$

The structure factor contains information about the average relative position of scatterers (atoms). It can be shown [13, 1] that it is in fact a Fourier transform of the density-density correlation function. For the same collection of particles located at a set of positions $\mathbf{r}_\alpha$ that we considered above, the density "operator" $\rho(\mathbf{r})$ can be defined as a function of the dynamical variables $\mathbf{r}_\alpha$,

$$\rho(\mathbf{r}) = \sum_\alpha \delta(\mathbf{r} - \mathbf{r}_\alpha). \tag{2.18}$$

Correlation functions of the density operator are ensemble averages of products of the density operator at different point in space. If the densities at the two points are uncorrelated the average is expected to be zero. A non-zero correlation indicates the existence of some form of ordering. With a two-point density-density correlation function defined by

$$C_\rho(\mathbf{r}_1, \mathbf{r}_2) = \langle\rho(\mathbf{r}_1)\rho(\mathbf{r}_2)\rangle = \langle\sum_{\alpha,\beta} \delta(\mathbf{r}_1 - \mathbf{r}_\alpha)\delta(\mathbf{r}_2 - \mathbf{r}_\beta)\rangle, \tag{2.19}$$

the structure factor defined by Eq. 2.17 is proportional to the Fourier transform of this correlation function:

$$S(\mathbf{Q}) = \int C_\rho(\mathbf{r}_1, \mathbf{r}_2) e^{-i\mathbf{Q}(\mathbf{r}_1 - \mathbf{r}_2)}. \tag{2.20}$$

We can conclude from here that *scattering is a direct measurement of density-density correlation functions.* From this point of view there is an intimate connection between equilibrium and non-equilibrium statistical mechanics, which allows the calculation of such correlation functions and scattering techniques such as X-ray diffraction which allow their direct measurement.

2.2.2 Scattering from crystalline solids

A crystal is characterized by the periodicity of its structure and may be constructed by placing a basic structural unit known as the basis at the lattice points specified by a set of vectors R_n with

$$\mathbf{R}_{n_1,n_2,n_3} = n_1\mathbf{a}_1 + n_2\mathbf{a}_2 + n_3\mathbf{a}_3. \tag{2.21}$$

The fixed vectors $\mathbf{a}_1, \mathbf{a}_2, \mathbf{a}_3$ are called the lattice vectors and they define the unit cell. All the general concepts about X-ray scattering introduced above apply to the scattering of X-ray photons from crystalline solids. The "special" feature associated with crystals is that the structure factor (Eq. 2.17) can be either very large, if the periodicity of the lattice "matches" with the scattering wavevector, or very small otherwise. This leads to the apparition of Bragg peaks in the diffraction patterns from crystals.

The wavevectors at which one can observe the Bragg reflections can be defined in terms reciprocal lattice vectors. The reciprocal lattice corresponding to the lattice defined by the vectors $\mathbf{a}_1, \mathbf{a}_2, \mathbf{a}_3$ is defined by a set of reciprocal vectors, $\mathbf{a^*}_1, \mathbf{a^*}_2, \mathbf{a^*}_3$ given by

$$\mathbf{a}_\alpha \dot{\mathbf{a}}^*{}_\beta = 2\pi\delta_{\alpha,\beta}. \tag{2.22}$$

It is demonstrated in almost any textbook on solid state physics (see for example [3, 35]) that the conditions above are equivalent with the reciprocal vectors being defined by

$$\mathbf{a}_1^* = 2\pi\frac{\mathbf{a}_2\times\mathbf{a}_3}{\mathbf{a}_1\cdot(\mathbf{a}_2\times\mathbf{a}_3)};\quad \mathbf{a}_2^* = 2\pi\frac{\mathbf{a}_3\times\mathbf{a}_1}{\mathbf{a}_1\cdot(\mathbf{a}_2\times\mathbf{a}_3)};\quad \mathbf{a}_3^* = 2\pi\frac{\mathbf{a}_1\times\mathbf{a}_2}{\mathbf{a}_1\cdot(\mathbf{a}_2\times\mathbf{a}_3)}\ . \tag{2.23}$$

This leads to a variation of Bragg's law, known as the Laue condition, which states that the Bragg reflections can be found at those locations for which the scattering vector $\mathbf{Q} = \mathbf{k}' - \mathbf{k}$ is equal to a reciprocal vector $\mathbf{G} = n_1\mathbf{a^*}_1 + n_2\mathbf{a^*}_2 + n_3\mathbf{a^*}_3$. The distinct peak in the diffraction pattern is labeled with the three indices n_i ($[n_1n_2n_3]$).

2.3 Synchrotron sources and X-ray coherent beams

The third-generation synchrotron sources available today generate extremely bright beams of radiation over the entire X-ray spectrum, and with properties such as coherence, polarization, energy resolution, that can be tailored to meet many experimental requirements. These improvements have enabled many new types of experiments and applications and they have a growing impact on many areas of science and technology [1, 21]. Recent progress in the X-ray detector technology have also had an invaluable impact in X-ray science. Charge-coupled device (CCD)-based area detectors have improved the quality and the speed of X-ray data acquisition [28, 39] for many scattering and imaging applications.

One of the very important possibilities opened by the modern synchrotron radiation sources is that of using coherent X-rays in scattering and imaging experiments [60, 46, 37].

Synchrotron X-ray beams posses a high degree of coherence [15] which can be exploited in X-ray experiments. Formally, a source is called coherent, or partially coherent if there is a non-zero correlation between the electric fields at two different locations and two different times, which is measured by a so-called mutual coherence function

$$\Gamma(\mathbf{r}_1, \mathbf{r}_2, t_1, t_2) = \langle E(\mathbf{r}_1, t_1) E^*(\mathbf{r}_2, t_2) \rangle \tag{2.24}$$

It can be demonstrated [61, 26] that the degree of spatial coherence is related to the intensity distribution of the source by a Fourier transformation (van Cittert-Zernike theorem).

In practice, the coherence of synchrotron radiation beams is usually defined in terms of the longitudinal and the transverse coherence lengths. The longitudinal coherence measures the property of the wave to produce an interference pattern with a time-delayed copy of itself in the same way that two copies of the same beam produce interference patterns in a Michelson interferometer after having traveled different optical paths. Similarly, the transverse coherence of a beam measures the ability of the wave to produce interference fringes in a Young double slit experiment. If the two slits are separated by more than a few transverse coherence lengths, no fringes will be seen in the screen.

The longitudinal coherence length [6] is determined by the relative bandwidth of the source

$$l_{\|} = \frac{\lambda^2}{2\delta\lambda}. \tag{2.25}$$

In words, the coherence of the wave is lost if the wavelength spread $\delta\lambda$ can create phase differences larger than π (λ /2).

The transverse coherence length is determined by size of the source d and the distance from the source to the observation point R

$$l_{\perp} = \frac{\lambda R}{2d}. \tag{2.26}$$

The transverse and longitudinal coherence lengths define a so-called coherence volume. When the illuminated sample volume is smaller than the coherence volume, the individuality of the exact arrangement of random fluctuations superposed on the slow-varying average structure shows up as a speckle pattern in the scattering intensity. The size of the individual speckles is given by the diffraction-limited resolution obtained from the illuminated area. If D is the size of the coherent beam (usually delimited by a set of slits or by pinholes) and L is the sample-detector distance, the speckle size can be estimated by

$$s \sim \frac{1.22\lambda L}{D}. \tag{2.27}$$

The effects of the partial coherence on the scattering of X-rays by matter have been studied in detail in review articles by Pusey [53] and by Sinha et. al. [58].

Here we will describe only the coherent X-ray scattering from a non-equilibrium system such a material undergoing an order-disorder phase transition. If $\psi(\mathbf{r}, t)$ is the order-parameter and $\widehat{\psi}(\mathbf{q}, t)$ is its Fourier transform, the scattered intensity from the ordered phase is:

$$I(\mathbf{q}, t) = \langle \widehat{\psi}(\mathbf{q}, t)\widehat{\psi}(\mathbf{q}, t\rangle. \tag{2.28}$$

The intensity covariance can be related to the order-parameter correlation function:

$$\langle I(\mathbf{q}, t_1)I(\mathbf{q}, t_2)\rangle = \langle \widehat{\psi}(\mathbf{q}, t_1)\widehat{\psi}^*(\mathbf{q}, t_1)\widehat{\psi}(\mathbf{q}, t_2)\widehat{\psi}^*(\mathbf{q}, t_2)\rangle, \tag{2.29}$$

$$\begin{aligned} &\langle I(\mathbf{q}, t_1)I(\mathbf{q}, t_2)\rangle = \\ &\quad \langle \widehat{\psi}(\mathbf{q}, t_1)\widehat{\psi}^*(\mathbf{q}, t_1)\rangle\langle \widehat{\psi}(\mathbf{q}, t_2)\widehat{\psi}^*(\mathbf{q}, t_2\rangle + \\ &\quad \langle \widehat{\psi}(\mathbf{q}, t_1)\widehat{\psi}^*(\mathbf{q}, t_2)\rangle\langle \widehat{\psi}^*(\mathbf{q}, t_1)\widehat{\psi}(\mathbf{q}, t_2)\rangle + \\ &\quad \langle \widehat{\psi}(\mathbf{q}, t_1)\widehat{\psi}(\mathbf{q}, t_2)\rangle\langle \widehat{\psi}^*(\mathbf{q}, t_1)\widehat{\psi}^*(\mathbf{q}, t_2)\rangle. \end{aligned} \tag{2.30}$$

With the two-time structure factor corresponding to the two-point two-time order-parameter correlation function defined as,

$$S(\mathbf{q}, t_1, t_2) = \langle \hat{\psi}(\mathbf{q}, t_1)\hat{\psi}^*(\mathbf{q}, t_2)\rangle, \tag{2.31}$$

the intensity covariance becomes

$$C(\mathbf{q}, t_1, t_2) = \langle I(\mathbf{q}, t_1)I(\mathbf{q}, t_2)\rangle = (1 + \delta_{\mathbf{q},0})\, S\,(\mathbf{q}, t_1, t_2) + S(\mathbf{q}, t_1)S(\mathbf{q}, t_2). \tag{2.32}$$

For $\mathbf{q} \neq 0$, the speckle intensity covariance becomes simply equal to the square of the two-time structure factor of the system:

$$C\,(\mathbf{q}, t_1, t_2) = S^2\,(\mathbf{q}, t_1, t_2) \tag{2.33}$$

2.4 Applications of coherent X-ray diffraction

There are two main applications for coherent X-rays. One is the ability to use phase information in order to perform real-space imaging in phase contrast. Mathematically, it is known that using coherent X-rays allows one to invert the (speckled) diffraction pattern. Such an operation requires knowledge about both the amplitude and phase of the scattered radiation. Unfortunately the phase information is lost in a diffraction experiment (this is usually referred to as the "phase-problem") and doing such an inversion becomes a very complicated problem. Recently, Miao et. al. [46, 47] and Robinson et. al. [55] have demonstrated that so-called phase retrieval algorithms based on an oversampling method can be applied to obtain real space images of small, non-crystalline objects.

The main focus of the present research is another class of coherence-enabled applications, and that is the study of dynamics of fluctuations by using intensity fluctuations spectroscopy. As it was pointed out in the introduction, this technique has emerged with the observation of static speckles in the scattering patterns from systems containing some random disorder [60, 12]. Further studies have proven that it is possible to measure the dynamics of fluctuations in a large class of systems by measuring fluctuations in the speckle pattern. The X-ray Intensity Fluctuation Spectroscopy (XIFS) technique has been applied to study dynamical properties in a very large class of equilibrium systems. Brauer et. al. have studied critical dynamics in metallic alloys near second order phase transitions (Fe_3Al) [7]. Other systems and processes studied by XIFS in the last decade have included the Brownian motion of gold colloids in glycerol [16], fractal aggregates composed of gold particles [63], diffusion of polymer micelles [48], suspensions of latex spheres [41], surface dynamics of polymer films [34], concentration fluctuations in binary hexane-nitrobenzene mixtures [19] and grazing incidence studies of liquid surfaces [43, 42, 57].

Extending the XIFS technique to non-equilibrium systems is under way and in the present thesis we report the first measurements of two-time correlations during first order phase transitions with non-conserved order parameter in non-equilibrium systems. Previous XIFS studies in non-equilibrium systems have measured the dynamics of fluctuations in conserved systems such as phase separation in AlLi alloys [38] and sodium-borosilicate glasses [44].

Chapter 3

KPPID Temperature Control

3.1 Introduction

With third generation synchrotron X-ray sources, it is possible to acquire detailed structural information about the system under study in times that are orders of magnitude faster than was possible a few years ago. These advances have generated many new challenges for changing and controlling the state of the system on very short time scales, in an uniform and precise manner.

For our particular X-ray experiments on non-equilibrium processes in metallic alloys, we need to accurately change the sample temperature by hundreds of degrees in times that are orders of magnitude shorter than the thermal response time constants, but also, to keep the temperature stable and constant for times which are many orders of magnitude longer.

Some examples of X-ray studies of non-equilibrium processes which push the limits of available temperature control technology are shown in Fig. 3.1. The amorphous NiZr sample (metallic glass) undergoes a crystallization process if the sample temperature is raised by a couple of hundred degrees Celsius. The time-resolved X-ray scattering patterns and the temperature step are shown in panels (a) and (b).

The order-disorder transition in Cu_3Au is a classic [64] example of a first-order phase transition. If the temperature drops from a value above the critical temperature ($T_c \simeq 380°C$) to a value just below it (Fig. 3.1 (c)), the sample undergoes an ordering process which can be monitored by recording the growth of one of the superlattice X-ray Bragg peaks (panel (d))

Both studies require similar temperature tracking capabilities. The sample tempera-

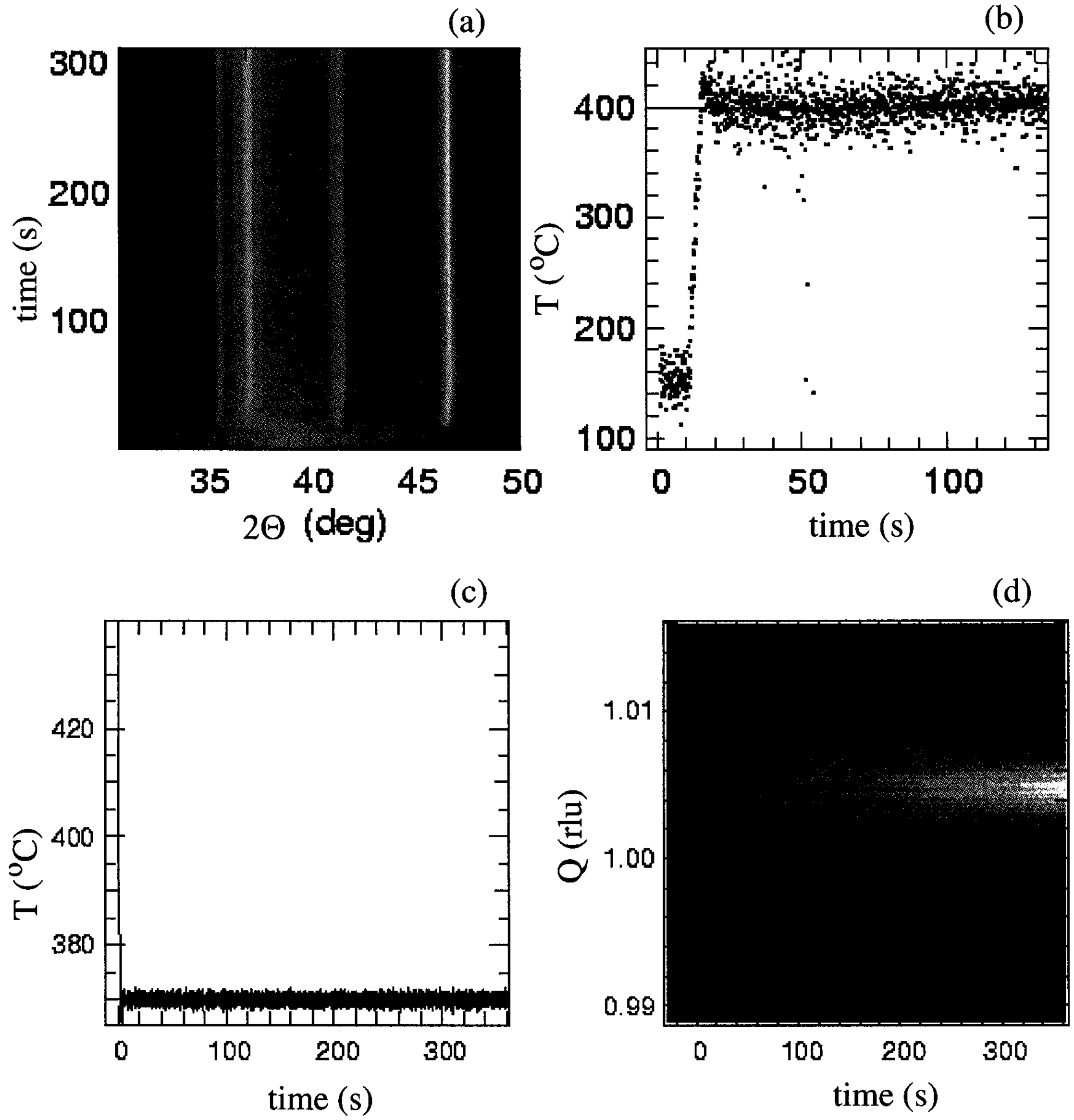

Fig. 3.1 X-ray studies of non-equilibrium processes in material science require a fast and accurate temperature control. A NiZr metallic glass undergoes a fast crystallization process (a) following a sudden increase in the sample temperature (b). Growth of the [100] superlattice Bragg peak in a Cu_3Au alloy (d) after a temperature quench through the order-disorder phase transition (c).

ture has to undergo an initial fast process followed by a very long, stable run at constant temperature. Also, the final state has to be reached without any significant temperature oscillations (over/under shooting). This requirement is critical in the study of phase transitions where small temperature variations can completely change the kinetics of the process.

One of the most common practical ways to regulate the temperature in a system is by controlling the amount of power supplied to a heating element. It is useful at this point to introduce the block diagram of a simple, generic, temperature controller (Fig. 3.2). Such representations will be particularly useful later, to describe more complicated systems.

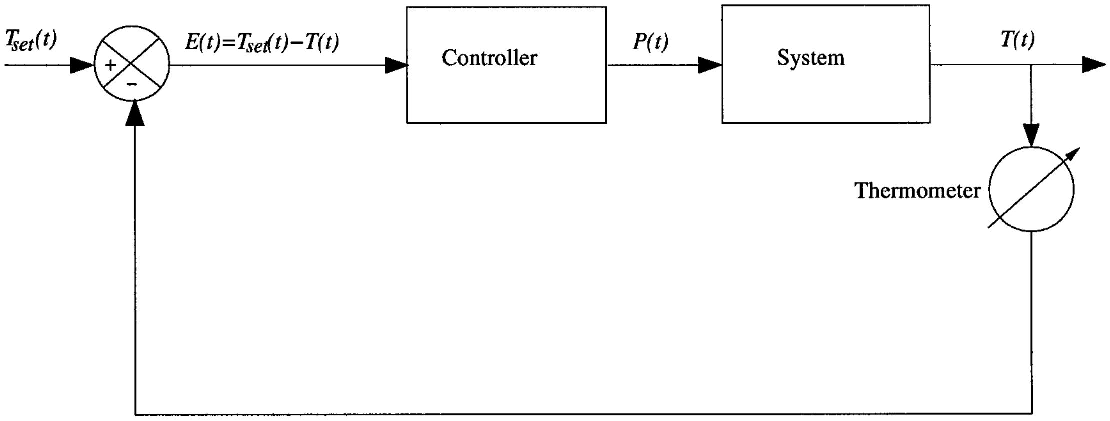

Fig. 3.2 Block diagram of a generic temperature controller. The sample temperature at time t, $T(t)$ is regulated by modulating the amount of heating power, $P(t)$, supplied to a heating element included in the experimental system.

The central element of any temperature controller (and any controller in general) is the control algorithm that determines the amount of heating power that has to be delivered to the heating element as a function of the target temperature T_{set} and the actual, measured, temperature T. One of the most common control algorithm is the Proportional-Integral-Derivative (PID) controller which will be presented in Section 3.2.1.

This is the general architecture of most continuous (analog) temperature controllers. However, for many important practical reasons, including flexibility and the possibility of using the controller for different experimental stages, a programmable, computer based temperature controller is usually advantageous. It is important though, to understand some differences associated with digital control. From a practical point of view an input/output system that interfaces the computer with the physical system is required. Such an interface allows the temperature to be read from the control program, which in return sets the appropriate amount of heating power. The most important difference, however, comes with the fact that data input (A/D conversion) and output (D/A conversion) occurs at some discrete times: $t_1, t_2, ..., t_k, ...$. Also, it is important to realize that in a digital system, the power output at step "k" (which means the power output between time t_k and t_{k+1}) will influence the temperature recorded at step "$k+1$". The general structure of a digital temperature controller is presented in Fig. 3.3.

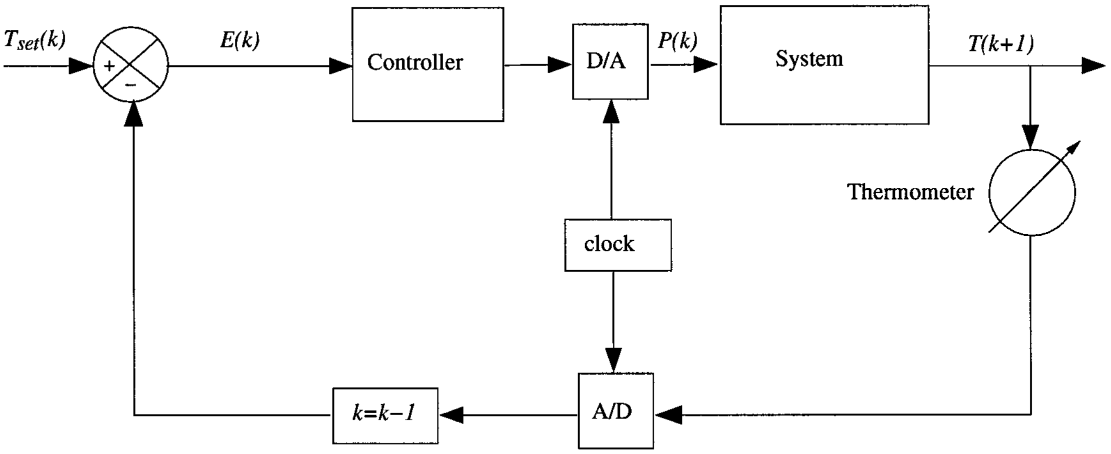

Fig. 3.3 Block diagram of a digital temperature controller.

With this "mini-introduction" to control engineering and in particular to temperature control, one can formulate the requirements for a temperature controller to be used for the study of various non-equilibrium processes in materials:

Design a computer-controlled (digital) temperature tracking system which allows fast and accurate temperature-changing processes as well as very long and stable runs at constant temperature.

The PID controller is a real "workhorse" for many practical applications and the temperature controller described in this chapter is not an exception and is based on the PID feedback algorithm. However, as it will be clearly seen in the following sections, a "standard" PID controller doesn't meet all the requirements stated above. Consequently, the PID feedback loop was combined with thermal modeling and finite difference thermal calculations of the temperature distribution in the system (Feedforward) in order to compensate for some of the problems associated with simple PID control, and Kalman filtering in order to reduce the effect of the noise on the the temperature readings. The resulted Kalman-Predictive-Proportional-Integral-Derivative (KPPID) algorithm allows faster response times while avoiding any significant temperature over/under shooting and has all the benefits associated with PID control when one needs to keep a constant temperature for very long experimental runs.

3.2 Techniques

The main techniques used in the design of the KPPID temperature controller are presented in this chapter. The PID feedback algorithm is described in the following section. Thermal modeling and finite difference calculations of the temperature distribution in a system, as well as the calculation of an "optimal" power profile that leads to the desired evolution of the sample temperature, which is the feedforward technique used in the KPPID system, will follow in Section 3.2.2. Finally, the dynamic Kalman filtering technique, used to reduce the effects of the noise on the temperature readings will conclude this chapter.

3.2.1 PID control

One of the most common algorithms in control engineering is the Proportional-Integral-Derivative (PID) controller [20]. Its functioning principle is simple and robust. In order to minimize the error function, $e(t)$, which is the difference between the target temperature and the measured temperature, the heating power $P(t)$ is set by a feedback algorithm, by the formula

$$P(t) = K_p \left(e(t) + \frac{1}{T_i} \int_0^t e(t)dt + T_d \frac{de(t)}{dt} \right). \tag{3.1}$$

The PID controller thus consists of three components, each with its own distinctive function to fulfill certain control objectives. The coefficient K_p is the gain of the feedback circuit, T_i the integral time constant, and T_d the derivative time constant. Together, they control and determine the response of the system. The proportional term (K_p) is the main term which determines the response time, but without an integral correction, it would produce a steady state error. The integral term eliminates the steady-state error but makes the transient response worse. The derivative term improves the transient response by reducing the over/under shooting and reducing the response time. However, the derivative term has to be reduced or canceled in systems with appreciable noise on the temperature readings.

In Fig. 3.4 we show the block diagram of a PID controller. The error signal ($e(t)$) is the input of the PID controller, which computes the integral and the derivative of this signal and outputs the level of heating power ($P(t)$) to be sent to the system or "plant", how it is called in the control engineering literature. The power level and possibly other parameters denoted in the diagram by $x_1, x_2, ...$ will determine the output of the system, which is the sample temperature $T(t)$.

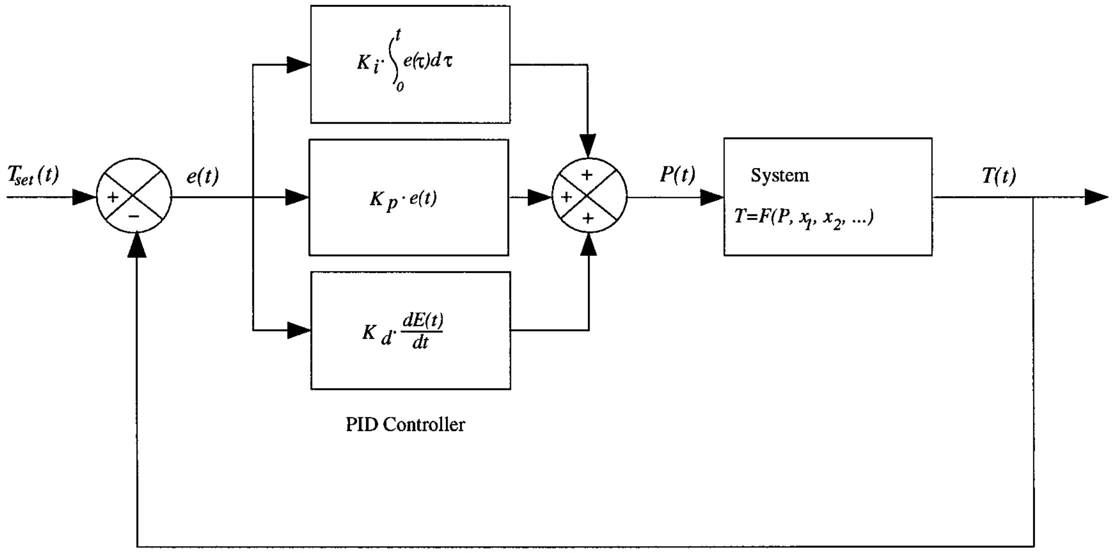

Fig. 3.4 Block diagram of a PID controller.

The PID controller works extremely well if one needs to keep a constant temperature or if one needs to track a slow-varying temperature profile. However, it is well known that when dealing with more complex temperature profiles, conventional PID control can be limited. For example, as shown in Fig. 3.5 the response of a PID controller to a sudden change in the set temperature (step function) will either undergo a few oscillations before reaching the desired steady state or will slowly drift towards the final temperature if the gain is reduced in order to avoid over/under shooting. The PID algorithm is also less effective in dealing with systems with time lags because the apparent lack of response to a change in power will be attributed to insufficient adjustment of the controlling power.

Tuning a PID controller is a whole "art" in control engineering. Finding the right combination of parameters (K_p, T_i and T_d) for a certain control objective is far from being

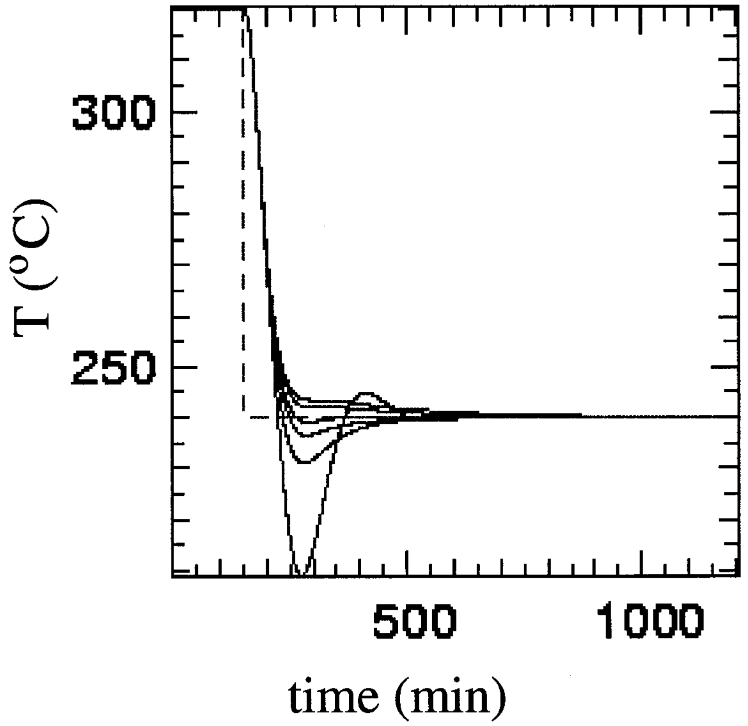

Fig. 3.5 PID response functions to a sudden drop in the set temperature.

a trivial issue and at least at some level, all the "fine-tuning" methods have some empirical, semi-empirical or trial and error based components. One of the most quoted methods for tuning a PID controller is the Ziegler-Nichols (ZN) method. The basic idea behind a ZN tuning method is simple in essence. Assuming a first order (linear) system, the equation describing the time evolution of the output function, $T(t)$ in the feedback system is similar to the equation of motion of a damped harmonic oscillator. An optimal tuning would correspond to a critical damping of the oscillations. In control engineering language this can be also viewed as a matching between the poles of the "transfer functions" for the PID feedback algorithm and the system, but in order to introduce this notion rigorously, we would have to talk about the frequency domain characterization of a system, poles, relationship between frequency domain and time domain, and this is beyond the purpose of this chapter.

Based on the ideas mentioned above, a "tuning recipe" can be described in terms of the open loop response of the plant, which is the response to an excitation of the input quantity (heating power) without any feedback system. The time evolution of the sample temperature $T(t)$ caused by a step-like heating power profile - $P(t)$ is schematically shown in Fig. 3.6. The response to a step in the heating power of ΔP can be described in terms of a few parameters: a lag time (L), a time constant (T) and a process response (ΔT). The significance of each of these parameters can be easily understood from Fig. 3.6.

With these open-loop parameters, two other parameters, a gain $G = \frac{\Delta T}{\Delta P}$ and $K = \frac{T}{GL}$, can be defined. The optimal parameters for a PID and a PI (derivative gain set to zero) feedback circuit are than given by the following formulas:

$$\begin{array}{rr} K_p = 0.9 \cdot K;\ T_i = 3.3 \cdot L & (PI) \\ K_p = 1.2 \cdot K;\ T_i = 2 \cdot L;\ T_d = 0.5 \cdot L & (PID) \end{array} . \tag{3.2}$$

In all the experimental runs involving standard PID control described in this thesis, the temperature controller was tuned using the Ziegler-Nichols method followed by some empirical, trial and error based, "fine tuning". However, as it was emphasized before, even with very careful tuning, the PID algorithm has its own limits and this can cause significant perturbations in many experiments involving non-trivial temperatures profiles.

In order to overcome some of the deficiencies of a standard PID controller, the KPPID algorithm combines PID feedback with a priori calculation of an "optimal" power profile (feedforward). The feedforward technique used is described in the next section of this

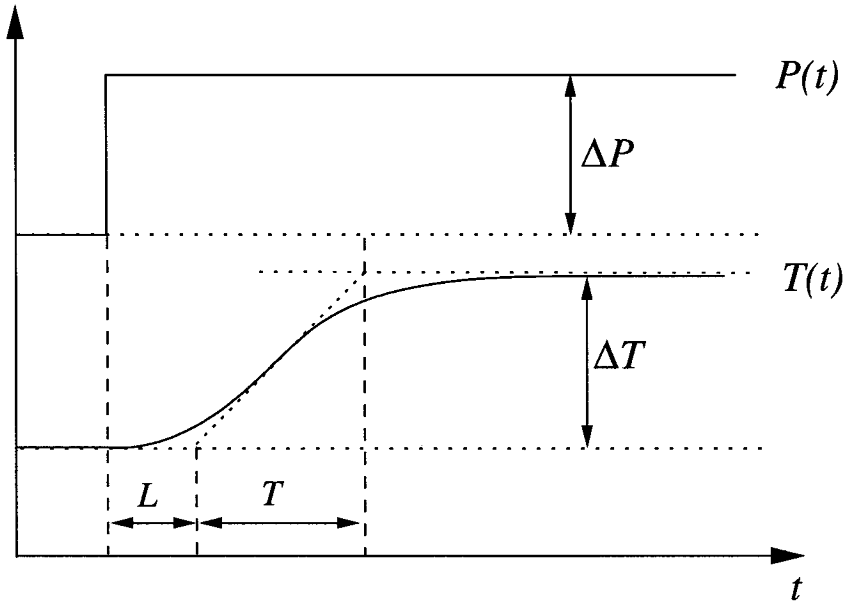

Fig. 3.6 Open-loop response of the system for the Ziegler-Nichols tuning of the PID feedback loop.

chapter.

Another practical aspect that can limit the performance of a temperature controller is temperature measurement. In many experiments the use of a temperature probe with a high intrinsic noise, such as a optical pyrometer, is required by the nature of the system under study. With a noisy temperature reading, any feedback system tends to oscillate between the maximum and minimum heating power when the control gain is high enough to ensure a reasonably fast response time. In order to reduce the effects of the noise on the temperature measurements a Kalman filtering technique is used to obtain a more accurate estimate for the sample temperature. Details about temperature measurement and the Kalman filter follow in Section 3.2.3.

3.2.2 Thermal calculations. Feedforward

The basic idea behind the feedforward technique employed by the KPPID algorithm is that, given a model for the sample furnace, an optimal power profile, which is the power profile that leads to the desired time evolution of the sample temperature, can be calculated. In practice, this is, of course, true only to a certain level of accuracy. Any model of the thermal system provides only an approximation for the response of the real system. Fluctuations in the ambient conditions are also a common source of fluctuations of the sample temperature. In addition, finding the power profile which leads to a given temperature profile is an "inverse problem" which requires approximate numerical methods for all thermal models, except the simplest linear systems. For these reasons, the feedforward calculations have to be combined with a feedback circuit. By doing this, the control system can correct "on the fly" for errors in the feedforward calculations. A very important benefit of this method, is that corrections made by the feedback system are small if the feedforward calculations are adequate and this will minimize many of the above mentioned problems associated with PID feedback. These deficiencies are generally associated with the times when the feedback algorithm attempts to cancel large differences between the set values and the measured values.

The key element to the feedforward thermal calculations is, of course, a good thermal model. At the same time, in order to be able to find the temperature distribution in real time while the experiment is running, the model should also be simple enough to be solved by the controller. This leads to the need to compromise between accuracy and speed.

The thermal configuration of a system, which is the temperature distribution as a function of position and time, $T(\mathbf{r}, t)$, is determined by solving the heat equation [4],

$$\nabla^2 T - \frac{1}{\alpha}\frac{\partial T}{\partial t} = -\frac{p}{k}, \tag{3.3}$$

with appropriate boundary conditions. The parameters involved depend on the particular materials, with $\alpha = k/\rho c$ the thermal diffusivity, k the thermal conductivity, c the heat capacity, ρ the density and p, the power flowing into a unit volume by means other than thermal conduction.

The correct meaning of the heat equation (Eq. 3.3) can be understood more easily if one considers the integral form of the heat equation. Given a domain D delimited by the closed surface Σ (Fig. 3.7), the power balance between the power density generated within the volume p, the flux of power "lost" via thermal conduction $k\nabla T$ and the power density required to change the temperature of the material $\rho c\frac{dT}{dt}$, can be written as

$$\frac{d}{dt}\int_D \rho c T dv = \int_D p dv + \oint_\Sigma k\nabla T d\mathbf{s}. \tag{3.4}$$

The Eq. 3.4 is also known as the Stefan equation [24]. With this, one of the most important

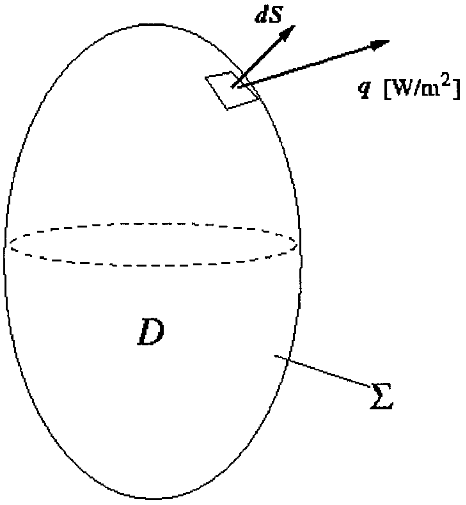

Fig. 3.7 The balance between the power generated within a volume D, the power "lost" via thermal conduction through the surface Σ bounding the volume and the power required to change the temperature within the domain D is expressed by the Stefan equation (Eq. 3.4).

mechanisms for heat exchange, namely, heat conduction, has been implicitly introduced. However, there are many other mechanisms through which different systems, or different parts of the same system, can exchange thermal energy. Some of the most common ones are heat convection, thermal contacts between different objects and radiation. These mechanisms and the equations describing each are summarized in Table 3.1. Generally, they are used to write the correct boundary conditions for a given thermal problem.

The experiments presented in this thesis have used two different X-ray ovens. The first one, referred to hereafter as the "hotplate oven" (see Fig. 3.8) is a rather slow furnace, which provides good temperature stability and holds relatively big samples (penny-sized). The essential element of the furnace is a pyrollitic-Boron-Nitride coated pyrollitic graphite heater [1] mounted on a water-cooled Cu heat sink. In order to increase the temperature stability and the maximum temperature for a given heating power, a layer of mica can be inserted between the heater and the Cu post. This arrangement gives sufficient cooling power to quench the sample at a rate of about 1°C/s. The sample-holder, heater and cooling post are mounted in a vacuum chamber. The temperature probe is a thermocouple fixed on the surface of the sample. The "hotplate oven" is described in more detail in [18].

The second X-ray oven ("ribbon-oven" in Fig. 3.9) is a much faster oven, which can

---

[1] Boralectric heater made by Advanced Ceramic Corporation, Cleveland, Ohio, USA.

Heat exchange mechanism	Equation	
Thermal conduction	Fourier law: $q_k = k\nabla T \; \left[\frac{W}{m^2}\right]$	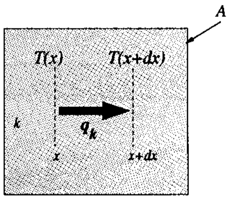
Thermal convection	$q_h = h(T - T_0) \; \left[\frac{W}{m^2}\right]$	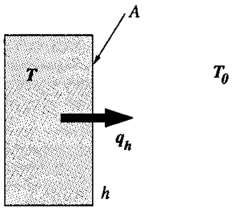
Thermal contact	$q_R = \frac{T_1 - T_2}{R} \; \left[\frac{W}{m^2}\right]$	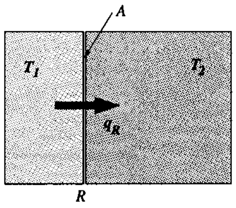
Radiation	$q_\sigma = \sigma\epsilon\,(T^4 - T_0^4) \; \left[\frac{W}{m^2}\right]$	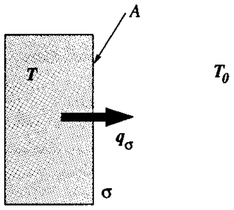

Table 3.1 Heat exchange mechanisms. Physical laws describing the most common encountered heat exchange mechanisms.

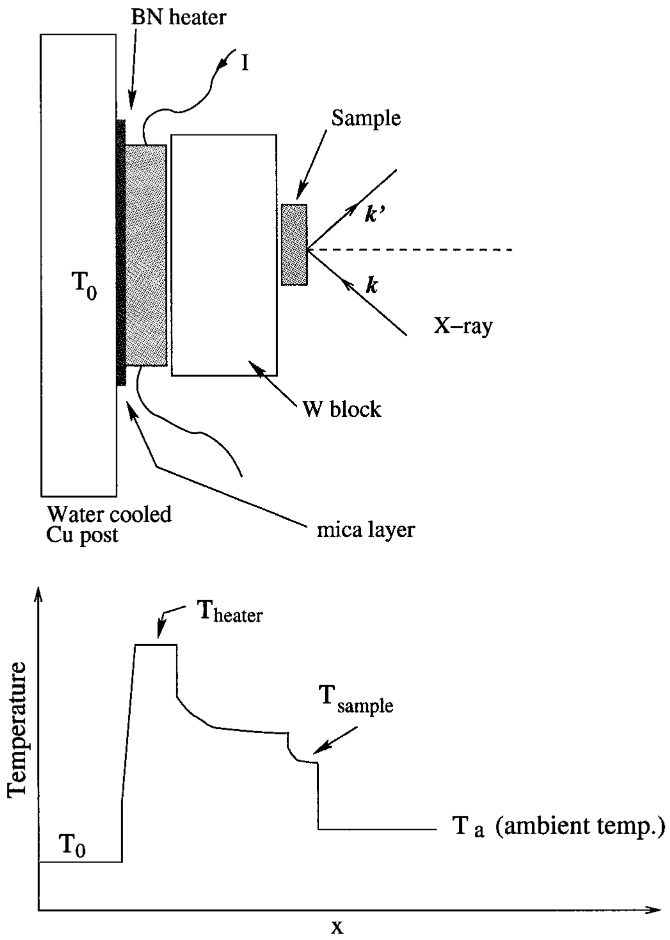

Fig. 3.8 “Hotplate” oven.

provide heating rates of about 70°C/s and slightly slower cooling rates [2]. The samples are melt-spun ribbon segments, typically 30 mm long, 1 mm wide and 25 μ m thick, directly heated by a current. In order to increase the cooling power, the sample is held in a helium atmosphere. Both the sample preparation method and the design of the vacuum furnace are described in [8].

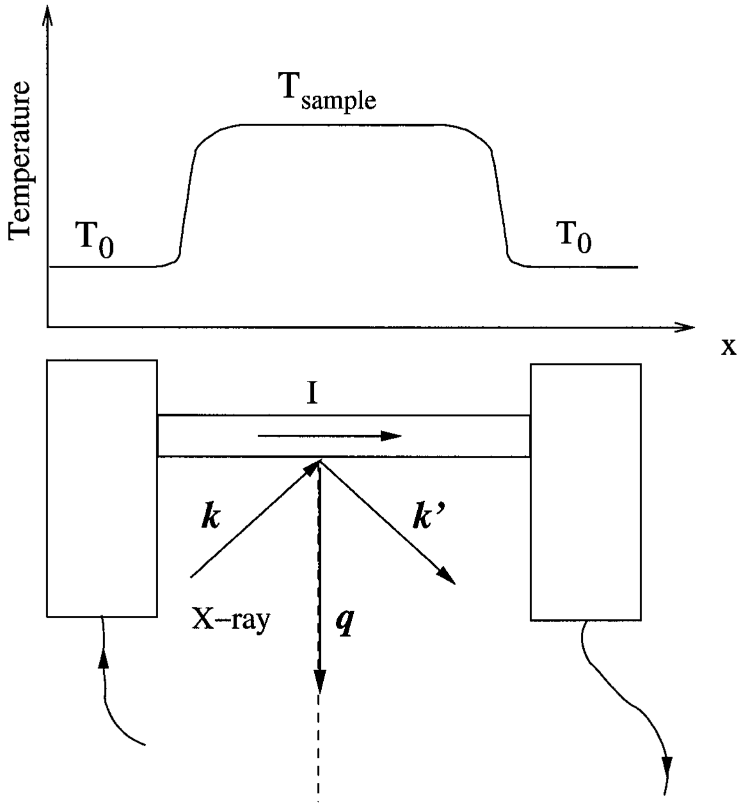

Fig. 3.9 "Ribbon" oven.

The two X-ray ovens are described using simple one-dimensional finite elements thermal models that are solved numerically using the appropriate boundary conditions. To calculate the temperature distribution in an one-dimensional model, the system is divided into a series of finite elements $1, ..., n-1, n, n+1, ..., N$ (Fig. 3.10) with temperatures, $T_1, ..., T_{n-1}, T_n, T_{n+1}, ..., T_N$.

---

[2] The maximum heating/cooling rate is limited by the maximum heating/cooling power. With different experimental arrangements [8] heating rates rates as high as 10^3 K/s were achieved with the same oven for quenches of a few hundred degrees

These temperatures are, of course, time dependent. The discretized thermal problem consists thus, in using a set of known temperatures at time t_i, which can be written,

$$T_{1,t_i}, \ldots, T_{n-1,t_i}, T_{n,t_i}, T_{n+1,t_i}, \ldots, T_{N,t_i},$$

to find the "new" temperatures at time $t_{i+1} = t_i + \Delta t$,

$$T_{1,t_{i+1}}, \ldots, T_{n-1,t_{i+1}}, T_{n,t_{i+1}}, T_{n+1,t_{i+1}}, \ldots, T_{N,t_{i+1}}.$$

In order to simplify the notations, the t_i, t_{i+1} indices will be dropped from both the "old" and the "new" temperatures, and the unknown, "new", temperatures will be denoted by a * upper index:

$$T_1^*, \ldots, T_{n-1}^*, T_n^*, T_{n+1}^*, \ldots, T_N^*.$$

With these notations, the finite-difference approximation to the heat equation for the finite element "n" can be written:

$$-k\frac{T_n^* - T_{n-1}^*}{\Delta x} + k\frac{T_{n+1}^* - T_n^*}{\Delta x} + \frac{P_n}{A} = \rho c A \Delta x \frac{T_n^* - T_n}{\Delta t}. \tag{3.5}$$

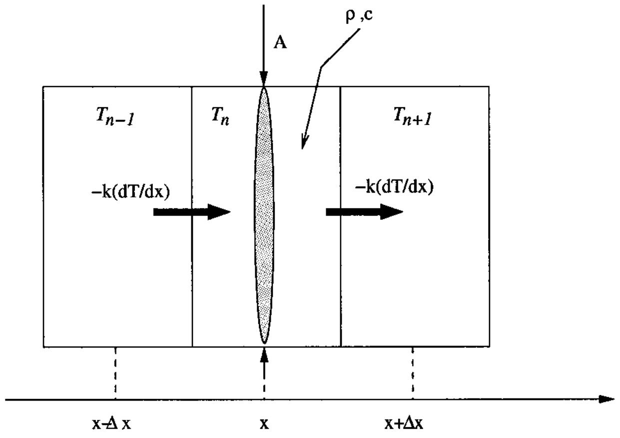

Fig. 3.10 Heat conduction in a 1-dimensional system.

The term P_n, is given by the power generated within the element dx, the power lost via thermal convection or radiation through the side area or other similar power-exchange mechanisms.

In this form it becomes obvious how to write the correct boundary conditions. If the element "n+1", for instance, is in contact with a gas at temperature T_a, then the power flux exchanged with the gaseous atmosphere is $q_h = h\,(T(x + dx) - T_a)$ and the heat equation for this finite element is:

$$-k\frac{T^*_{n+1} - T^*_n}{\Delta x} - h\left(T^*_{n+1} - T_a\right) + \frac{P_n}{A} = \rho c A \Delta x \frac{T^*_{n+1} - T_{n+1}}{\Delta t}. \tag{3.6}$$

Similarly, if the element "n-1" is in contact with an object at temperature T_0 and the contact is described by a thermal resistance "R", then the flux of power at the interface can be written $q_R = \frac{T_0 - T_{n-1}}{R}$, and the discretized heat equation for the element "n-1" becomes:

$$\frac{T_0 - T^*_{n-1}}{R} + k\frac{T^*_n - T^*_{n-1}}{\Delta x} + \frac{P_n}{A} = \rho c A \Delta x \frac{T^*_{n-1} - T_{n-1}}{\Delta t}. \tag{3.7}$$

It is important to observe that the spatial derivatives on the left hand side of the equations were estimated by using the "new" temperatures T^*_j. This is the so-called Euler implicit method [24] and leads to a numerically stable tridiagonal linear system. An "explicit" set of equations, with the derivatives on the left-hand side estimated using the "old" temperatures leads to a simple linear system which can be, however, numerically unstable for some combinations of finite elements Δt and Δx (Appendix A in [8] and [24]). To find the tri-diagonal linear system resulting from the implicit Euler method, an adimensional parameter, the Fourier number can be defined by the relationship $F = \frac{\rho c \Delta x^2}{k \Delta t}$ and the Eq. 3.5 becomes:

$$-T^*_{n-1} + (2 + F)\, T^*_n - T^*_{n+1} + \frac{P_n \Delta x}{kA} = F T_n - \frac{P_n \Delta x}{kA}. \tag{3.8}$$

Some of the terms in the N equations written for all the finite elements will be of course, slightly different, due to the boundary conditions, but the general form for all of them is the same. Solving such a linear system is straightforward and requires a LU decomposition of the system matrix, forward- and backward- substitution and takes $O(N)$ operations [52]. However, the task is even easier, since many modern mathematical computer packages (Mathlab, Yorick) have libraries which include functions to solve tri-diagonal systems.

More details about our finite element models for the hotplate oven and the ribbon oven can be found in Appendix A.

A critical aspect for the use of any thermal model in a temperature control application is, of course, the calibration of the model. Parameters such as thermal contact resistances, convection coefficients, heat capacities and many others can be adjusted by a least-square fitting procedure in order to make the output of the model match the experimental data.

In order to fit the model a known heating power profile is applied and the time evolution of the sample temperature is recorded during the process. Subsequently, the fitting algorithm allows the calculation of a combination of free parameters that makes the theoretical (model output) response agree with the measured one. The thermal models used by the temperature controller in the experiments presented in this thesis are non-linear and they are not even expressed in closed-form. The output function (temperature distribution) is obtained by numerical methods. For this reason, the non-linear Marquardt [5, 52] algorithm is used in order to fit the free parameters.

The power profile used to do the calibration is very important and can significantly improve the accuracy of the thermal model. Fitting the model by using a long constant-power run will most likely result in an accurate theoretical estimate for the steady-state power level, but a poor description of a transient regime. Since the feedback component of the KPPID controller can easily correct for systematic or slow-varying errors in the model output, it turns out that a good qualitative description of the transient regimes is at least as important, if not more important, than an accurate estimate for the power level required to maintain a given temperature. It is essential thus to choose a power profile that has enough "steps" in order to allow an accurate-enough calibration for the transient regimes.

A calibration run for the "hotplate oven" is shown in Fig. 3.11. The applied power was stepped through four levels. The free parameters (the thermal resistances at the contacts between different pieces and the convection coefficient h) are calculated using the Marquardt non-linear least squares fit algorithm [5, 52].

The dots are the measured temperatures while the solid line is the model output after calibration. As it can be seen in the inset the calibration errors are sometimes significant for the simplified model that was used but, as it will become more clear in the following sections of this chapter, these errors are small enough to be corrected "on the fly" by the KPPID feedback algorithm. What is important, is to have good-enough accuracy and be able to solve the model in real time for feedforward temperature control at the same time. The thermal models presented in this section are are a compromise between accuracy and speed and they resulted after several iterations. More details about the calibration procedure for

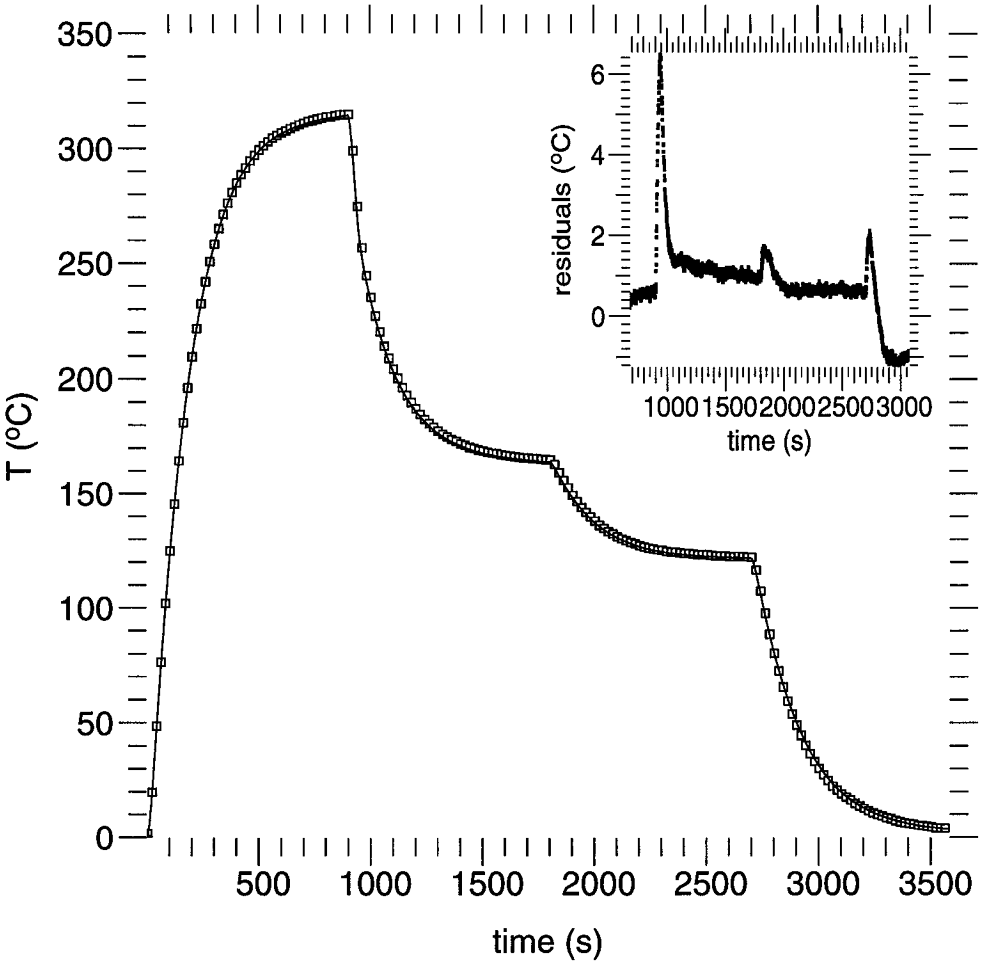

Fig. 3.11 Calibration run for the "Hotplate" oven.

the "hotplate oven" are given in Appendix A.

Feedforward

The actual feedforward procedure consists of using the calibrated model to find the power profile which leads to the desired temperature profile or, at least, to the closest possible fit of the desired temperature profile, given practical constraints such as the maximum heating and cooling power available in the system. Such an "inverse" problem is generally difficult to solve. However, one can gain some insight about what the actual power profile should look like, by considering very simple "toy-systems", which can be solved analytically. If a block of density ρ, heat capacity c, volume V, surface area A, heated by a heating element providing a power density p is small enough and/or has a high enough thermal conductivity, the temperature T may be considered constant throughout the volume (Fig. 3.14). Considering that the only heat loss mechanism is thermal convection through a convection coefficient h and the surrounding atmosphere at T_0, the heat equation can be written:

$$\rho c V \frac{dT}{dt} = pV - hA(T - T_0). \tag{3.9}$$

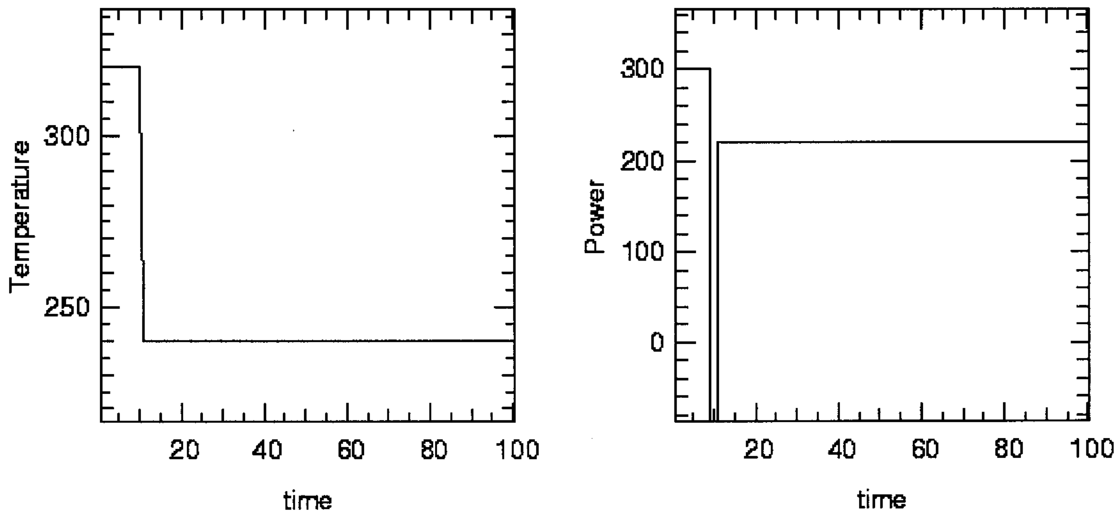

Fig. 3.12 Feedforward: Power profile (right panel) leading to the temperature step shown in the left panel for the "toy-model" Eq. 3.9

Eq. 3.9 can be used to calculated the heating power leading to a known temperature profile. With the heating power profile shown in the right panel of Fig. 3.12, the temperature follows the ideal "step" shown in the left panel of the same figure. However, such a profile is of course not realistic. The maximum cooling power required to achieve such a fast step becomes arbitrarily large as the step becomes shorter and an ideal temperature step would require an infinite amount of cooling power. Considering, for instance, that the fastest cooling is achieved by turning off the heating power and letting the system cool down by thermal convection, the temperature and the power profiles shown in Fig. 3.13 become the more "realistic" estimates for the "best" temperature quenches that can be obtained with this "toy-system".

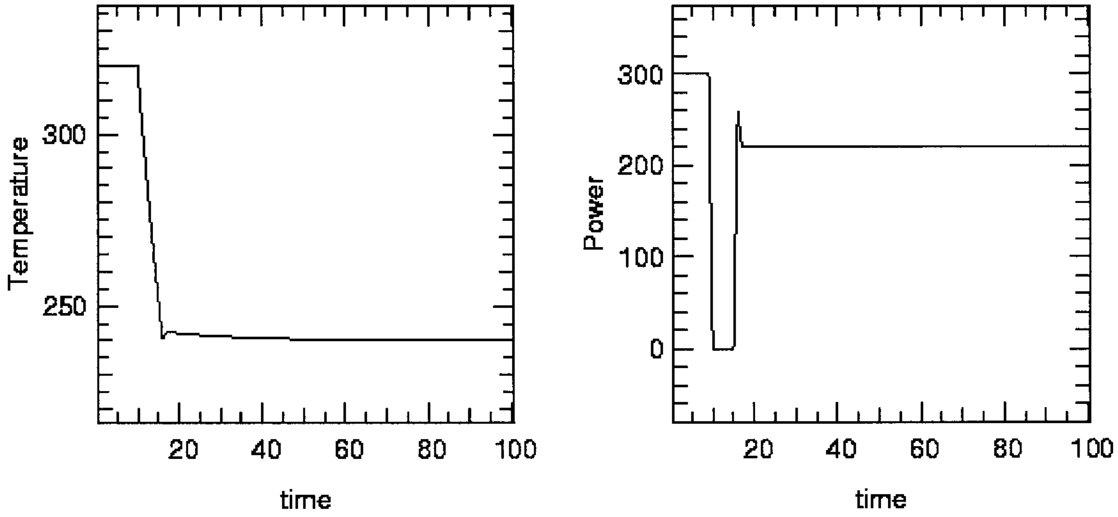

Fig. 3.13 Feedforward: The best achievable temperature profile (left panel) is often limited by practical constraints such as the maximum cooling power available in the system.

To solve the "feedforward problem" for a more complicated system, like the "hotplate oven" or the "ribbon oven", a power profile similar in shape with the one represented in Fig. 3.13 is obtained by a fitting procedure, using the Marquardt non-linear least squares fit algorithm [5]. The power profile is described in terms of a few parameters and the fitting algorithm is subsequently applied to find the set of parameters which lead to the desired temperature profile. The best results for temperature quenches were obtained with power profiles described by two power levels corresponding to the initial and final (steady-state) temperatures and a set (8,16,32, etc.) of intermediate power levels. The

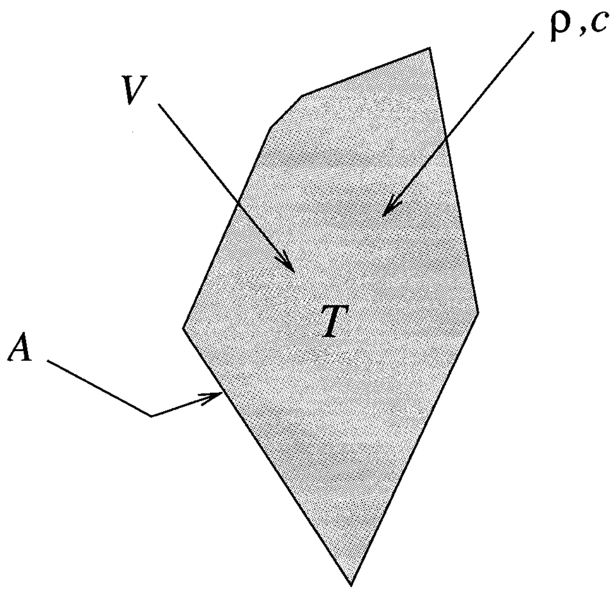

Fig. 3.14 Feedforward: Calculating the power profile leading to a target temperature profile for a simple system - a block of heat capacity c and uniform temperature T

feedforward procedure described above is schematically represented in Fig. 3.15. Ideally, the temperature would follow a perfect step function, represented in the upper-left panel. However, due to practical constraints mentioned above, the best achievable temperature profile is the calculated by using a thermal model and the non-linear least-square fitting procedure. The result (both the temperature and the power profile) is shown in the lower panels of Fig. 3.15. The power profile in the lower-right panel is optimized to minimize the response time of the temperature quench while avoiding any non-negligible temperature undershooting. The initial and the final steady-state power levels as well as 32 intermediate values were found by a (long!) fitting procedure. The corresponding temperature response is shown in the lower-left panel of the figure.

With the temperature and power profiles calculated by the feedforward procedure the experimental goal for the control process becomes less "ambitious" albeit more "realistic", and that is to follow the "feedforward" temperature profile shown in Fig. 3.15. The feedback algorithm corrects small errors in the calculated profile but this small corrections will generate fewer problems such as temperature oscillations or slow drifts.

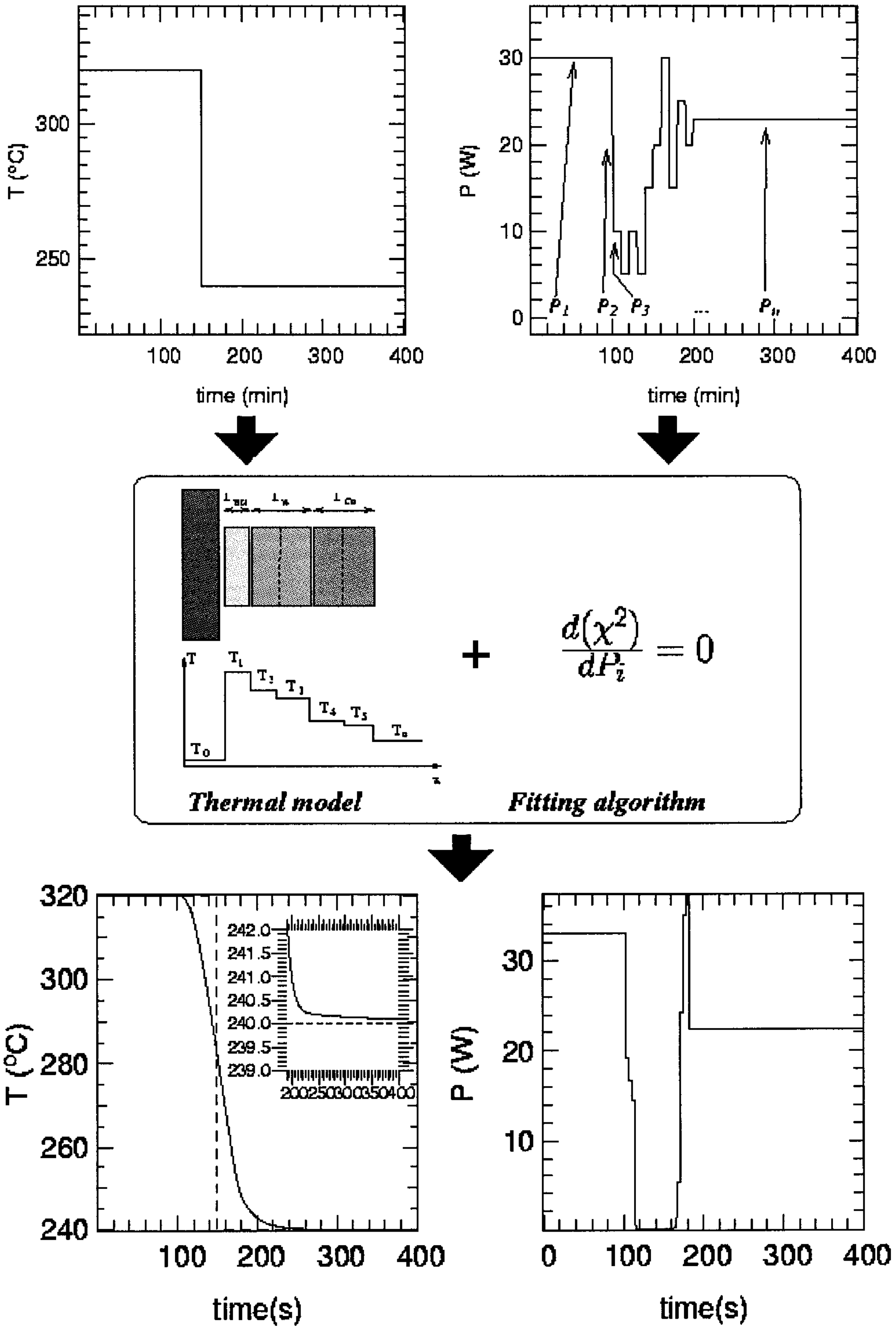

Fig. 3.15 Feedforward: power profile and corresponding temperature profile for a temperature quench from 320°C to 240°C.

3.2.3 Temperature measurement. Kalman filtering

A precise temperature measurement is key to an effective and accurate temperature control. With a noisy temperature probe a temperature controller reacts to the random fluctuations in the readings and, as a consequence, the power output keeps oscillating. At the same time, some of the experimental systems require contact-free temperature probes which have high intrinsic levels of noise. In the "ribbon oven" described in the previous section, the sample has such a small "thermal mass" (i.e. small heat capacity, high thermal conductivity) that any direct-contact temperature probe like a thermocouple or a thermistor, would disturb the temperature distribution and the thermal properties of the sample. As a consequence the sample temperature is measured with an IR optical pyrometer. The instrument is a powerful temperature probe and is described in [8], but the problem with any IR device is the high intrinsic noise. The temperature readings for a constant (or quasi-constant) temperature run with the "ribbon oven" are show in Fig. 3.16. With such a high level of noise, any feedback system will basically keep oscillating between the maximum and minimum heating power if the control gain is high-enough to ensure a reasonably fast response time.

In order to reduce these limiting effects of the noise on the temperature control, a better estimate of the sample temperature is obtained by a Kalman filtering process. Kalman filtering is a powerful technique which allows filtering of measured physical quantities in a dynamical system by using the prediction of a model and direct measurements.

The basic idea behind a Kalman filter is extremely simple [45] and is represented in Fig. 3.17. If there are two estimates T_1 and T_2 with standard deviations σ_1 and σ_2 for the same physical quantity (in this case, the sample temperature) T, then a better estimate for the actual value is given by the weighted average:

$$T_{kal} = \frac{\sigma_2}{\sigma_1 + \sigma_2} T_1 + \frac{\sigma_1}{\sigma_1 + \sigma_2} T_2. \tag{3.10}$$

This estimate is better, in the sense that its standard deviation σ_{kal} is smaller than either σ_1 or σ_2:

$$\frac{1}{\sigma_{kal}} = \frac{1}{\sigma_1} + \frac{1}{\sigma_2}. \tag{3.11}$$

The two estimates for the quantity T are generally the output of a theoretical model

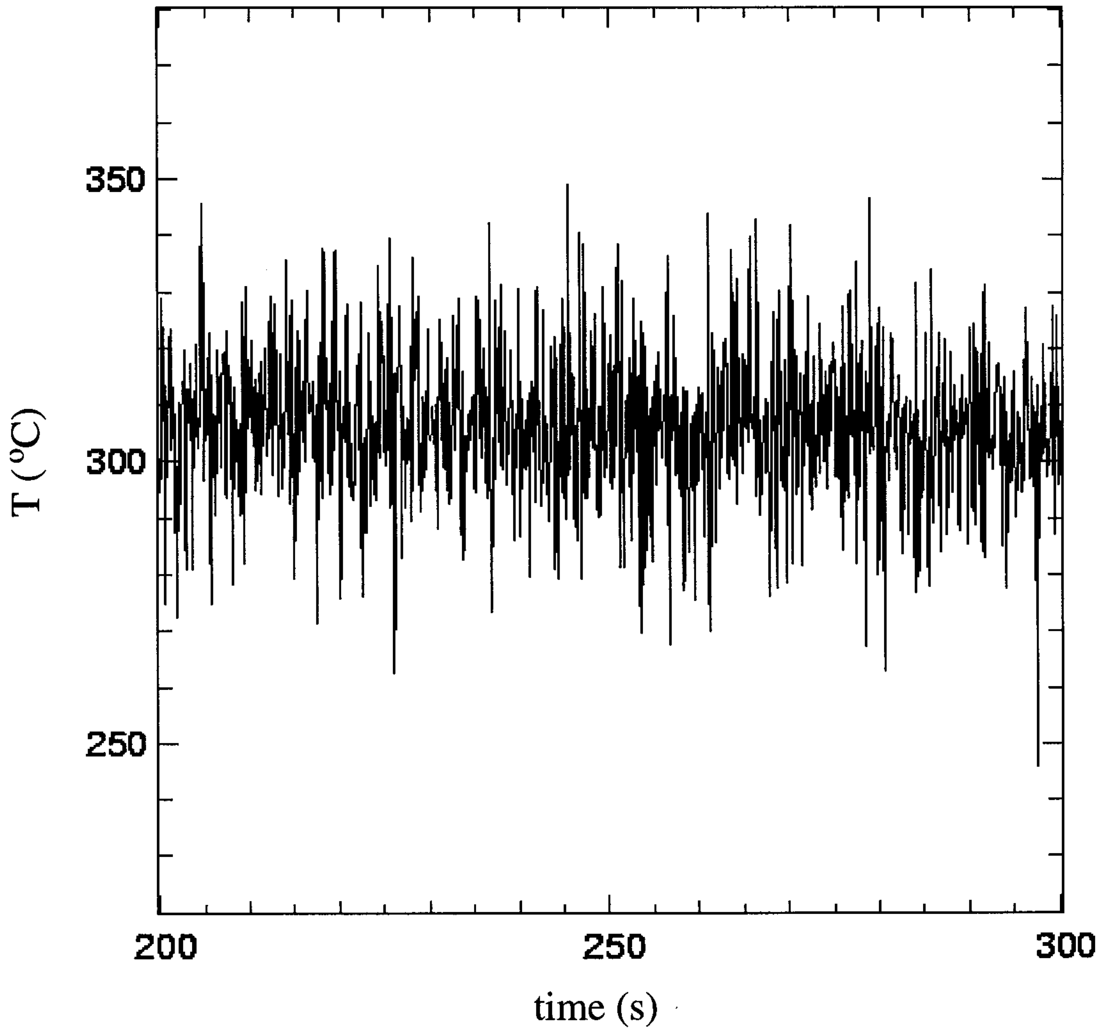

Fig. 3.16 Temperature readings recorded with an IR pyrometer in the "ribbon oven". The high level of noise is an intrinsic problem with many contact-free temperature probes and limits the performance of a temperature controller.

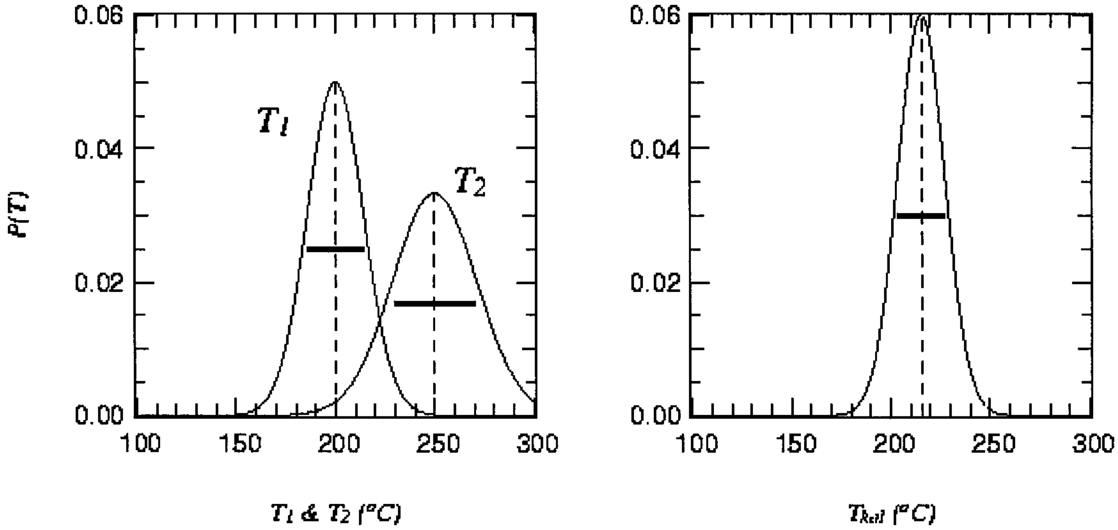

Fig. 3.17 Kalman filtering:

and a measurement. The basic idea behind the Kalman filter, thus, is that a better estimate for the sample temperature can be obtained by using the already existing model to calculate a theoretical value for the temperature and the (noisy) temperature readings. In the equation 3.10 and 3.11, a pure Gaussian noise is assumed for both the measured and the calculated values for the temperature. While this is a reasonable assumption for the measurements, it is clear that in reality, the model output will be subject to (sometimes important) systematic errors as well. In order to compensate for the systematic errors in the calculated temperatures, a "two-stage" Kalman filtered value was calculated. The Kalman estimate T_{kal} is calculated in the first stage by a Kalman filter using as an input the value predicted by the finite difference model of the oven T_{mod} and the measured temperature T_{meas} (with their respective errors). A second Kalman filter corrects for systematic errors in the model output. A correction term, ΔT is estimated using as an input the error of the first stage Kalman filtering ($T_{kal} - T_{meas}$) and the "belief" that ΔT varies slowly in time. The double stage Kalman filtering algorithm is summarized by the block diagram shown in Fig. 3.18.

The results shown in Fig. 3.19 demonstrate the power of this Kalman filtering technique. The thick solid line is the double-stage Kalman filtered estimate for the temperature and the dots are the actual measurements obtained with an IR optical pyrometer. This estimation is obtained with a thermal model which can have systematic errors as high as 2-3°C and

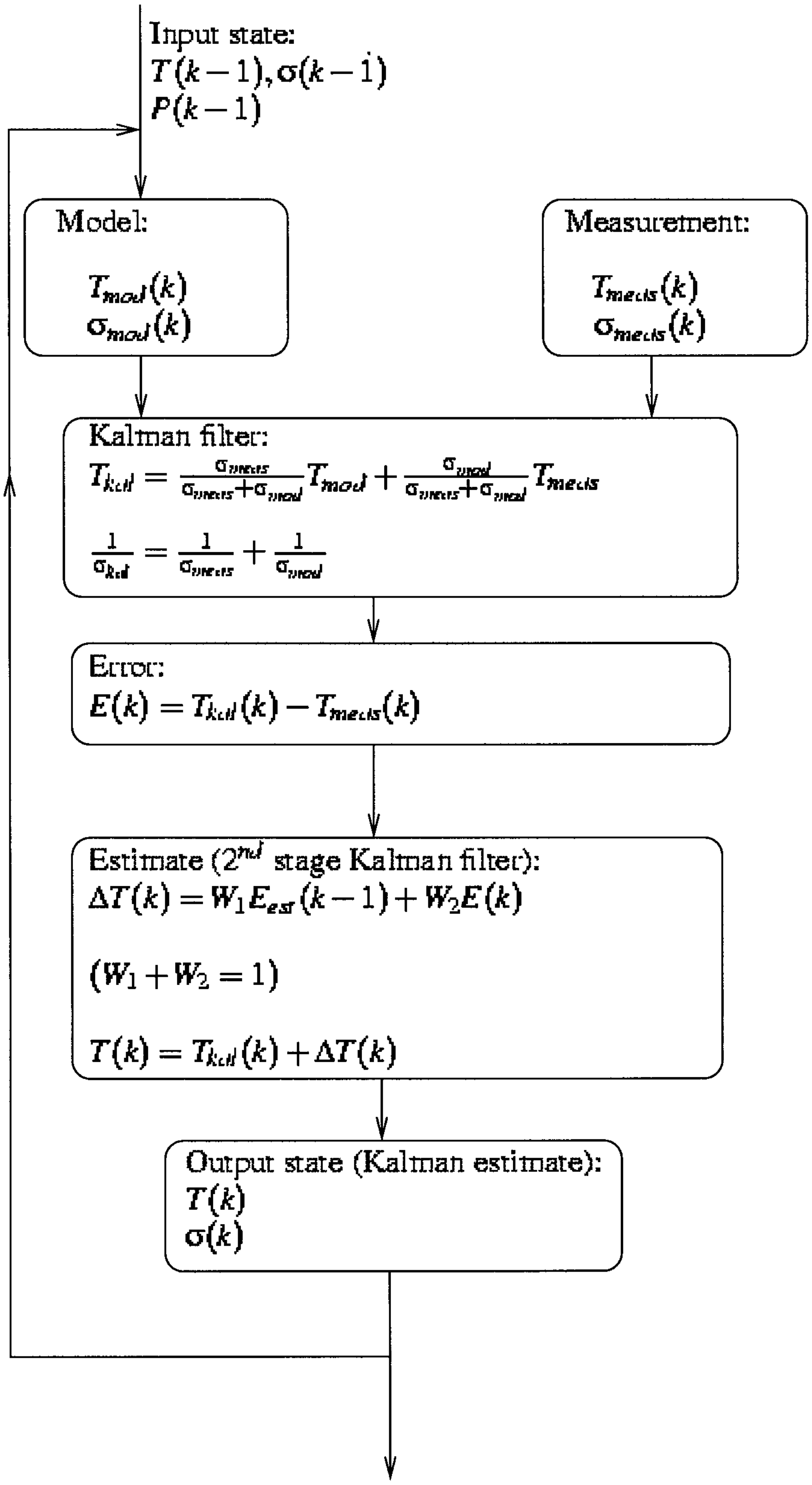

Fig. 3.18 Block diagram of the "double-stage" Kalman filtering algorithm used by the KPPID controller to reduce the effects of the noise on the temperature estimates.

maximum errors as high as 6°C.

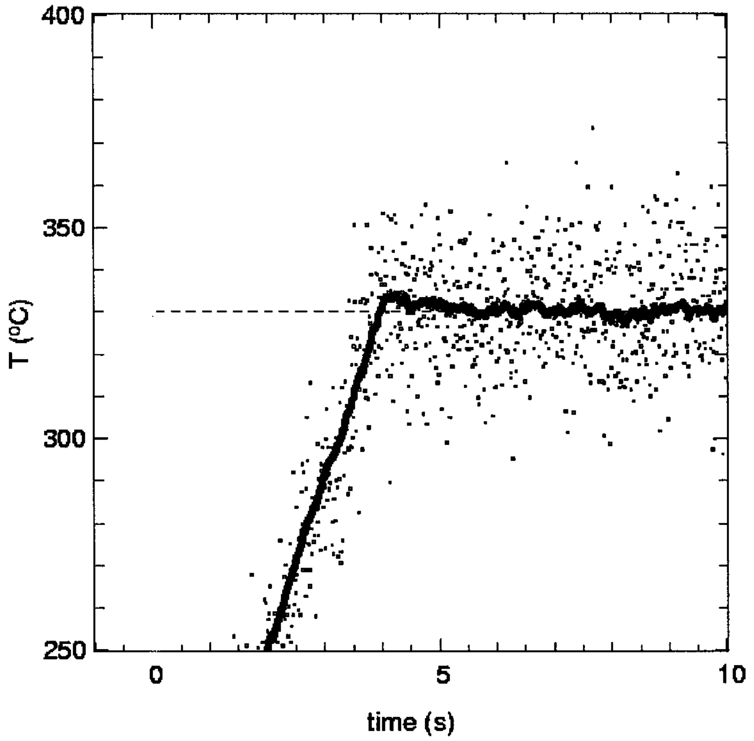

Fig. 3.19 Temperature step with the "ribbon oven". The dots are the temperature readings and the solid line is the Kalman estimate for the sample temperature.

3.3 Design of the KPPID controller

The main idea behind the KPPID temperature control is to try to follow the feedforward temperature profile by outputting the calculated power profile. The role of the classic PID algorithm is only to provide a "small correction" to this power and compensate for random and/or unknown factors that affect the actual temperature of the sample. The double-stage Kalman filter runs continuously and produces the filtered estimates for the sample temperature. The KPPID algorithm was implemented on a personal computer system running Linux connected to a 16 bit Keithley data acquisition board [22].

In Fig. 3.21 we show a typical quench obtained with the hotplate oven. The calculated (feedforward) power and temperature profiles are the solid lines. The short segment to the left shows the maximum cooling rate for our oven (about 1 °C/s) and this shows that our

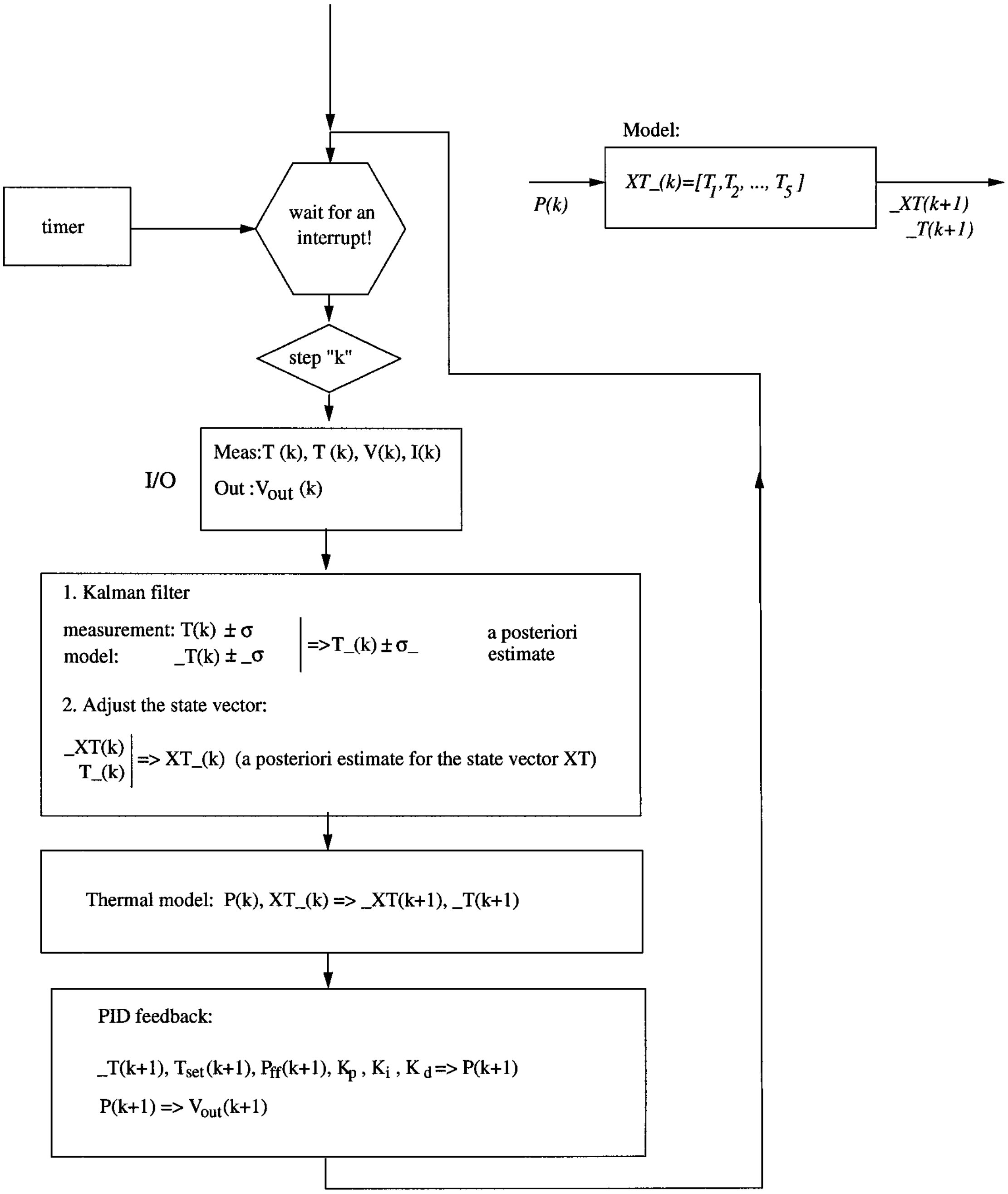

Fig. 3.20 Flowchart for the KPPID algorithm.

calculated temperature profile is indeed close to being optimal. The measured values for the temperature and the heating power are represented by the dots. For clarity, only one in ten measurements have been shown in the main graph. However, all the data points have been shown in the insets.

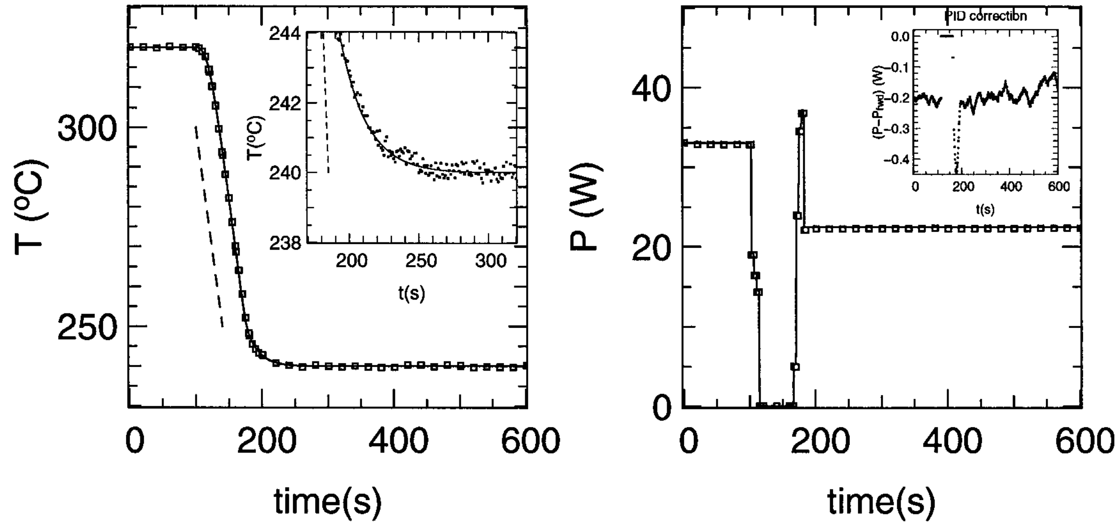

Fig. 3.21 KPPID quench of a Cu_3Au sample from 320°C to 240° in the "hotplate oven". The dots are the measured values. The dashed line in the left panel shows the maximum cooling rate for the oven

Similar results were obtained with an earlier version of the KPPID temperature controller for the ribbon oven. The NiZr metallic glasses ribbons were heated from room temperature to 350°C to study their crystallization process (Fig. 3.22). Due to the small sample size, any direct-contact temperature probe is impractical. An infrared (IR) optical pyrometer was used as a temperature probe. The noise on the temperature readings (dots) is partially due to the intrinsic noise of IR devices and partially to the very short integration time. In order to obtain an accurate control for temperature steps of 300°C in 4 s, a time step of 10 ms was used. The main benefit of the Kalman filter is that even with such high levels of noise on the temperature readings, the "smooth", filtered estimate of the actual temperature, allows an efficient control.

The block diagram for the KPPID controller is shown in Fig. 3.23. The "core" of the system is the thermal model used to calculate the feedforward power profile and Kalman-filtered values for the temperature.

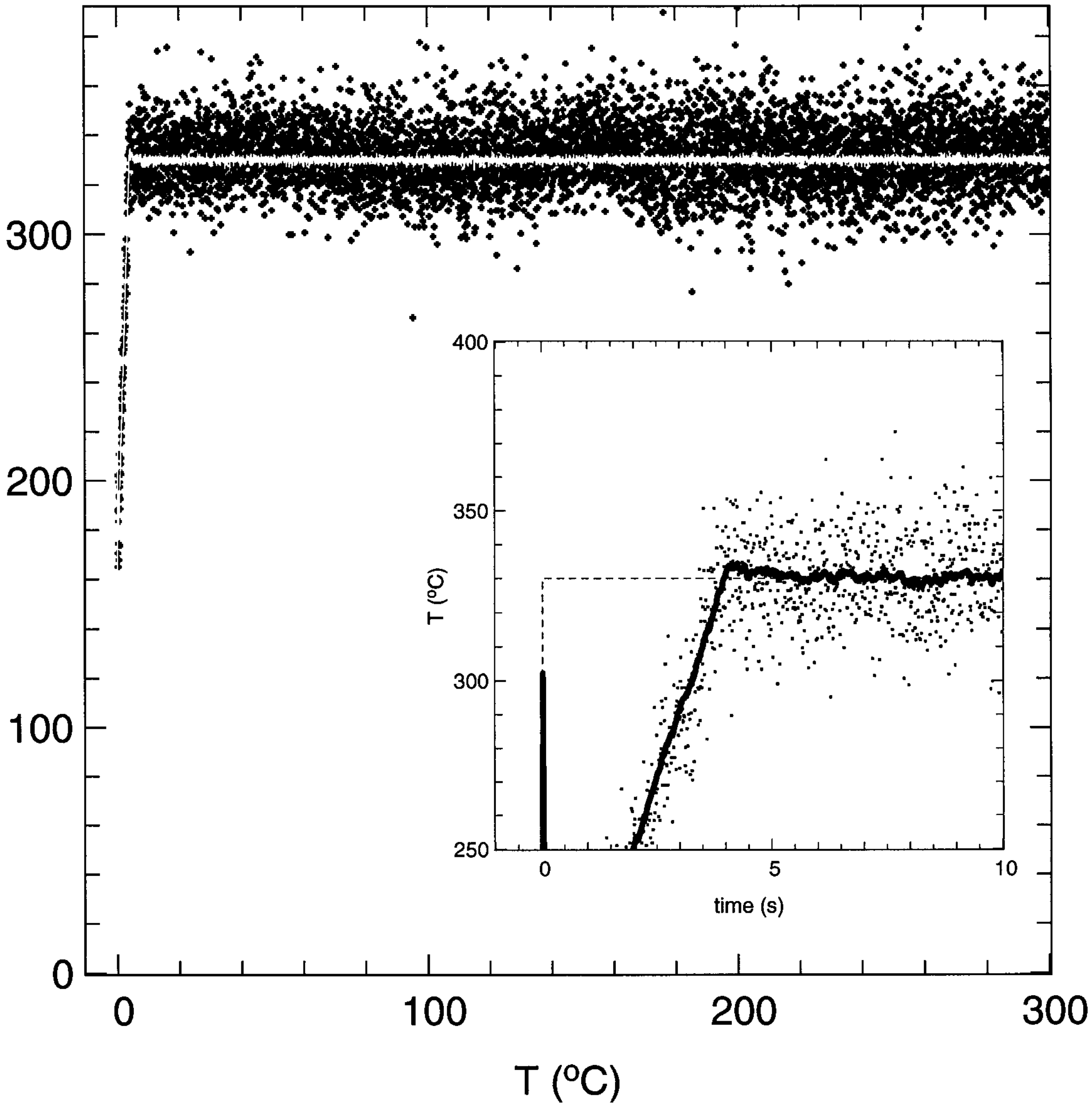

Fig. 3.22 KPPID temperature step of a NiZr metallic glass ribbon from room temperature to 350°C. The dots are the measured values, the continuous line is the Kalman estimate for the sample temperature.

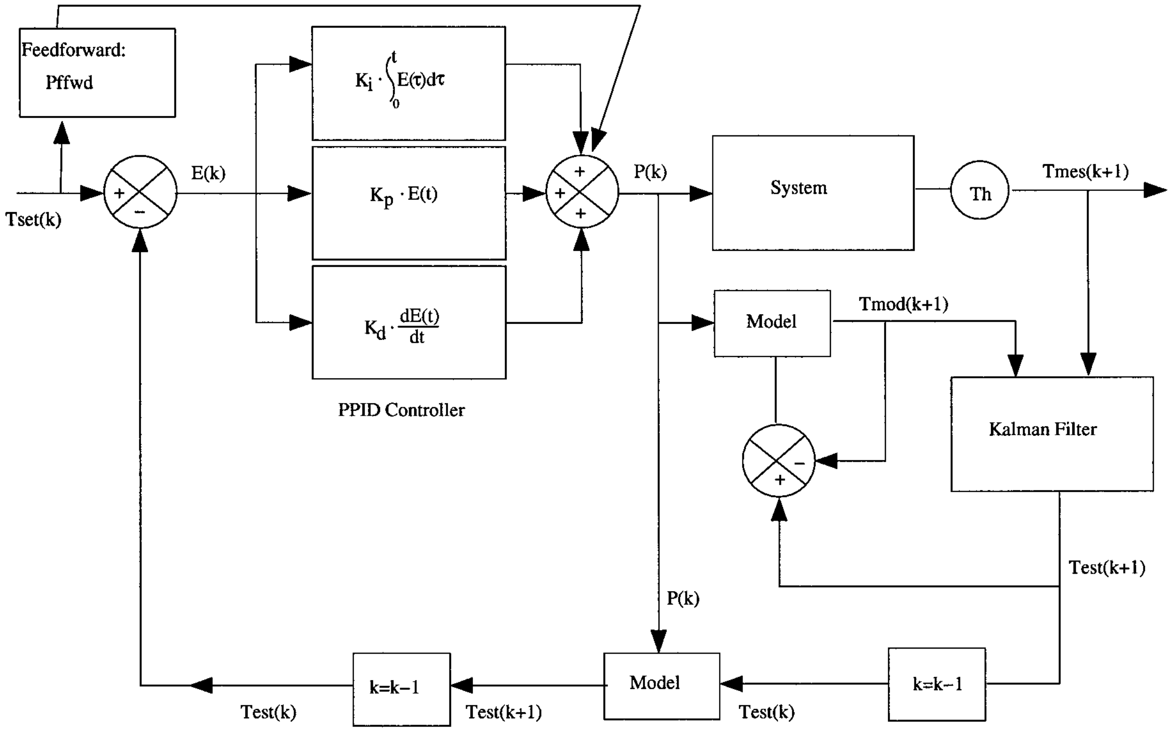

Fig. 3.23 Block scheme of the KPPID control algorithm. At each time step "k", the power output is the sum of the feedforward power P_{ffwd} and a PID correction which is set to minimize the error function E(k). The error function is the difference between the set and the estimated temperature, $E(k)=T_{set}(k)-T_{est}(k)$. The optimal estimate for the temperature, T_{est}, is calculated by the Kalman filter as a weighted average of the measured value, T_{meas}, and a theoretical value output by the model, T_{mod}. The Kalman filter has also an "adaptive" role. The output of the model is shifted and its predictions improve with time.

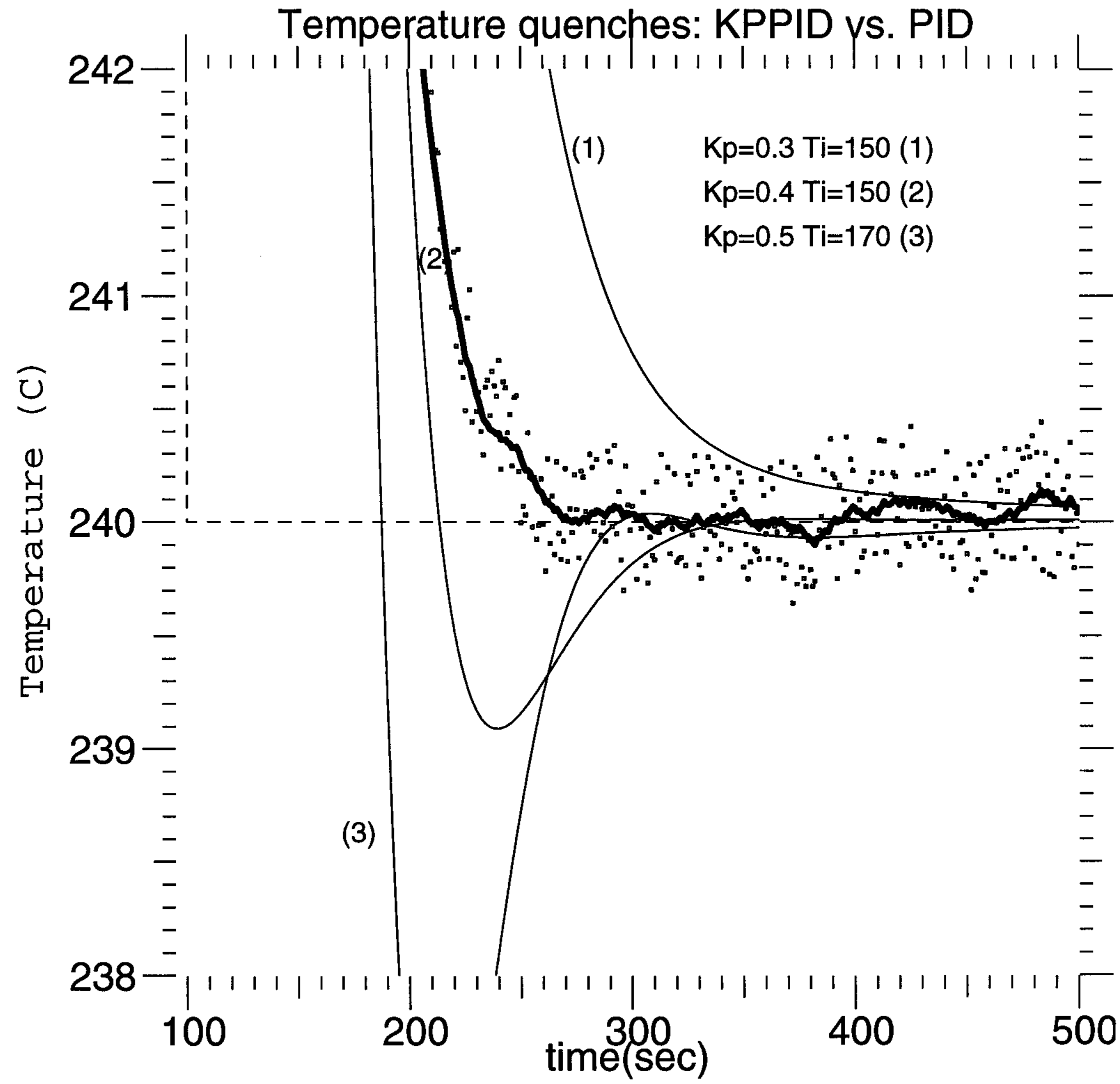

Fig. 3.24 The measured values for the sample temperature (discrete points) and the Kalman filter estimate (thick solid line) during a KPPID temperature quench are shown together with "standard" PID responses tuned for no undershoot (1), fastest response (3), and "reasonable compromise" between the two cases (2).

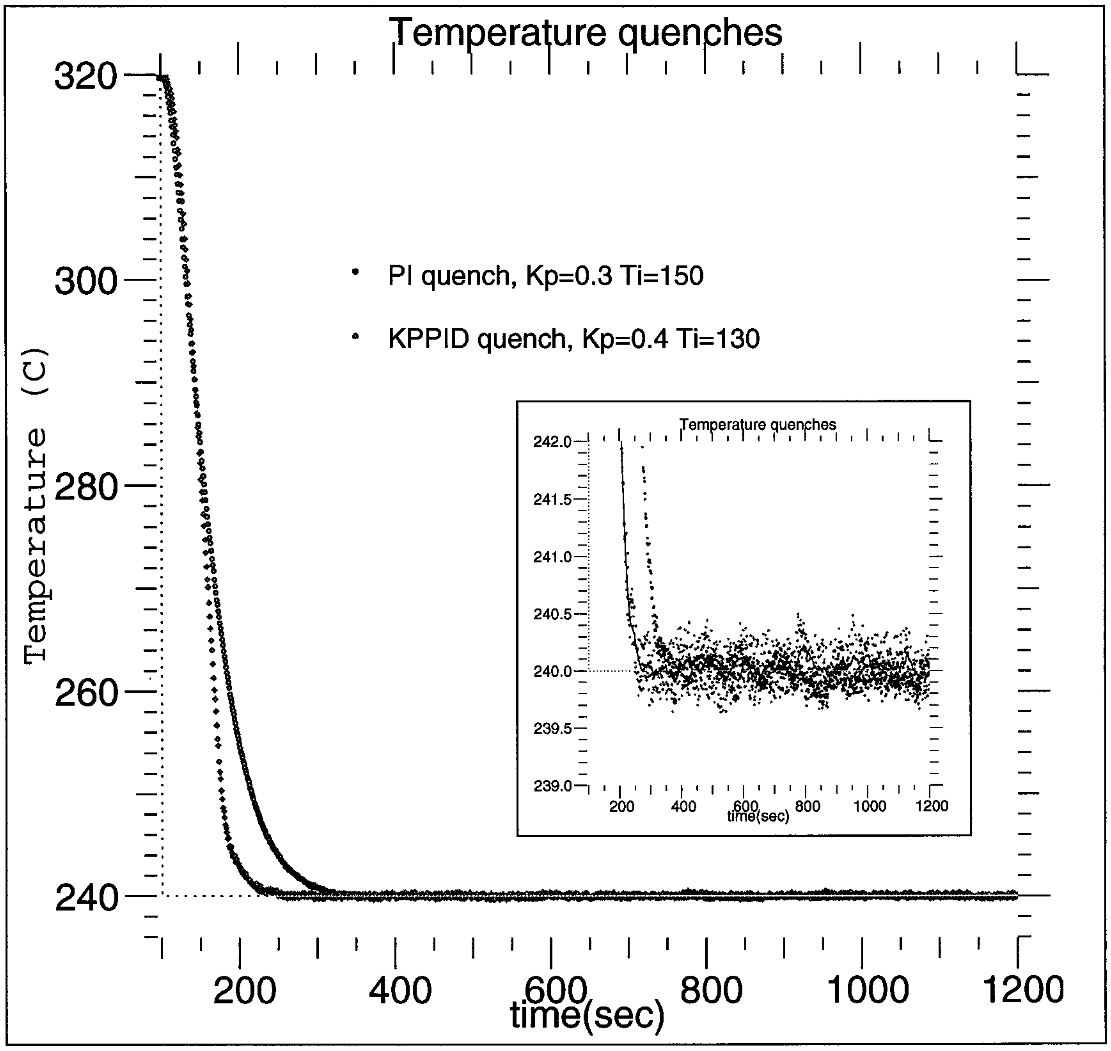

Fig. 3.25 KPPID temperature quench from 320°C to 240°C and PID temperature quench between the same temperatures tuned for fastest response with no undershooting.

3.4 Some applications of the KPPID controller

The main results of this thesis, the coherent X-ray studies of the order-disorder phase transition in Cu_3Au are presented in detail in Chapter 4. In order to do coherent X-ray diffraction experiments, the KPPID temperature controller was used to quench the sample through the phase transition and to keep it at a constant temperature during the ordering process. In this section we will present another application of the KPPID temperature controller, the time-resolved X-ray studies of polymorphic crystallization in $NiZr_2$ metallic glasses.

3.4.1 Experimental Details

The Ni-Zr samples were prepared by Zaven Altounian and his coworkers [2]. The alloys were obtained by arc melting 99.99% pure Ni with 99.9% pure Zr. In order to ensure homogeneity, samples were melted four to five times, under Ti-gettered Ar gas. The glassy ribbons were produced by the rapid solidification technique of melt-spinning under a helium atmosphere. Melt-spinning parameters (wheel speed, crucible orifice diameter and distance from wheel, RF power) were carefully controlled in order to maintain the same quench rate for all samples. Ribbons were produced with a typical cross-section of $0.02 \times 2\ \mathrm{mm}^2$. Reproducible consistency between actual and nominal sample composition values was established by electron microprobe analysis. An automated powder X-ray diffractometer using Cu K_α radiation was used for primary structural studies of the glassy alloys and their crystallization products. Calorimetry studies were done with a calibrated Perkin-Elmer DSC-2C differential scanning calorimeter (DSC), under a flow of oxygen-free argon gas. DSC isochronal scans were done with a heating rate of 40 K/min.

Two types of Ni-Zr samples have been studied in these experiments. Pure $NiZr_2$ glasses have been prepared as described above. By melting the alloy in a H_2 atmosphere, hydrogenated $(H)NiZr_2$ samples were prepared as well.

The time resolved X-ray scattering measurements were performed using a dedicated spectrometer recently commissioned on the MIT-McGill-IBM insertion device beamline at the Advanced Photon Source. The main characteristics of this spectrometer have been described in Ref. [51]. Briefly, X-rays produced by a 2.4 m 72-pole undulator are reflected off a silicon mirror and a diamond (111) crystal to obtain monochromatic X-rays at 7.66 keV (1.619 Å) having a relative bandwidth $\Delta\lambda/\lambda = 6.2 \times 10^{-5}$. Between the monochromator and the sample chamber, two sets of slits separated by 1.3 m are used to adjust the beam size and eliminate parasitic scattering. An ion chamber monitors the incident X-ray beam intensity. For the experiment described here, the X-ray beam had dimensions of $0.6 \times 0.9\ \text{mm}^2$ and a flux of $\sim 5 \times 10^{12}$ photons per second for a storage ring current of 100 mA.

Scattered X-rays were collected by a linear photo-diode array detector (PSD) mounted on the 2θ arm of a 4-circle goniometer. This detector is described in further details in Ref. [59]. The detector was located 75 mm from the sample and from this distance could acquire a range of nearly ~17° in 2θ. A schematic diagram of X-ray spectrometer is shown in Fig. 3.26.

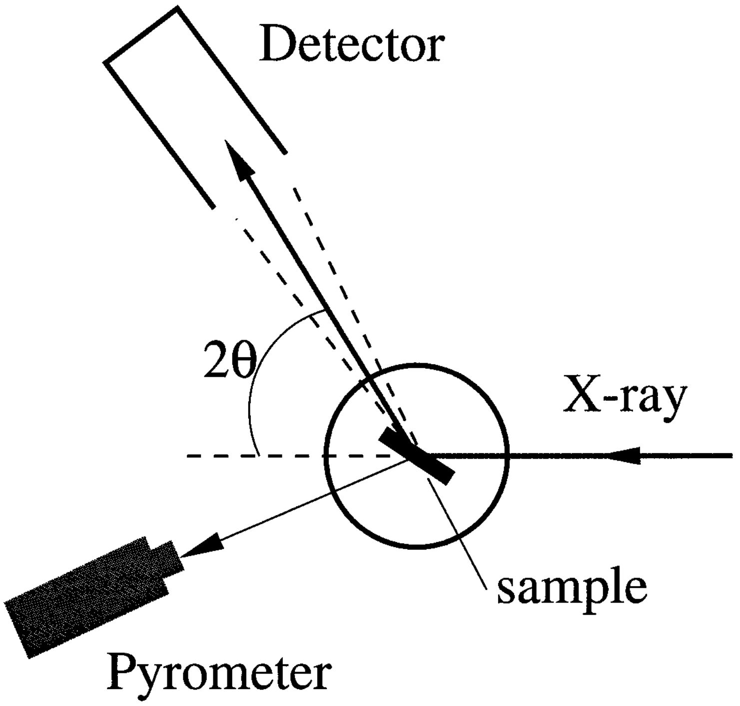

Fig. 3.26 Time-resolved X-ray scattering setup

Samples were loaded inside the "ribbon oven" described earlier in this Chapter (Fig. 3.9). The ribbon samples were cut down in pieces approximately 3 cm long which were held in place between the two electrical terminals. One of the terminals is spring-loaded to maintain a constant tension in the ribbon and to compensate for thermal expansion. The samples were heated by a direct current and the temperature was monitored using a fast pyrometer. The vacuum furnace is equipped with a 10-mm wide Be window covering approximately

200° in 2θ and mounted on the θ circle of the goniometer.

3.4.2 Experimental results: crystallization of Ni-Zr metallic glasses

A metallic glass is formed by the sudden cooling of a melt such that detectable crystallization is avoided [8]. The glassy state is thus a non-equilibrium state and the time taken for a detectable crystallinity to form from the undercooled melt is schematically show in Fig. 3.27.

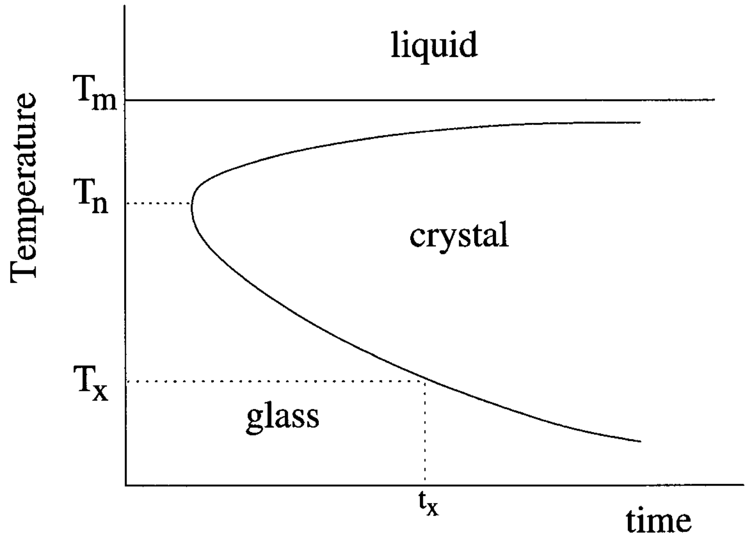

Fig. 3.27 Temperature-Time-Transformation (TTT) diagram for crystallization from an under-cooled melt. The crystallization time at a temperature T_x is t_x.

Above the melting temperature T_m the metal is in a liquid state. Just below T_m the crystallization is very slow because of the small thermodynamic driving force (free energy difference between the glassy state and the crystalline state). At lower temperatures, the thermodynamic force is higher but the atomic mobility is reduced as well. The two competing mechanisms lead to the "nose" profile shown in Fig. 3.27. The maximum crystallization rate occurs at T_n, the temperature of the "nose".

In the present experiments, the samples were prepared in their amorphous state and held at room temperature where the crystallization time can be considered, for any practical purpose as being infinite. The crystallization was triggered by sudden temperature steps like the one shown in Fig. 3.22 to temperature close to the "nose" where the crystallization process is much faster and happens over time scales of a few seconds or less. This is the reason for which a very fast and accurate temperature control system is required for such studies.

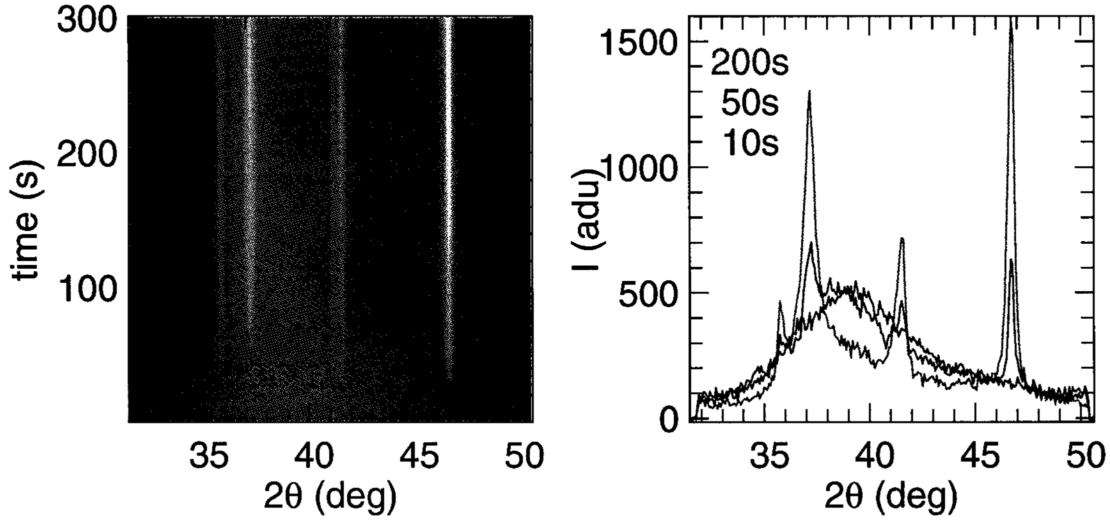

Fig. 3.28 Time-resolved X-ray studies of polymorphic crystallization in $NiZr_2$ metallic glasses.

A typical crystallization process can be seen in Fig. 3.28. The initial, amorphous state, creates a broad X-ray peak centred around a value of θ give by

$$sin\left(\frac{2\theta}{2}\right)=\frac{\pi}{kd}, \tag{3.12}$$

with d, the average inter-atomic distance. During the crystallization process the amorphous peak vanishes and the Bragg peaks associated with the new crystalline structure appear instead.

An interesting result of these experiments can be seen in Fig. 3.29. The two graphs show the X-ray scattering pattern at three different times after a temperature step for a pure $NiZr_2$ sample (upper graph) and a hydrogenated $(H)NiZr_2$ sample (lower graph). The only noticeable difference between the two graphs is the absence of the Bragg peak around $2\theta \simeq 31°$ for the hydrogenated sample. This Bragg peak corresponds to the ZrO_2 phase. The formation of oxides during crystallization of metallic glasses containing Zr in generally inevitable. Our analysis of rapid heating scans shows that for amorphous $NiZr_2$, the first crystallization product is cubic ZrO_2. However, the hydrogenated $(H)NiZr_2$ samples do not show the formation of an oxide during their crystallization process. A possible explanation could be that the hydrogen and oxygen desorb as water from the hydrogenated samples.

3.5 Conclusions

To have a full understanding on the complex mechanisms taking place during the crystallization of metallic glasses or in other non-equilibrium systems requires, of course many different experimental and theoretical investigations. The goal of this chapter was to prove that time-resolved X-ray studies combined with a fast and accurate temperature tracking system is an invaluable tool to study structural changes at atomic length scales in such non-equilibrium systems. The general approach that was adopted during the development of the KPPID controller presented in this chapter was to use the sample furnaces that were available in our labs and design the "best possible" temperature controllers for them. The results were encouraging and enabled experiments like the study on the crystallization of Ni-Zr metallic glasses described above or the study of the ordering dynamics in Cu_3Au which will be presented in the following chapter. In both studies the limiting factor in obtaining even better temperature quenches, with shorter response times, or better accuracy in avoiding temperature over or under shooting is the feedforward part of the algorithm, or the ability to accurately predict the correct power output. A natural approach to improve these results would be, of course, to design better thermal models which predict more accurately the temperature distribution in the sample, especially during the transient regimes. This approach is currently being used in designing several experiments to investigate early-time behavior during processes such as the order-disorder phase transition in Cu_3Au.

Another possible approach in obtaining better experimental results is to "start from scratch" and design an "controllable-oven" which could easily be modeled. With the thermal modeling techniques presented in Section 3.2.2, one can expect that the behavior of a very simple and highly symmetric sample oven could be more easily predicted and this would of course lead to a better temperature control.

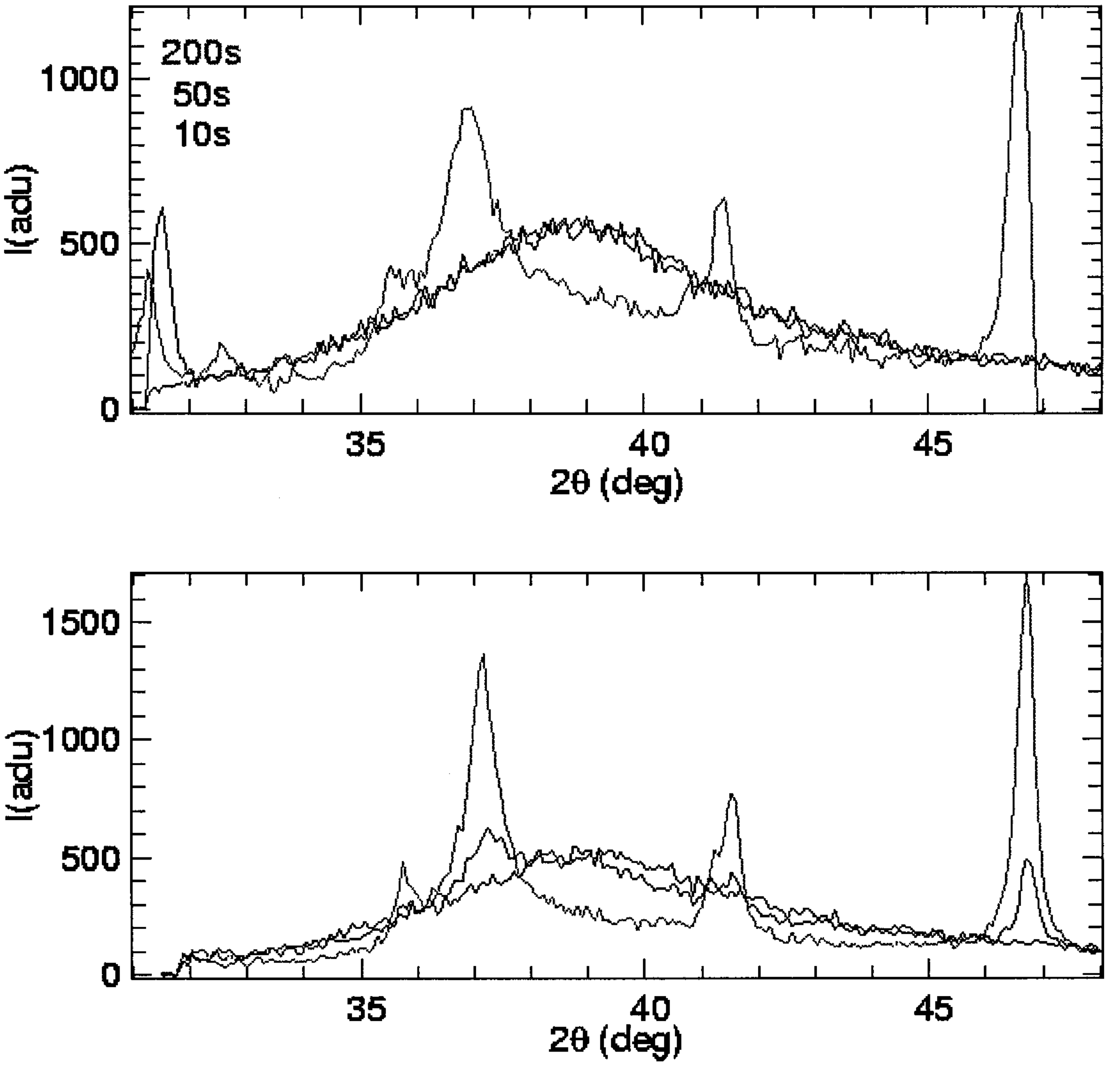

Fig. 3.29 Influence of hydrogen in the crystallization process. In NiZr samples, the first crystallization product is ZrO - Bragg peaks around 30-32 ° in the upper graphs. During a similar process, a hydrogenated (H)NiZr sample doesn't show the formation of an oxide phase.

Chapter 4

X-ray Studies of Order–Disorder

4.1 Introduction

With the advent of third generation synchrotron X-ray sources, many new types of diffraction experiments are now possible. A class of such experiments are those exploiting coherence. Observation of static speckle patterns in the scattering of X-rays from disordered systems was the first step in using partially coherent synchrotron beams obtained with collimating pinholes [60]. But one of the main benefits associated with the use of coherent X-ray beams comes with the ability to measure fluctuations of the scattered intensity. The technique, x-ray intensity fluctuation spectroscopy (XIFS) is an ideal way to perform direct measurements of the dynamics of fluctuations in the system under study at nanometer length scales, provided that the scattered intensity is sufficient for the characteristic time scales involved. In the past few years, XIFS has been demonstrated in studies of equilibrium dynamics such as diffusion of solid latex spheres in glycerol or fluctuations near a critical point in a metallic alloy [7, 41].

Extending XIFS to study non-equilibrium systems is under way. The development of long range order out of a disordered system is a well known and well studied class of non-equilibrium phenomena. In the late stages of such a process, the transition is well described as a collection or ordered domains whose growth are driven by boundary energy reduction. Experiments and theories on these systems have led to the concept of dynamic scaling. The structure is typically well described by one length scale (for example an average domain size) and looks invariant in time when the system is scaled by this characteristic length. The time dependence that enters only through the characteristic length, $R(t)$

can typically be described in terms of a growth exponent n, such as $R(t) \propto t^n$. This scaling hypothesis has been found to correctly describe the time evolution of a large class of systems and to be independent of many microscopic details of the system (including the spatial dimensionality). For example, for first order phase transitions with a non-conserved order parameter, often called model A [29], the growth exponent is found to be $n = 1/2$ while $n = 1/3$ in systems described by a conserved order parameter, also called model B.

XIFS gives the possibility of studying fluctuations around this average behavior by measuring and analyzing the fluctuations in the scattered intensity. One of the main difficulties associated with XIFS studies in non-equilibrium systems is associated with the fact that the averaged scattered intensity, which measures the average structure factor, is not constant. This situation is shown in Fig. 4.1. The recorded, coherent scattered intensity and a calculated average (incoherent) intensity are shown at three different times during an order-disorder phase transition in Cu_3Au (which will be described in detail in the following section).

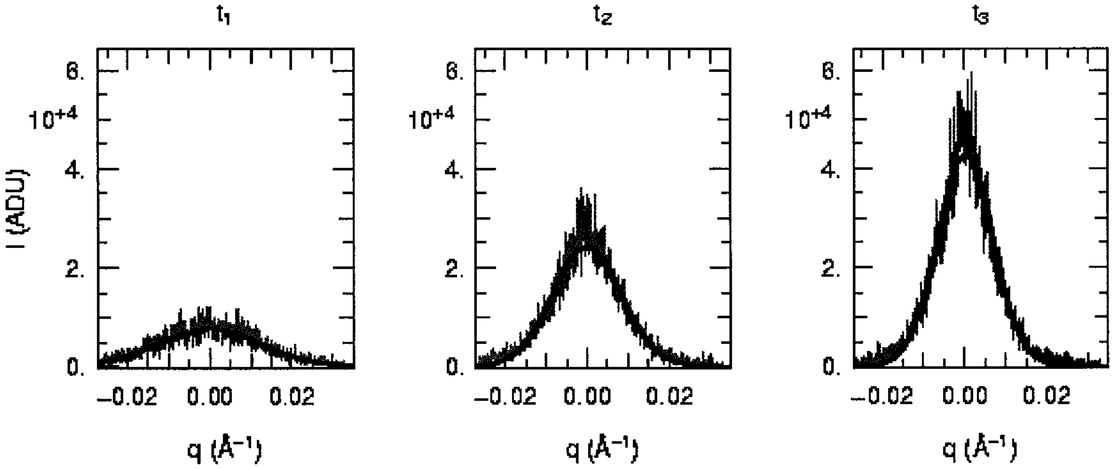

Fig. 4.1 The coherent X-ray scattering pattern measures the time evolution of the exact structure factor. For comparison, an averaged structure factor, which is what an incoherent X-ray beam would measure, is shown as well.

The use of two-time correlation functions of the intensity fluctuations, as proposed in [9, 10] has proven to be useful in studies of phase separation experiments(model B) [44, 38]. This thesis presents the first measurements of two-time correlation functions in systems undergoing first order phase transition with non-conserved order parameter (model A).

4.1.1 Order-disorder phase transitions in Cu_3Au

The order-disorder phase transition in Cu_3Au has been widely studied and is a classic case study for first order phase transitions with non conserved order-parameter [64, 40, 49, 32, 33, 36, 11, 17, 30, 50, 54]. At high temperatures the alloy has a fcc lattice with each site randomly occupied by either a Cu atom or an Au atom. The probabilities of finding a particular type of atom at a given site are given by the stoichiometry: 0.75 Cu and 0.25 Au. Below a critical ordering temperature ($\simeq 383°C$), the system develops long-range order ($L1_2$ structure). The lattice has cubic symmetry and in the four atom basis, the Au atom tends to occupy a specific site, say the corner, while the Cu atoms will be at the three other sites sites (Fig. 4.2).

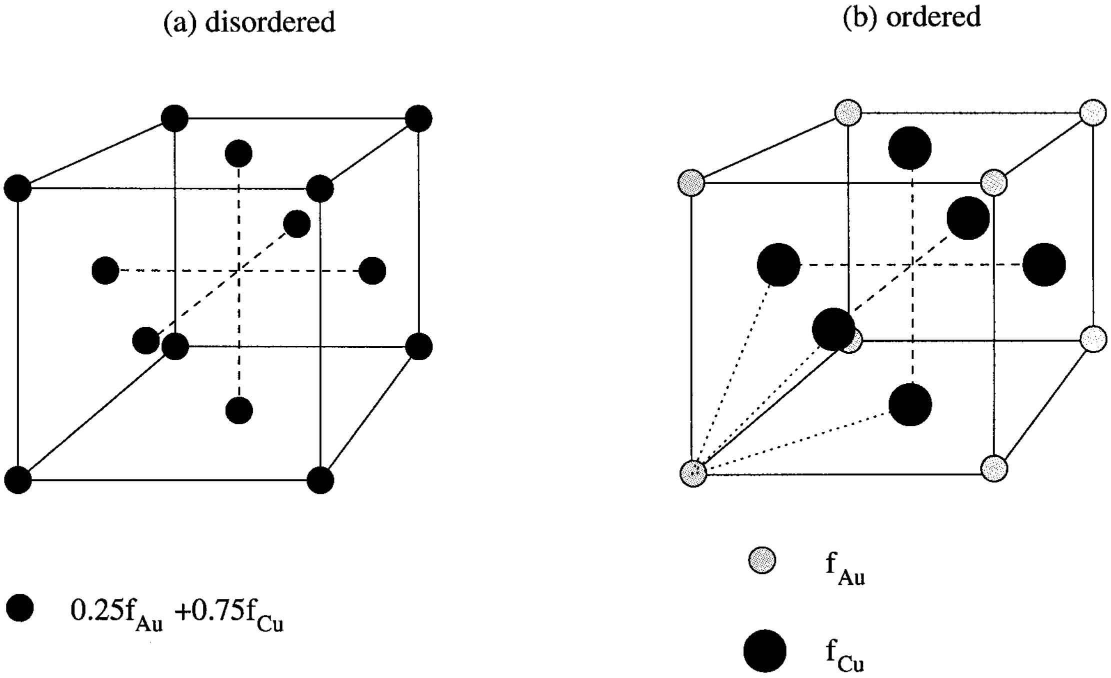

Fig. 4.2 Crystal structure of Cu_3Au. In the disordered phase each site of the fcc lattice can be randomly occupied by either a Cu or an Au atom. In the ordered state, the system develops long-range order. The lattice becomes cubic, and in the four-atom basis (shown by the dotted lines), the Au atoms tend to occupy the "corners", while the Cu atoms will place themselves at the face centers.

However, since the "corner" can be chosen at any of the 4 different sites of the 4 atom basis, the ground state is four-fold degenerate. Different regions in the material can order in any of the four possible orientations of the ordered state and this leads to the appearance of anti-phase domain walls. Two types of domain walls separate regions of ordered-phase material in each of the four possible ground states. For example, a type-I wall perpendicular to the $\mathbf{a_1}$ axis, is created by displacing all the atoms left of the plane by a vector $\frac{\mathbf{a_2}+\mathbf{a_3}}{2}$, while type-II domain walls can be obtained by displacing the same atoms by $\frac{\mathbf{a_1}+\mathbf{a_3}}{2}$ or $\frac{\mathbf{a_1}+\mathbf{a_3}}{2}$ [64, 33]. The two possible types of domain walls (perpendicular to $\mathbf{a_1}$) are shown in Fig. 4.3. The four possible ground states can be distinguished by the position of the Au atom in the 4-site basis. Cyclic permutations of the translation vectors given above will describe the type-I and type-II domain walls perpendicular to $\mathbf{a_2}$ and $\mathbf{a_3}$ respectively.

An important difference between the two types of domain walls is the fact that type-I walls conserve the nearest-neighbor configuration and the local stoichiometry while type-II walls will affect both. Type-II domain walls therefore have a higher surface energy.

A model Hamiltonian describing the ordered and disordered states in Cu_3Au was proposed by Lai [36]. In order to describe the fourfold degenerate ground state and the disordered state, a 3-component order parameter (ψ_1, ψ_2, ψ_3) is defined by linear combination of the occupation numbers s_1, s_2, s_3, s_4. The lattice is described as four cubic sub-lattices corresponding to each of the four sites in the basis and for each site of the main lattice the occupation numbers take a value of -1 at the "sub-sites" occupied by Au atoms and +1 at the "sub-sites" occupied by Cu atoms. If the sample is disordered at that particular location, the occupation numbers are 3*(+1)+1*(-1)=2. The occupation numbers and the corresponding components of the order parameter: ψ_1, ψ_2, ψ_3 can be seen in Table 4.1. The fourth component ψ of the order parameter is proportional to $(s_1+s_2+s_3+s_4)/2$ and reflects only the stoichiometry of the sample at the particular location.

	(s_1, s_2, s_3, s_4)	$(\psi_1, \psi_2, \psi_3, \psi)$
I	(-1, 1, 1, 1)	(-1, -1, -1, 0)ψ_0
II	(1, -1, 1, 1)	(1, 1, -1, 0)ψ_0
III	(1, 1, -1, 1)	(1, -1, 1, 0)ψ_0
IV	(1, 1, 1, -1)	(-1, 1, 1, 0)ψ_0

Table 4.1 The four component order-parameter describing the ordered state in Cu_3Au is defined using the "occupation numbers" s_1, s_2, s_3, s_4.

With the four-component order parameter introduced above, the full Hamiltonian proposed by Lai has the general form of any "ψ^2, ψ^4" Hamiltonian describing a system with a

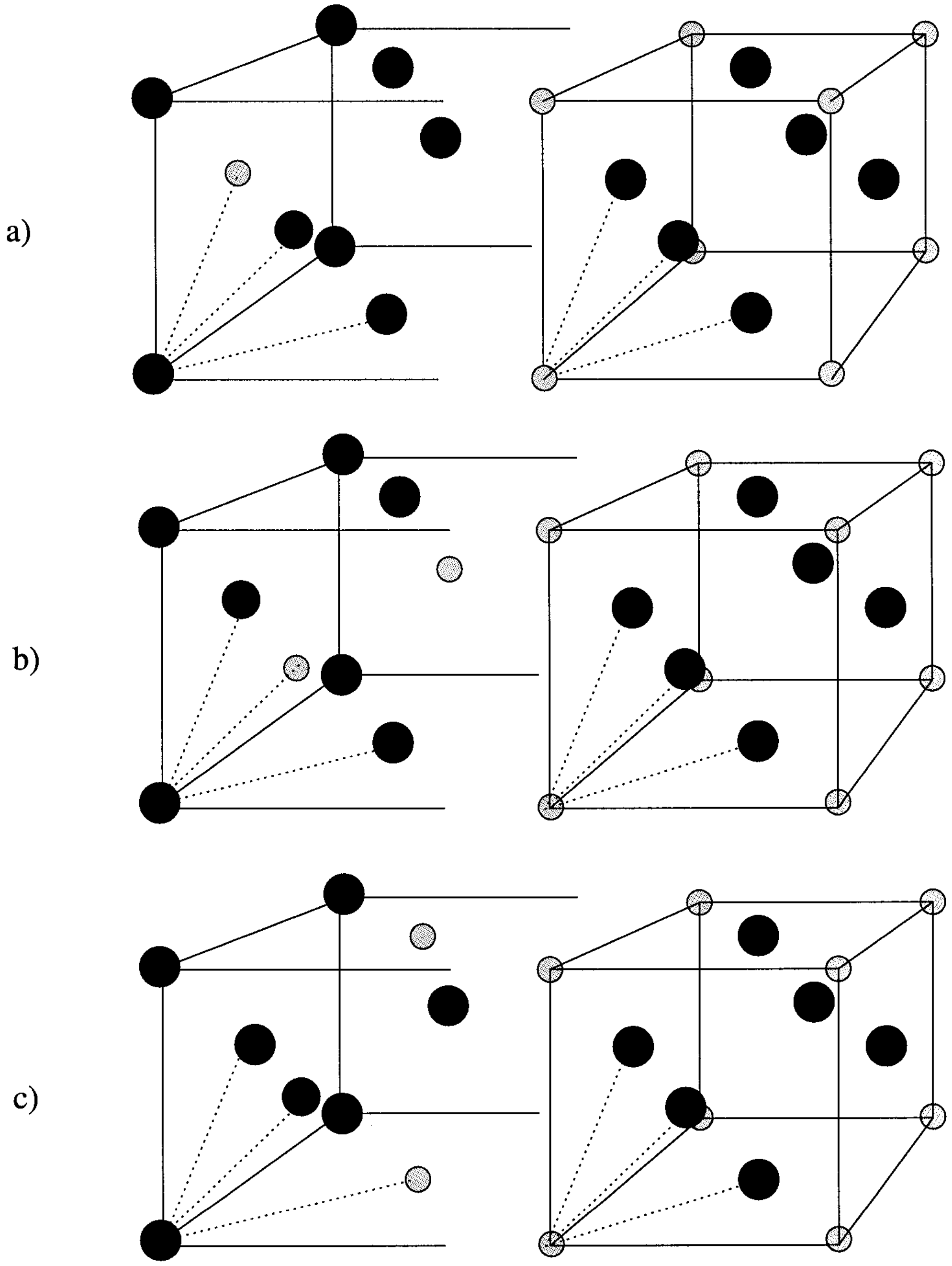

Fig. 4.3 Antiphase domain walls in Cu_3Au: type-I (a) and type-II (b). The Au atom can occupy any of the 4 sites in the basis (shown by the dotted lines) and this leads to a fourfold degeneracy of the ground state (ordered state). The antiphase domain walls are formed when regions in different ordered states come in contact.

metastable (disordered) and a stable (ordered) state, but takes into account the two types of antiphase domain walls and the anisotropy associated with the fact that the two types of domain walls have different energies:

$$\begin{array}{c} H = \int d^d r \tfrac{c_1}{2} \left[\sum (\nabla \psi_\beta)^2 + a \sum (\nabla_\beta \psi_\beta)^2\right] + \tfrac{r}{2} \sum \psi_\beta^2 + w \psi_1 \psi_2 \psi_3 \\ + \tfrac{v}{4} \sum \psi_\beta^4 + \tfrac{u}{4} \left[\sum \psi_\beta^2\right]^2 + \tfrac{r'}{2} \psi^2 + \tfrac{c_1'}{2} (\nabla \psi)^2 \end{array} . \tag{4.1}$$

The index β runs from 1 to 3. The contribution of extra energy cost associated with the domain walls is expressed in terms of the isotropic gradient

$$\frac{c_1}{2} \sum (\nabla \psi_\beta)^2 + \frac{c_1'}{2} (\nabla \psi)^2 , \tag{4.2}$$

while the extra contribution from the type-II domain walls is described as an extra, anisotropic gradient term

$$a \frac{c_1}{2} \sum (\nabla_\beta \psi_\beta)^2 , \tag{4.3}$$

which vanishes for type-I domain walls.

The other terms in the Hamiltonian describe particular features of this system: (i) the v term adds the cubic symmetry of the lattice; (ii) the w term distinguishes between Cu_3Au and $CuAu_3$; (iii) the r term provides the "thermodynamic force" (if negative) for the transition from the disordered state characterized by $\psi_1 = \psi_2 = \psi_3 = 0$.

For a full description of the Hamiltonian for Cu_3Au, the reader should consult Lai's paper [36].

The Lai Hamiltonian (Eq. 4.1) was used to perform Monte-Carlo (MC) simulations of the ordering process. With the assumption that each unit cell is stoichiometric and can be either in the disordered state or in one of the four possible ordered states, the non-trivial (or non-constant) part of the Hamiltonian becomes more simple, and was used to do full, 3D MC simulations.

A typical result of the MC simulations for the ordering process is shown in Fig. 4.4. The disordered phase is represented in black in the order-parameter plots while the four different ground states of the ordered state are represented by the different colors (left column). The corresponding energy is shown in the right column. The process consists of at least two different stages:
(i) Nucleation and growth.

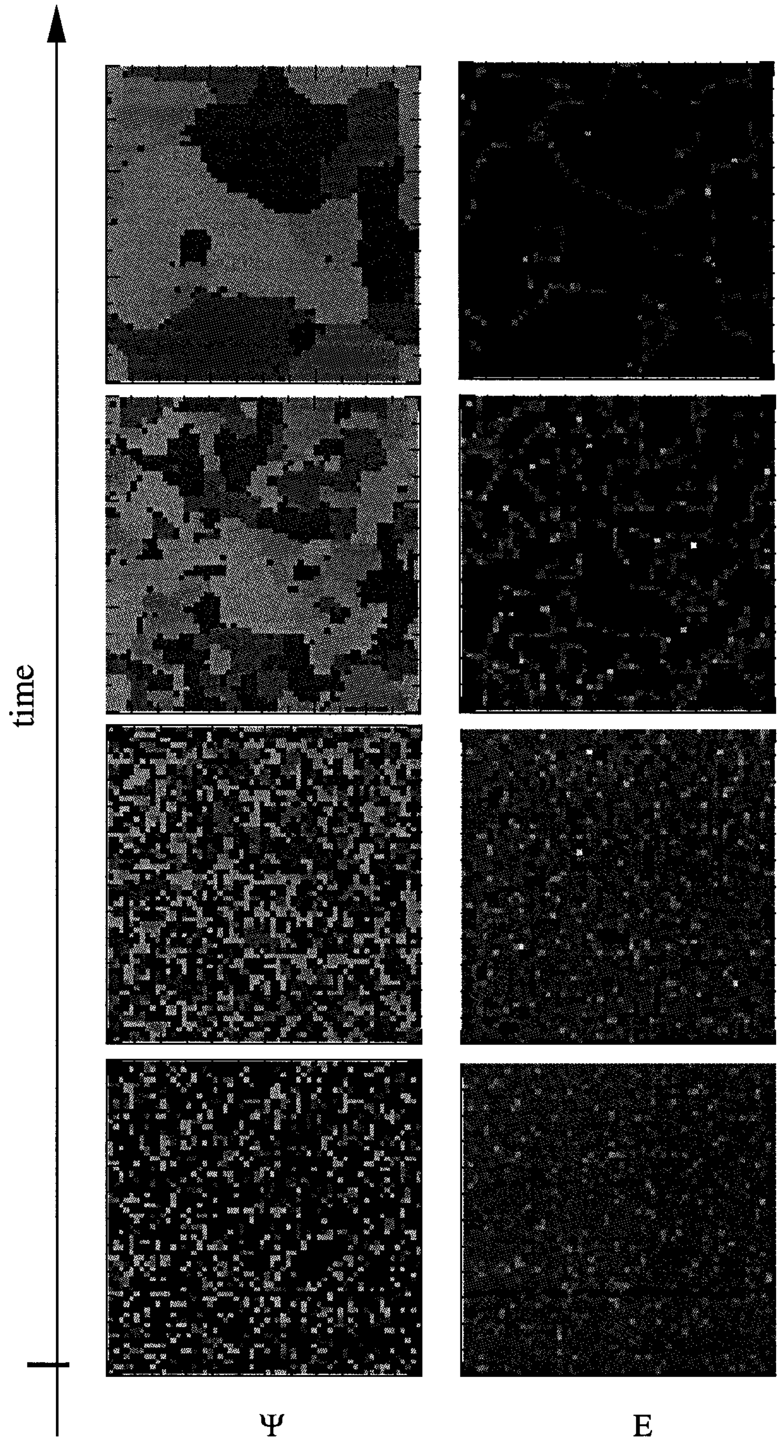

Fig. 4.4 Monte-Carlo simulations of the ordering process in Cu_3Au. The order parameter, with black representing the disordered phase and the four different colors representing the different ground states of the ordered state is shown in the left column. The plots in the right column show the corresponding energy.

Small nuclei of ordered material appear in any of the four allowable ground states by thermal induced transitions from the metastable disordered phase. This process is driven by the reduction of the bulk energy, the ordered state being the more favorable one.

(ii) Coarsening.

After the initial (fast) nucleation and growth stage, domains in different ordered states meet and form antiphase domain walls. The evolution is driven from this point mainly by the reduction of the energy of the domain walls.

4.1.2 Scattering from Cu_3Au

The authors in [40] derived an expression for the diffuse scattering from Cu_3Au valid throughout k space by using a three-dimensional Hendricks-Teller (HT) approach. By assuming that each unit cell is stoichiometric, that the probability of finding a type-I domain wall between a given pair of adjacent cells is γ, and that the probability of finding a type-II domain wall between a given pair of adjacent cells is 2η, the scattered intensity is given by

$$I(\mathbf{q}) = 2\left(f_{Au} - f_{Cu}\right)^2 \sum_{i \neq j \neq k = 1}^{3} \Gamma_{i1}\Gamma_{j1}\Gamma_{i2}\left[1 + cos\pi q_i \left(cos\pi q_j - 2cos\pi q_l\right)\right]. \tag{4.4}$$

Here $\Gamma_{im} \equiv \left(1 - p_m^2\right) / \left(1 + p_m^2 - 2p_m cos2\pi q_l\right)$, with $p_1 \equiv 1 - 2\eta - 2\gamma$, $p_2 = 1 - 4\eta$, f_{Au} and f_{Cu} are the atomic form factors of Au and Cu atoms and q_i are the Cartesian components of the normalized scattering vector $\left(\frac{a}{2\pi}\right)\mathbf{q}$.

The reciprocal space structure of Cu_3Au is shown in Fig. 4.5. The black dots mark the so-called fundamental reflections which are associated with the fcc structure and appear both in the ordered and the disordered phases. In addition, a set of additional Bragg peaks appear only in the scattering patterns from ordered materials. These are called the superlattice peaks. The existence of the rather complicated domain structure in ordered Cu_3Au, causes the superlattice scattering peaks to be anisotropic in reciprocal space. The peaks are disk-shaped with the thickness determined by the density of type-II walls and the radius determined mainly by the density of type-I walls with a smaller influence from the type-II domain walls [40].

In the experiments that are described in more details in the following section, the detector measures, to a first approximation, a section through the axis of symmetry of

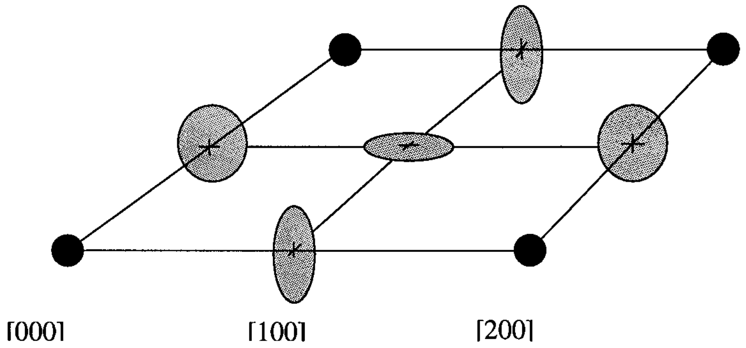

Fig. 4.5 Shape of the diffraction peaks from Cu_3Au. The superlattice peaks are disk-shaped. To a first approximation, the radius of the disk is determined by the density of type-I domain walls and the thickness is determined by the density of type-II domain walls.

the [100] superlattice peak. In fact, because any area detector provides a "2θ" scan, this section makes a small angle ($\sim 11.7°$) with the [100] axis. More details about the detector geometry are given in the following section and in Appendix B.

For the moment, it is useful to understand that, because the way it is mounted, a horizontal row of pixels through the CCD images (see Fig. 4.6) provides to a first approximation radial scans along the [100] axis, while a vertical row of pixels on the detector provides a transverse scan along a direction perpendicular to [100].

4.2 Experimental details

The experiments were performed using partially coherent X-rays at beamline 8-ID of the Advanced Photon Source. A thin diamond crystal monochromator was used to produce 7.66 keV X-rays having a relative bandwidth $\Delta\lambda/\lambda = 6.2\times10^{-5}$ and a flux of $\sim 5\times10^{12}$ photons per second for a storage ring current of 100 mA. A transversely coherent beam was produced using slits with highly polished edges set to a horizontal aperture of 5 μm and a vertical aperture of 10 μm. The scattered X-rays were recorded by an area direct illumination, "deep-depletion" charge-coupled device (CCD) with 22 μm square pixels located 1.20 m from the sample (see ref. [39] for more details about the CCD detector). The **q**-space resolution in coherent diffraction experiment is limited by either the pixel size or the speckle size (Eq. 2.27), whichever is larger. In order to improve statistics, the detector distance and the slit sizes were adjusted to provide a good factor of coherence and to give a speckle

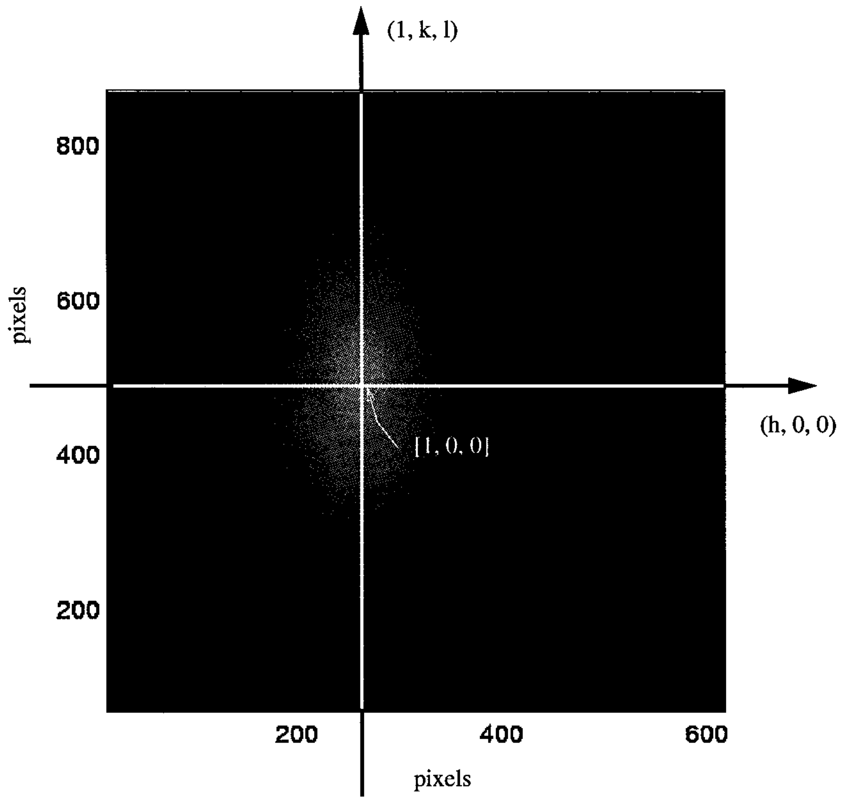

Fig. 4.6 The CCD detector measures a section through the [100] superlattice Bragg reflection.

size similar to the pixel size. As a consequence, the **q**-space resolution in our experiments is determined by the pixels size and is better than $\sim 10^{-4}$ Å^{-1} (see Appendix B for details). The exposure time was adjusted to maximize the measured signal while preventing the detector from getting saturated.

The relationships dependence of the longitudinal and transverse coherence length and pixels size on the scattering geometry and the properties of the X-ray source have been explained in Section 2.3. The experiments described here have been performed on the 8-ID-E beamline (commissioned to the McGill-MIT-IBM collaborative access team) of the Advanced Photon Source. The source to sample distance is 55m and the source size is 250 μm (horiz.) x 15 μm (vertical) (FWHM). From here, a transverse coherence length of $\sim$20μm (FWHM) is expected in the vertical direction and $\sim$4μm (FWHM) in the horizontal direction. The longitudinal coherence is determined by the relative bandwidth (Eq. 2.25), $\Lambda \simeq 1.30\mu m$. In the symmetric reflection geometry, the largest path-length difference is $2L_z sin\theta$, where L_z is the penetration depth normal to the surface. The adsorption length for 7.66keV photons in ordered Cu_3Au is $L \simeq 6.6\mu m$. From here, the penetration depth can be estimated by $L_z = Lsin\theta \simeq 1.32\mu m$, which determines the largest path-length difference: $\delta \sim 2Lsin^2\theta \simeq 0.53\mu m$, which is below the longitudinal coherence length.

The sample furnace consists of a pyrollitic-graphite heater mounted on a water-cooled Cu heat sink. This arrangement gives sufficient cooling power to quench the sample, a penny-sized Cu_3Au single crystal, at a rate of about 1°C/s. The temperature probe is a thermocouple fixed on the surface of the sample. The sample holder, heater and cooling post are mounted in a vacuum chamber. Fast temperature quenches without any significant temperature undershooting were performed using a temperature controller that combines proportional-integral-derivative feedback with thermal modeling and finite difference thermal calculations (feedforward) and Kalman filtering of the temperature readings in order to reduce the noise. The sample furnace geometry and the Kalman-Predictive-Proportional-Integral-Derivative (KPPID) control algorithm were presented in detail in Chapter 3 of this thesis.

In the XIFS experiments described in this chapter, the growth of the [100] superlattice peak was measured during the ordering process, after quenches from the high-temperature disordered phase to a temperature below the critical temperature. This peak is showed in Fig. 4.8 at various moments during the ordering process. As it was pointed out in the previous section, quasi-transverse scans ([100] direction) through the disk-shaped reflexion

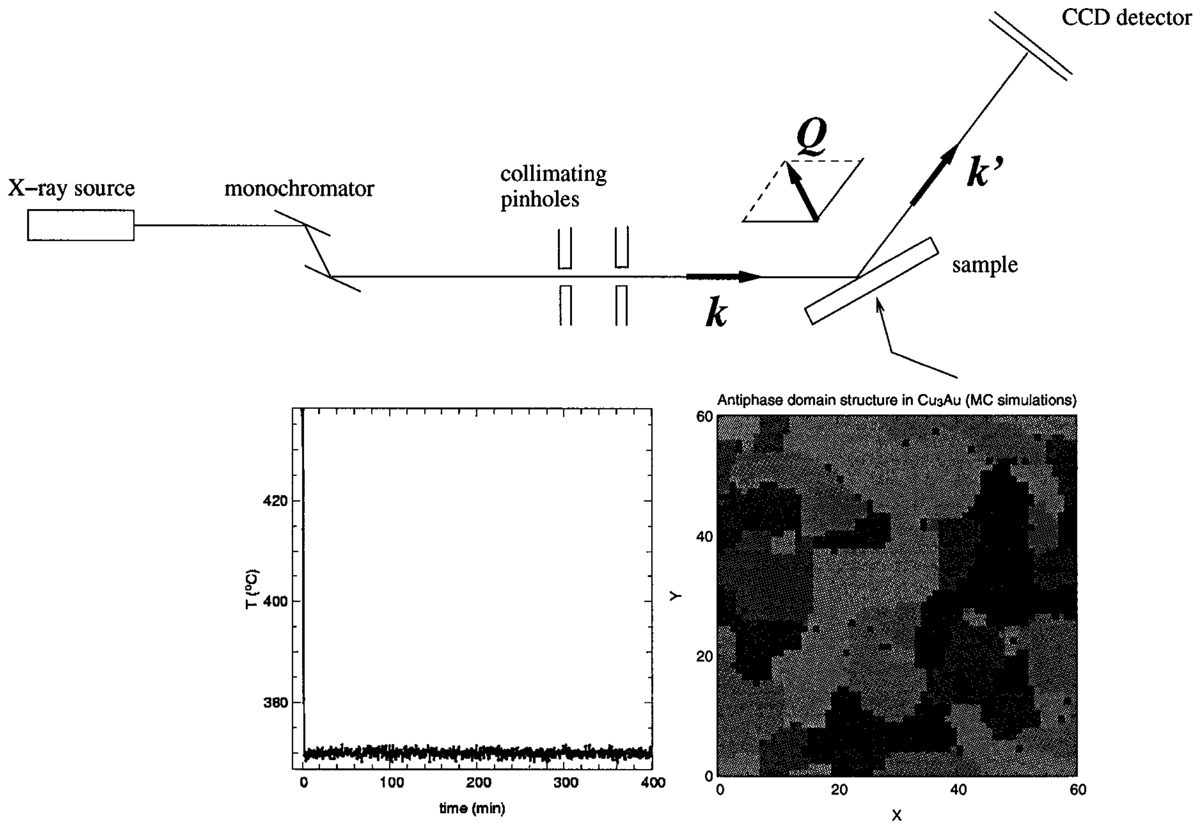

Fig. 4.7 A schematic of the coherent X-ray spectrometer and the XIFS experiments on the ordering process in Cu_3Au. Coherent X-ray diffraction patterns are recorded by a CCD area detector while the sample undergoes an ordering process triggered by a sudden temperature quench (shown in the inset).

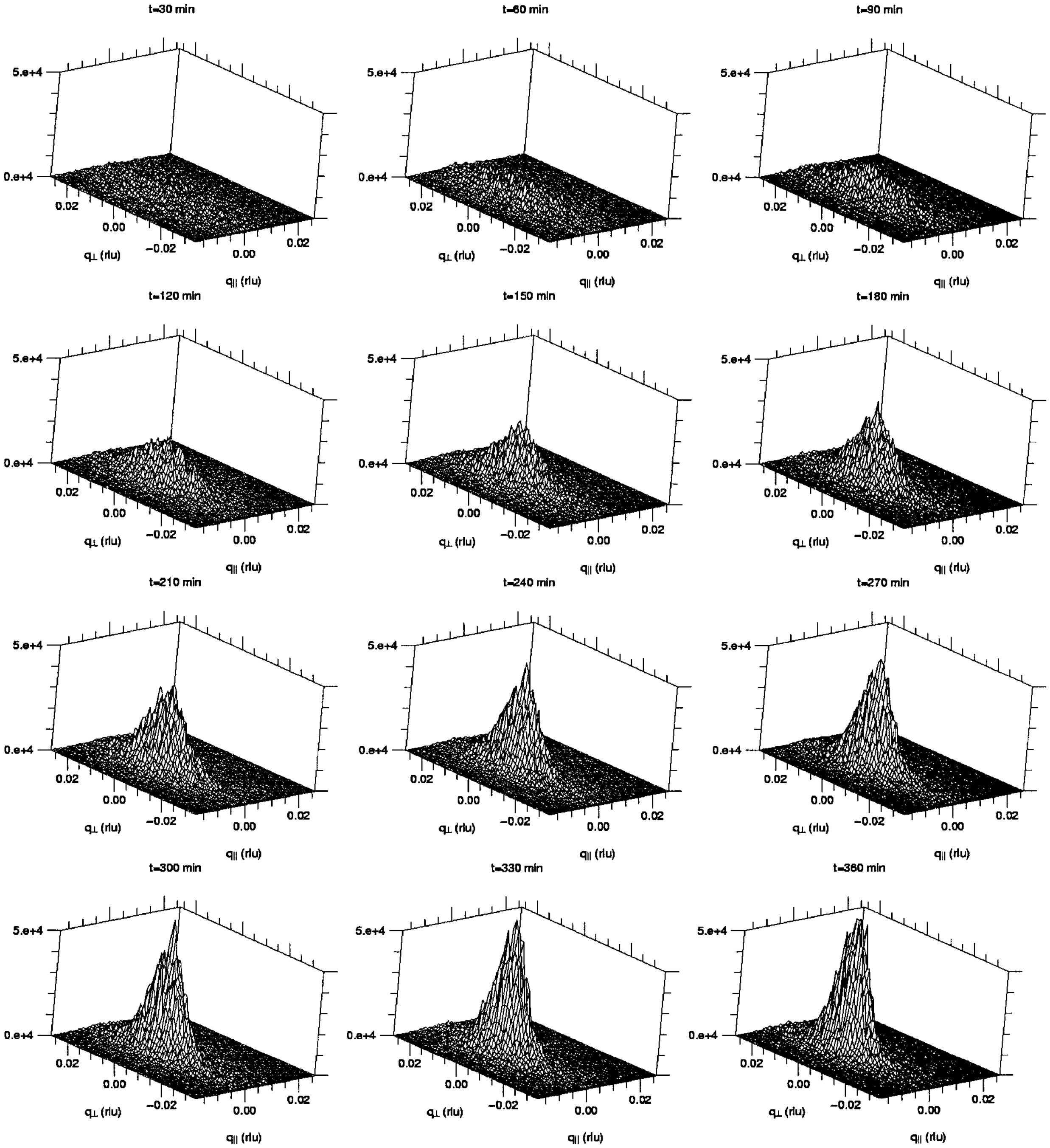

Fig. 4.8 Growth of the [100] peak in Cu$_3$Au after a quench from the high-temperature disordered phase to a temperature below the critical ordering temperature.

are obtained by taking "horizontal" sections through the CCD detector while a vertical section through the CCD detector will provide a quasi-radial scan. The exact variation of the reciprocal-space components of the scattering vector q_1, q_2, q_3 along the horizontal and the vertical directions on the area detector as well as details about the detection geometry and the "pixels-to-$\mathbf{q}$ mapping" can be found Appendix B.

Transverse scans through the Bragg peak mainly measure the dynamics of type-II domain walls. However, since the q_2 component of the scattering vector also changes (albeit by a smaller fraction) during transverse scans, they will also be sensitive to type-I wall dynamics simply because we measure a projection of a radial scan as well. A radial scan is, within experimental errors, a purely radial scan, but on the other hand the radial dimension of the peak itself although determined mainly by the concentration of type-I domain walls is affected by the type-II walls as well as it is suggested by calculations using Eq. 4.4. One can conclude thus that the information obtained from X-ray scattering (for both radial and transverse scans), couples to a certain degree the dynamics of type-I and type-II domain walls. However as it can be estimated by "playing" with Eq. 4.4, this "convolution" is more significant for transverse scans. The influence of type-I domain walls on the radial distribution of the scattered intensity is less important than the influence of type-II walls on the transverse distribution of the scattered intensity and is completely due to the impossibility of obtaining a purely radial scan by choosing appropriate pixels on the CCD detector.

In a typical experiment, the sample was held at ~425°C and rapidly quenched (within 1 min.) to a temperature below T_c where it was held for a few hours. During this process, scattering patterns from the [100] superlattice peak were recorded every minute and sometimes every 20s. The time-dependence of the scattering data can be seen in Fig. 4.9. Radial and transverse scans through the Bragg peak as well as the sample temperature and the average scattered intensity over a small area around the peak centre are plotted against time.

Each CCD frame is a section through the Bragg peak (Fig. 4.10). The "speckled" aspect of the scattered intensity is due to coherence of the X-ray beam. Standard, "one-time" quantities such as an average domain size or an ensemble averaged structure factor can be obtained from the speckled diffraction patterns by some averaging or smoothing process. An estimate of the incoherent scattered intensity is shown on the left side of the CCD frame in Fig. 4.10.

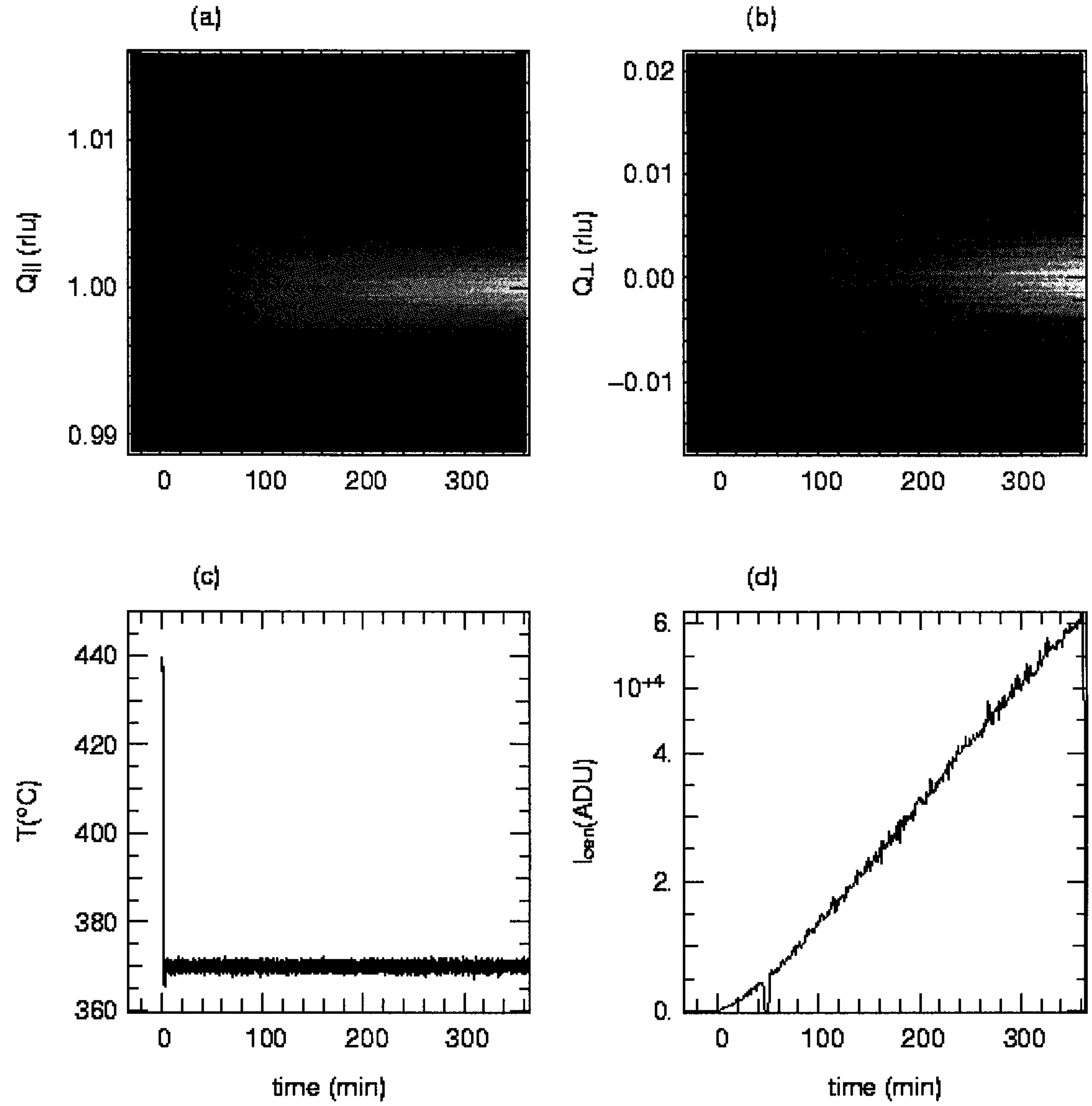

Fig. 4.9 Ordering process in a Cu_3Au single crystal following a temperature quench from ≃ 425°C (disordered phase) to 370°C. Radial scans (a) and transverse scans (b) through the centre of the [100] superlattice peak; (c) temperature quench; (d) scattered intensity averaged over a small area around the peak centre.

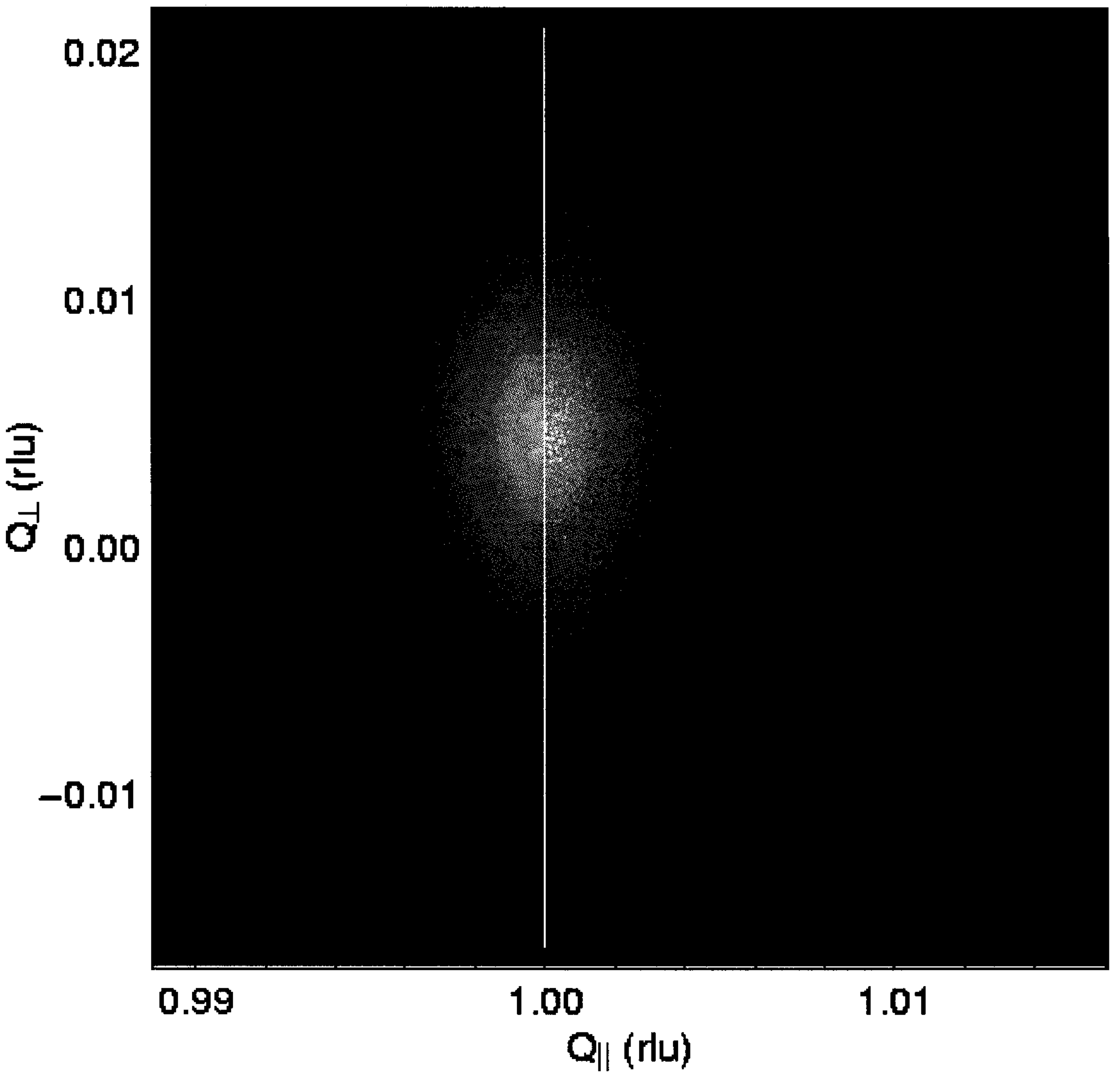

Fig. 4.10 One frame recorded by the CCD detector. The actual diffraction image is shown in the right side of the CCD frame. The "speckled" aspect of the Bragg peak is due to the beam coherence. For comparison, a "smoothed" image is shown on the left side of the frame.

4.3 One-time (incoherent) analysis

The X-ray data is first compared with the predictions of dynamic scaling theories (for an extensive review, see Gunton et. al. [29]). Experimental evidence for the scaling behavior in such processes were obtained in previous studies, using "standard" time-resolved (incoherent) X-ray scattering techniques, by Nagler, Shannon and their coworkers [49, 33].

In order to obtain quantities such as average domain sizes or the center of the Bragg peak, which are typically obtained in an incoherent X-ray diffraction experiments, the coherent diffraction patterns were fitted by 2D Gaussian functions (G2D). This fitting procedure provides an estimate for the ensemble averaged structure factor $\langle I(\mathbf{q},t)\rangle$ that would be measured by incoherent X-ray scattering. Although we do not expect the Gaussian profile to describe the "fine details" of the peak shape, we found they provide a more than satisfactory way to parameterize the data and estimate quantities such as the peak height, the peak width and peak centre. More details about the peak shape will follow in Section 4.4.1, where a very accurate estimate of correct shape becomes critical for the calculation of the intensity fluctuations and their autocorrelations.

Transverse and radial scans through the [100] superlattice peak center and the corresponding least-square fits (G2D) are shown in Fig. 4.11. The Cu_3Au sample is undergoing an order-disorder phase transition after temperature quenches from 420°C to 360°C, 370°C and $375°C$.

The amplitude of the scattered intensity should be proportional to the square of the order parameter while the integrated intensity should be proportional to the relative density of ordered material. A plot of the fitted amplitude and the integrated intensity vs time is shown in Fig. 4.12. From simple mean-field theories for an Ising-type model, Monte-Carlo simulations of the ordering process and even experimental data on the early stages of the order-disorder phase transition [40], it may be argued that the integrated intensity should be constant. In other words that means that the relative density of ordered material is constant throughout these experiments. The initial ordering process happens on time scales which are shorter than the time step used here.

In order to calculate the integrated intensity shown in Fig. 4.12, the fitted amplitude is multiplied by the fitted radial width and the fitted transverse width squared. By doing this instead of summing all the counts both the intensity in the tails and the intensity not measured by the CCD detector is accounted for. The small decrease in intensity at large

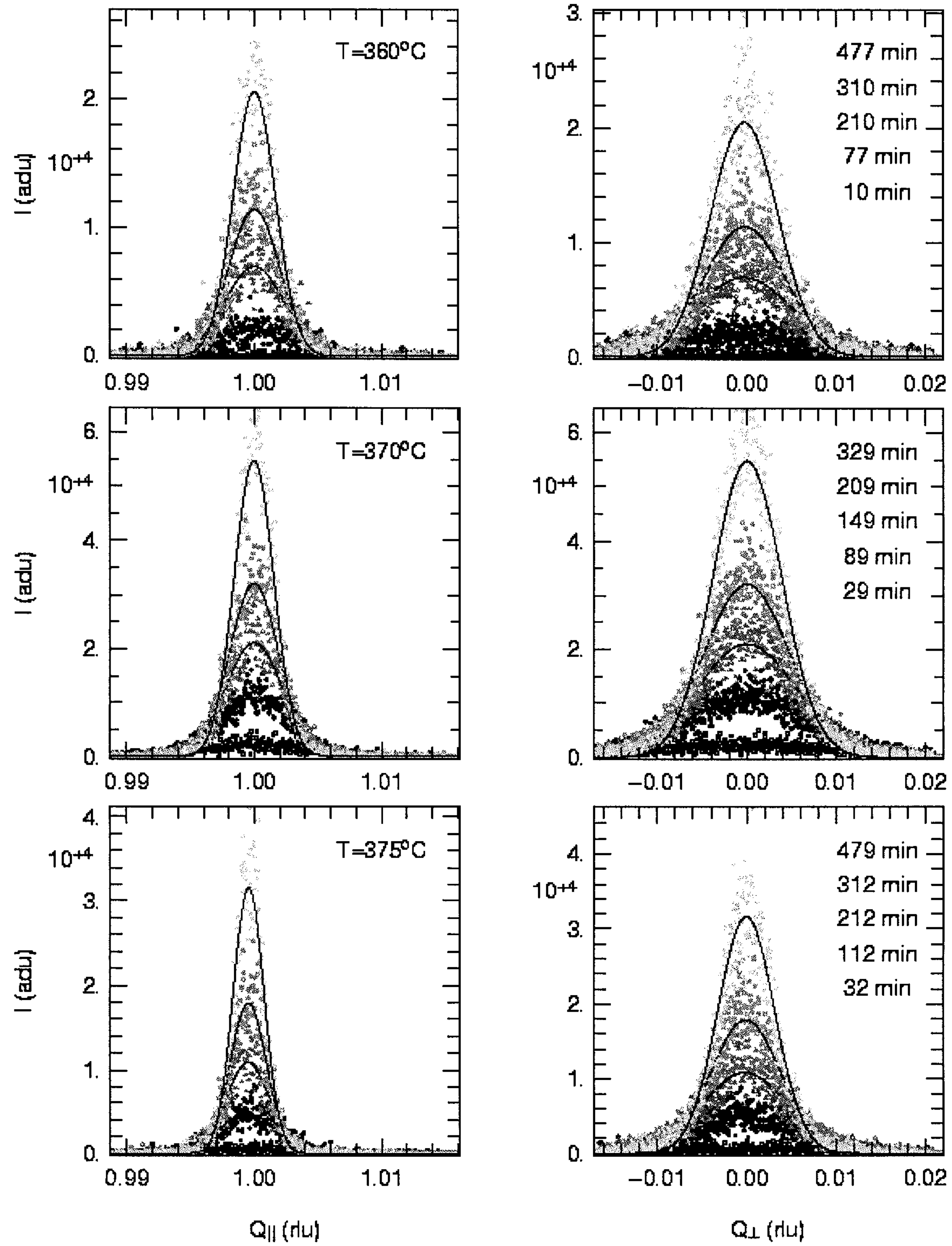

Fig. 4.11 Radial (left column) and transverse (right column) scans through the [100] superlattice peak during the phase ordering process. The data was obtained from the temperature quenches to 360°C (upper row), 370°C (middle row) and 375°C (lower row). The times at which the scattered intensity was plot are also shown for each temperature. The black lines show the fits to the scattered intensity with 2D Gaussian functions.

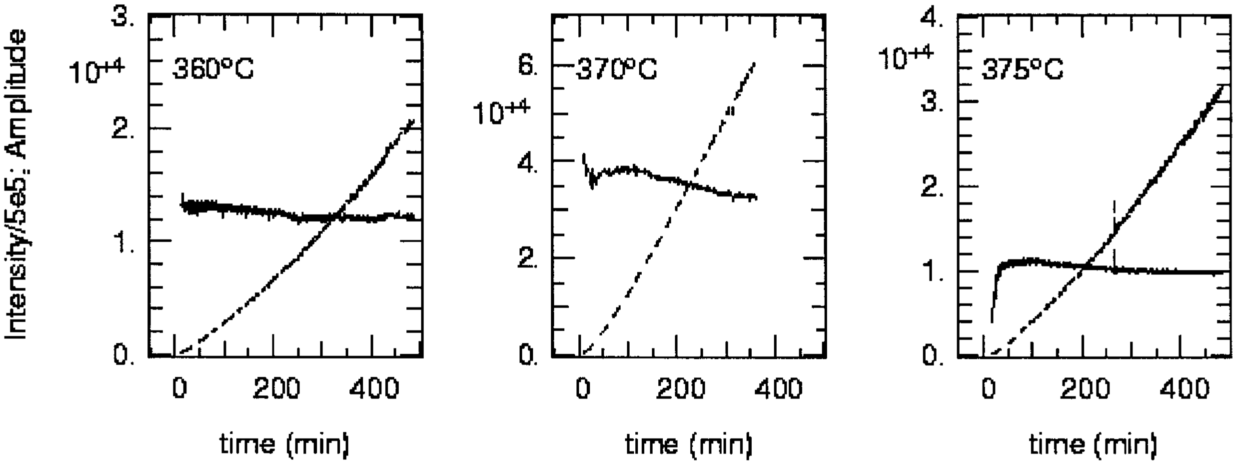

Fig. 4.12 Integrated scattered intensity (continuous line) and fitted amplitude (dotted line) vs time after temperature quenches to 360°C, 370°C and 375°C. The integrated intensity has been divided by 5×10^5 to plot it on the same scale as the amplitude.

times is probably due to the fact that the fits with 2D Gaussian functions do not have the correct tails and some of the intensity is therefore "missed".

Similar results have been obtained by Shannon et. at. [33]. However, since they used a standard point detector to do radial ($\theta - 2\theta$) scans and a linear position sensitive detector to do transverse scans and since their spatial resolution was at least one order of magnitude worse than the resolution obtained with the area CCD detector used in our experiments, their results are a bit more difficult to interpret. The graph in the left panel of Fig. 4.13 (from [33]) shows the integrated intensity and the amplitude obtained from transverse scans at the (010) following a temperature quench to 380°C. In the right panel we show similar results from our scans following a temperature quench to 375°C.

A first difference is that in the experiment reported here we covered a smaller time range. Synchrotron-based experiments have numerous advantages over "standard", laboratory-based studies, but scheduling long experimental runs is sometimes more difficult. The scattered amplitude behaves similarly in both studies. One can argue that in our case (right panel) it doesn't show the "slowing down" tendency that can be observed in Shannon's results, but this small difference can be caused by the temperature difference and one can argue that the same effect would have been observed in our scans, had we had the possibility to continue them for slightly longer times. The more important difference is the integrated intensity. As it was mentioned before, the integrated intensity reported here was

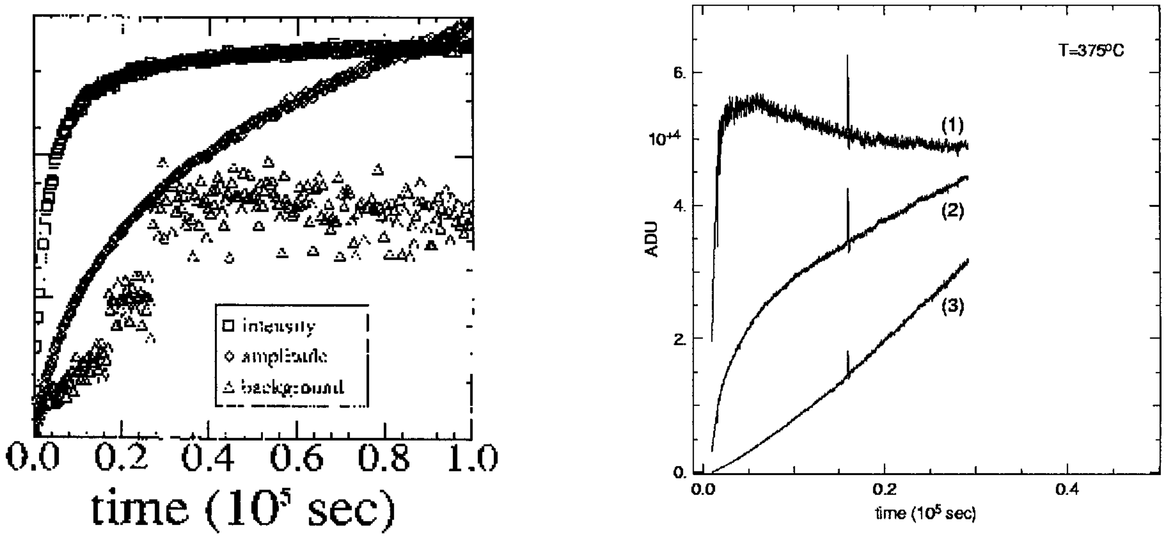

Fig. 4.13 Fitted amplitude and integrated scattered intensity from ref. [33] (left panel) and from our data (right panel). The integrated intensity is calculated as the product between the fitted amplitude, radial width and squared transverse width of the Bragg peak (line (1) in the right panel). The scattered amplitude is shown by the line labeled (3).

calculated as the product of the scattered amplitude, the radial width and the transverse width squared. This was allowed by the CCD area detector and although the radial size of the Bragg peak measured here is expected to be slightly smaller than the actual value because of the subtle deviation of the "radial scans" from the (h00) direction, it should provide an adequate approximation for the total scattered intensity. In order to estimate the same quantity from a linear scan, Shannon et. al. have corrected for resolution effects in one direction, calculated the intensity as the product of the amplitude and the corrected width and assumed that the effective measurement approximately integrates over the other two dimensions. However, one can argue that there is a certain likelihood that some of the scattered intensity is actually "missed" by doing this and their results show that this may indeed be the case. The calculated intensity (left panel, squares) follows a slower increase than expected. In order to get a "feeling" about the effects that some "missed" intensity can have on the integrated intensity plots, the curve labeled (2) in the right panel of Fig. 4.13 shows a calculated intensity for which some of the counts have intentionally been missed. The amplitude was multiplied with the transverse and radial width of the peak. It is easy to imagine that by "tuning" the fraction of counts that are missed, any profile between this and the curve labeled (3), which is the correct intensity, calculated as the product between the amplitude, radial width and transverse width squared, could be obtained and interpreted as the counts obtained from a particular detection method. In conclusion, we argue that by using a high resolution detector, one can calculate an adequate approximation for the total scattered intensity and this can be seen in both Fig. 4.12 and Fig. 4.13.

4.3.1 Dynamic scaling

Scaling describes well the evolution of dynamic systems if there is a single length scale, which contains all the time-dependence. Scaled by that characteristic length, the system looks invariant in time. The characteristic length describing the time evolution of the order-disorder phase transition in Cu_3Au is, of course, the average domain size of ordered domains. In this particular case the existence of two types of domain walls introduce an ambiguity: an average distance between type-I domain walls can be measured by a transverse scan and can be considered a "type-I" average domain size, while a radial scan measure the average distance between type-II domain walls and can also be considered an average domain size (albeit a "type-II" one). Is there a single characteristic length? The answer is yes, in the sense that, at least in the late stages of the ordering process the relative density of the two types of domain walls follows a thermal distribution and is constant in time. In other words, the peak shape doesn't change and the the average domain sizes provided by radial and transverse scans are connected by a constant "anisotropy parameter". This scaling picture is the main result of the time-resolved X-ray diffraction studies on the ordering process in Cu_3Au by Nagler [49] and Shannon [32, 33] and is confirmed by the studies presented in this thesis as well. However, subtle deviations from the scaling behavior can be seen during the early time stages of the ordering process. In order to measure "one-time" (average) quantities, the fits with G2D functions were used as an estimate for the average intensity $\langle I(q,t)\rangle$. The growth of the average domain size is expected to follow a $D \sim t^{1/2}$ law for a model A system, and this is seen in Fig. 4.14. The solid line is a slope 1/2 straight line (log-log plot) and the data (dots) follow well this growth law in the late stages but the early time-deviations are quite important (~30min) at this temperature (360°C).

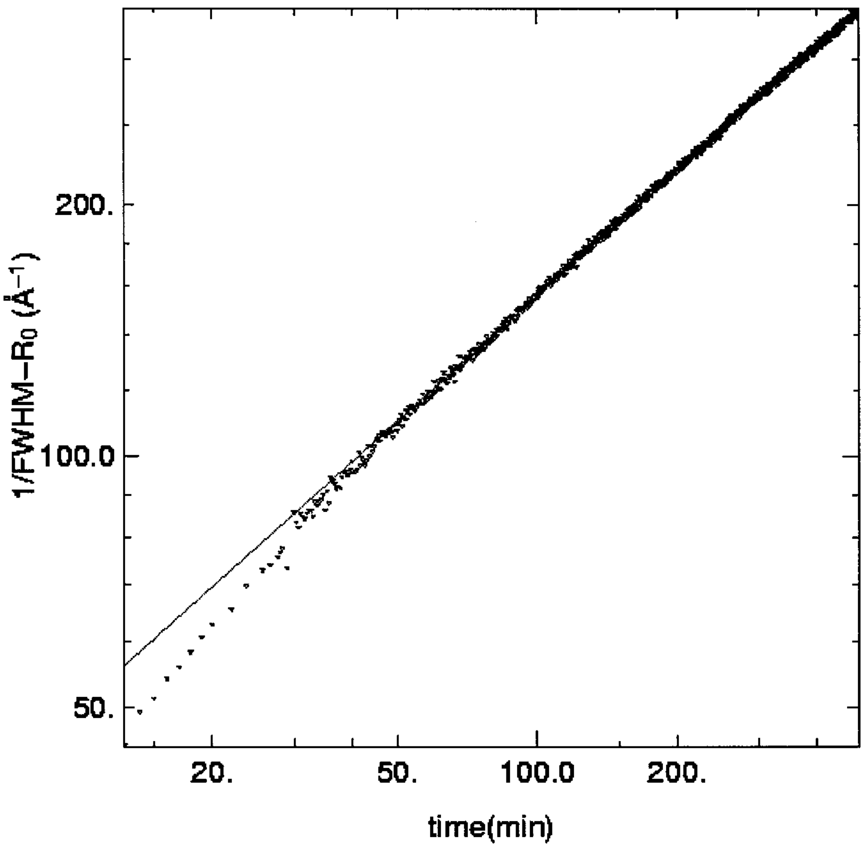

Fig. 4.14 The average domain size, measured as the inverse of the Bragg peak width (FWHM) follows a $\sim t^{1/2}$ scaling law.

To test the power scaling law, the average domain size, obtained from the inverse of the peak width (FWHM) was fit to equation

$$D = R_g t^{1/2} + R_0. \tag{4.5}$$

Here, the parameter $R_g \left[\frac{\mathring{A}}{min^{1/2}}\right]$ is a measure of the speed of growth of the ordered domains and R_0 can be interpreted as a critical droplet size at which the scaling description starts being accurate. Full data, from quenches at 360°C, 370°C and 375°C and for both radial and transverse scans are shown in Fig. 4.15. As it can be seen the process closely follows a $\sim t^{1/2}$ law in all the cases although some early time deviations can be seen for times as long as $\sim$ 30 min, especially at 360°C 375°C.

These results were compared with those reported by Shannon ([33]). The average domain size, calculated as 2π/(peak width - FWHM) obtained from radial scans through the [100] peak following temperature quenches to 360°C and 370°C is shown in Fig. 4.16. The third line shows a the growing law obtained by Shannon et. al. for a quench to 365.8°C. As one can see the matching is nearly perfect.

As a consequence of the $\sim t^{1/2}$ growth law, the structure factor can be collapsed on a stationary shape if the normalized intensity, $\frac{I}{I_{max}}$ is plotted against a rescaled scattering vector (or time) $qt^{1/2}$. This scaling behavior is shown in Fig. 4.17. The scaled intensity is plotted against the rescaled position at five different times after quenches from the disordered phase at 360°C, 370°C and 375°C. The black lines are the rescaled Gaussian fits.

In this form, the rescaled one-time structure factor is not temperature independent. The rescaled intensity plots for three different temperatures are shown in Fig. 4.18.

In order to rescale the structure factor to a temperature independent form, the time required for the average domain size to reach a certain value can be considered as a (temperature-dependent) characteristic time (Fig. 4.19). If the time is measured in units of this characteristic time, the structure factor scales to a temperature independent form, and all the temperature dependence is "buried" in the parameter t_D. The rescaled, temperature-independent structure factor is shown in Fig. 4.20 for both radial and transverse scans.

The temperature dependence of the ordering kinetics is given by the temperature dependence of the diffusion constant and by the thermodynamic force, which in this case is the temperature-dependent free energy difference. The two mechanisms have opposed

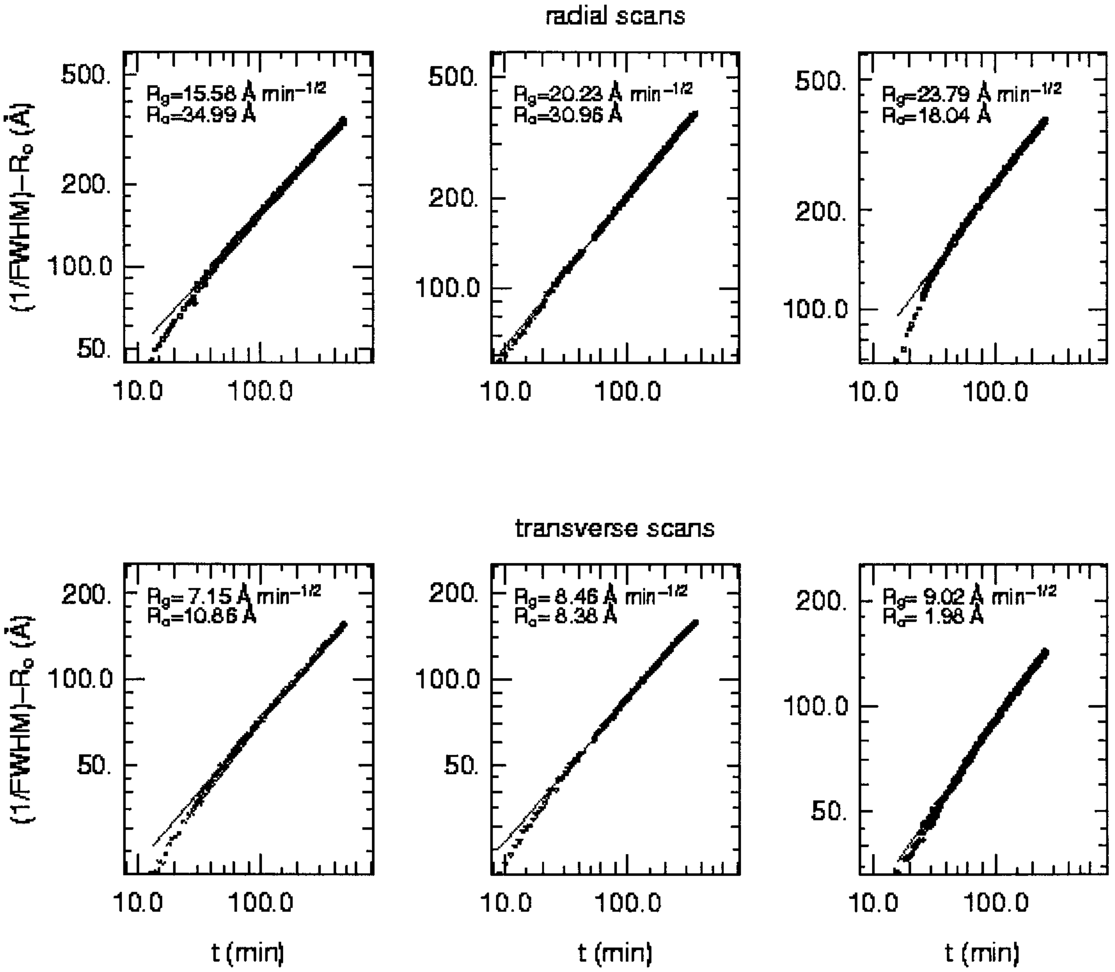

(a) 360°C **(b) 370°C** **(c) 375°C**

Fig. 4.15 The average domain size, which is measured as 1/FWHM of the Bragg peak follows a $\simeq t^{1/2}$ growing law during the coarsening regime. The solid lines show fits to Eq. 4.5. The fitted parameters R_g and R_0 are marked on the graphs.

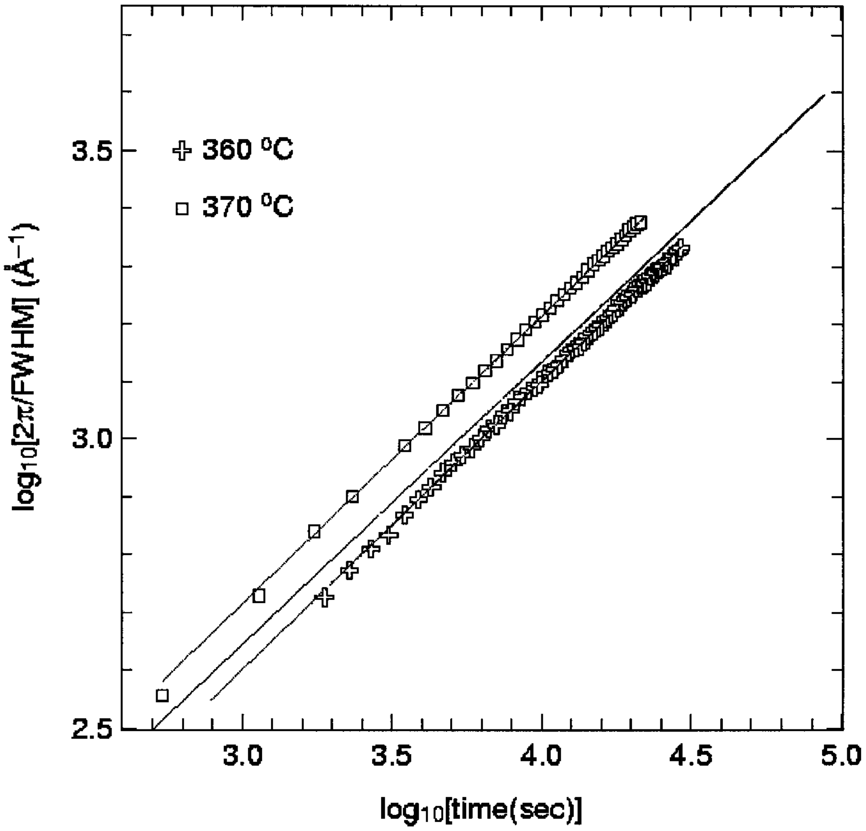

Fig. 4.16 Average domain size, measured as 2π/FWHM of the Bragg peak; (i) results obtained by Shannon et. al. from a temperature quench to 365.8°C (solid line); (ii) our results for temperature quenches to 360°C, 370°C and fits to Eq. 4.5.

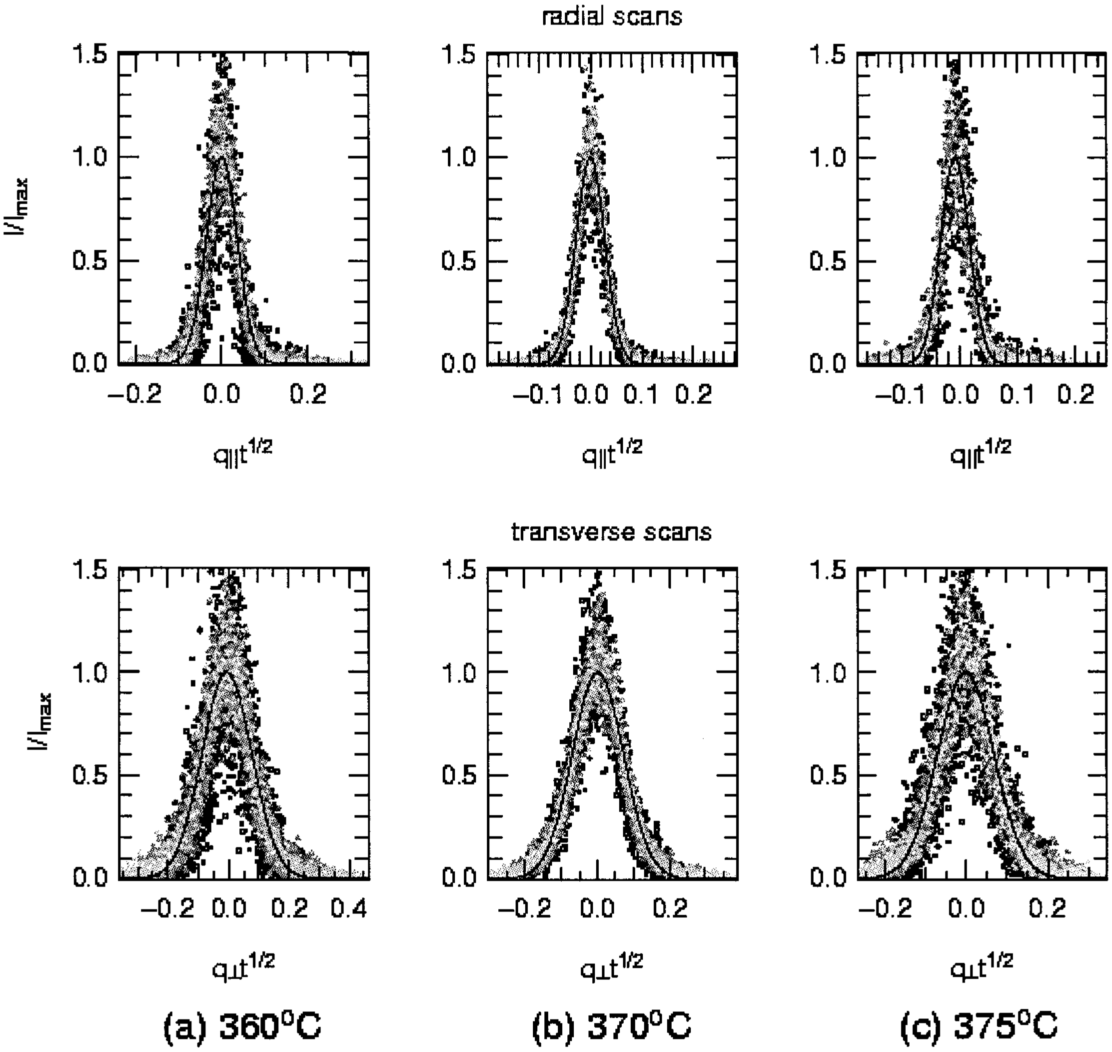

Fig. 4.17 Scaling of the average structure factor. The normalized intensity, I/I_{max} plotted against a rescaled wavevector $q_{||}t^{1/2}$ for a radial scan or $q_{\perp}t^{1/2}$ for a transverse scan follow an universal curve.

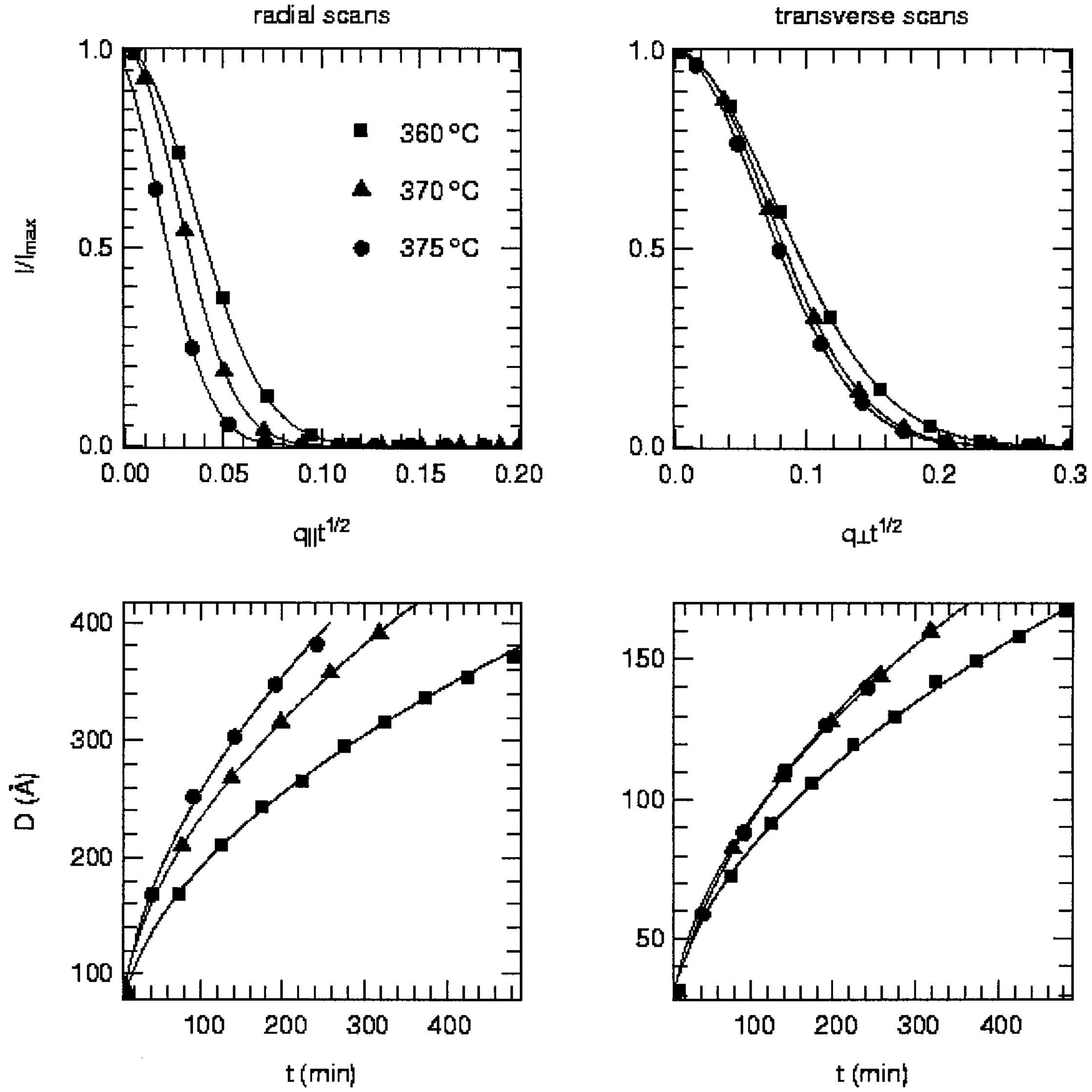

Fig. 4.18 Temperature variation of the rescaled structure factor and of the average domain size.

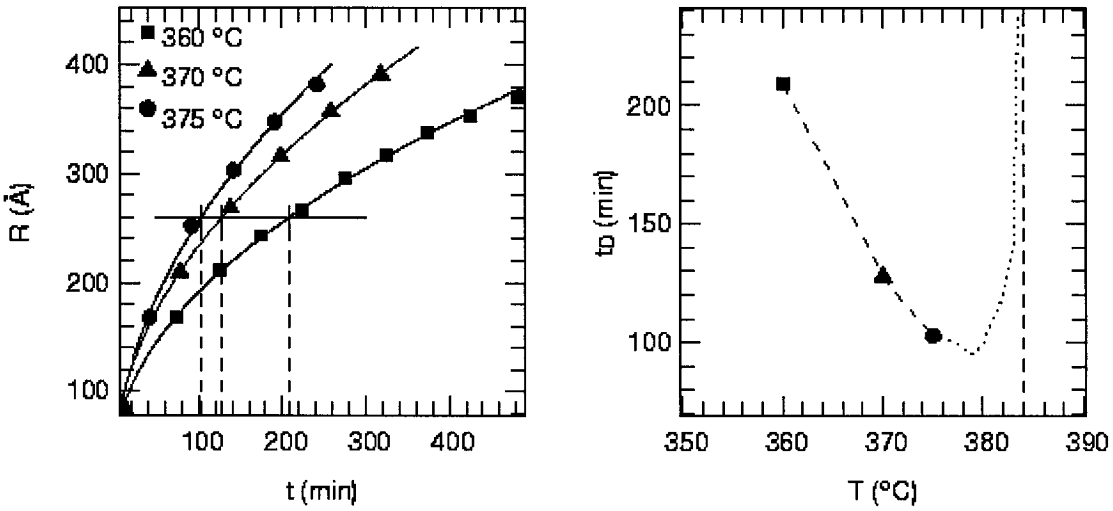

Fig. 4.19 The time required for the average domain size, D to reach a certain value can be considered as a (temperature-dependent) characteristic time for domain growth. Such characteristic times are shown in the right panel. Because the free energy difference between the ordered and the disordered phases vanishes at the critical point, the characteristic times are expected to diverge at the critical temperature.

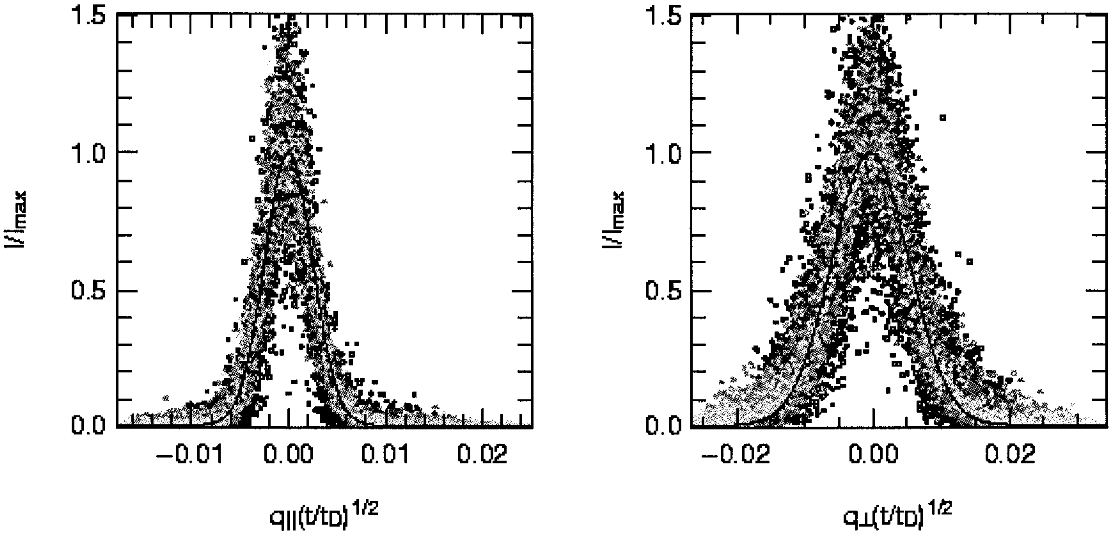

Fig. 4.20 Rescaled structure factor. By measuring the time in units of the characteristic time t_D, the structure factor rescales to a temperature-independent form for both radial and transverse scans.

temperature dependences. A deeper quench (lower final temperature) will increase the thermodynamic force but will also decrease the diffusion constant. The data shown in figures 4.18 and 4.19 suggests that in the 360°C - 375°C temperature range the ordering process is in a diffusion-limited regime. The average domain size grows slower for a "deeper" quench or equivalently, the characteristic time t_D is longer.

Similar information can be obtained from the scattered amplitude, which is proportional to the square of the order parameter. The fitted amplitude was plot in Fig. 4.21 as a function of time, for the three quenches to 360°C, 370°C and 375°C. The temperature dependence is similar to that of the kinetics of domain growth shown in Fig. 4.18.

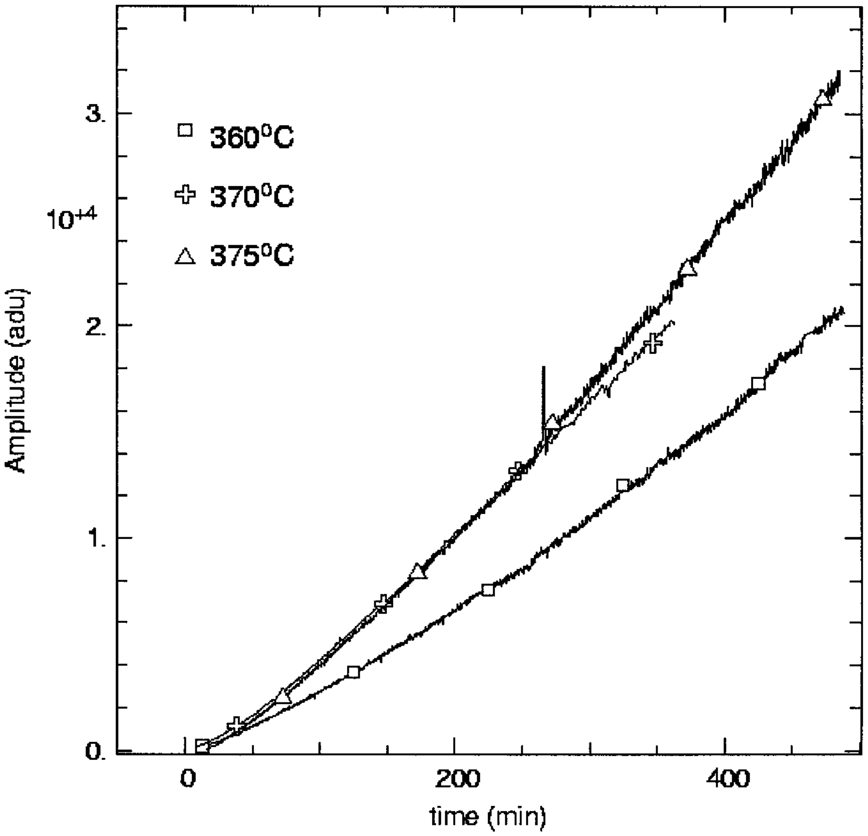

Fig. 4.21 Scattered amplitude as a function of time during during ordering processes at three different temperatures.

The ratio of the peak width in the two directions is, to a reasonable first approximation, a measure for the ratio of type-I and type-II domain wall densities. As it was already pointed out [33, 64], the low energy type-I walls are predominant. However as it can be seen in Fig. 4.22, this ratio decreases. This is explained by the fact that a type-I domain wall doesn't affect the local stoichiometry of the material hence less atomic transport is required to move such a domain. Relaxation of type-I domain walls occurs faster. From Fig. 4.22 we can also see how the relative density of type-I domain walls is higher at higher temperatures.

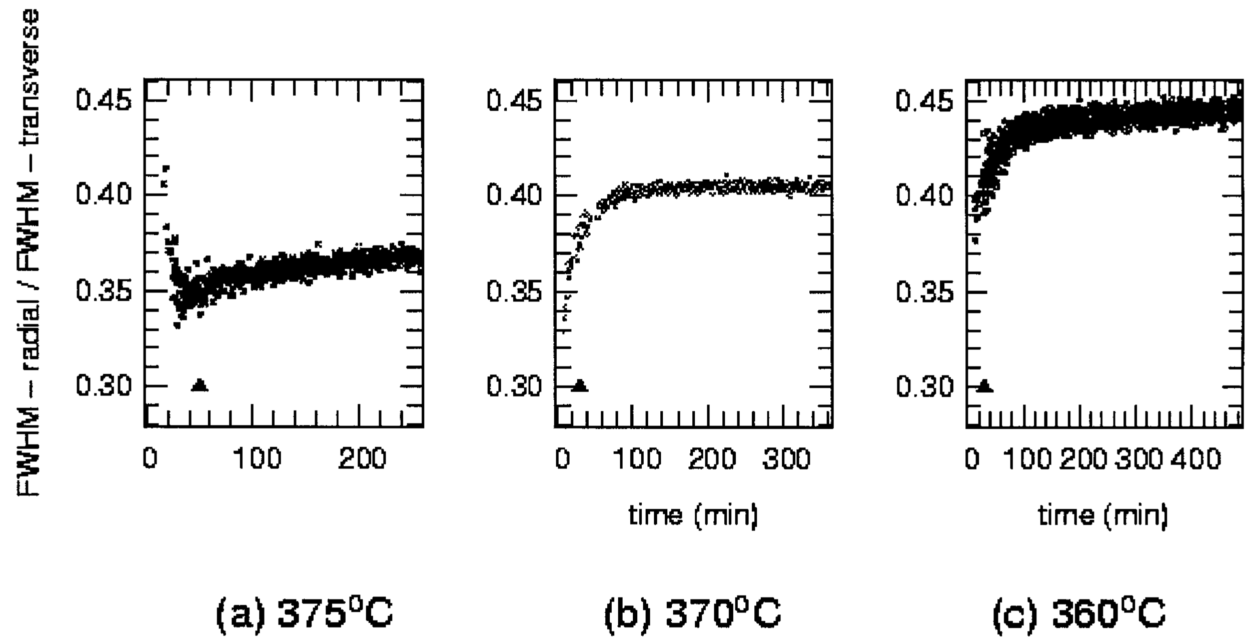

Fig. 4.22 The ratio of the FWHM of the Bragg peak in the radial and transverse directions measures (to a good approximation) the ratio between the type-I and type-II domain wall densities. This ratio is plotted throughout the ordering process for quenches at three different temperatures. The symbols on the lower axis indicate values of t before which the deviations from the $\sim t^{1/2}$ scaling law are important.

4.3.2 Domain wall induced lattice distortions

One of the parameters readily available from the fits to the time-evolving structure factor is the peak center, both in radial and transverse directions which is shown in Fig. 4.23.

From the fits one can see how the center of the Bragg peak shifts during the ordering process. This small shift is definitely not caused by a change in temperature because the ordering occurs at constant temperature.

The shift of the peak center is interpreted as a change in the average lattice constant

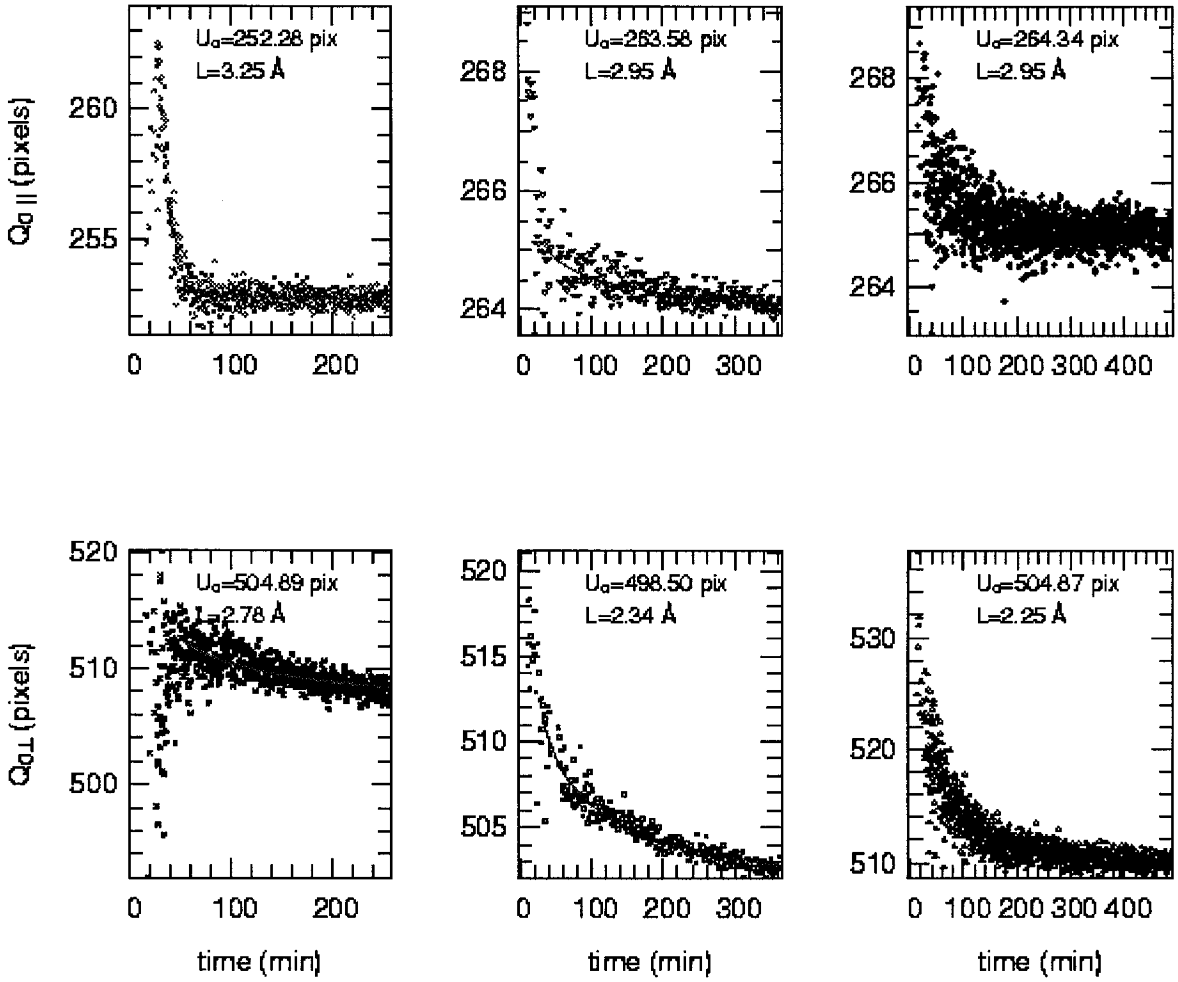

(a) 375°C (b) 370°C (c) 360°C

Fig. 4.23 Shift of the [100] superlattice peak throughout the ordering process. The center position (in pixels, 1 pixel=6.85×10^{-5} Å^{-1}) along a transverse and a radial direction is plotted against time for quenches at three different temperatures. Note: U_0=253 pixels corresponds to Q_0=0.9999 rlu and U_0=263 pixels corresponds to Q_0=0.9995 rlu caused by the domain walls. During the ordering process, the volume fraction associated with the domain walls keeps decreasing, hence the average lattice constant approaches its nominal value (3.71Å in Cu_3Au for this temperature range according to [33] and consistent with our estimates)

The direction of this shift is more difficult to interpret. The peak shifts by a larger amount in the transverse direction in reciprocal space with a smaller component in the [100] radial direction. Knowing that the type-II walls (which cause the peak width in the [100] direction) disturb the lattice more than the low-energy type-1 walls, this result seems counter intuitive.

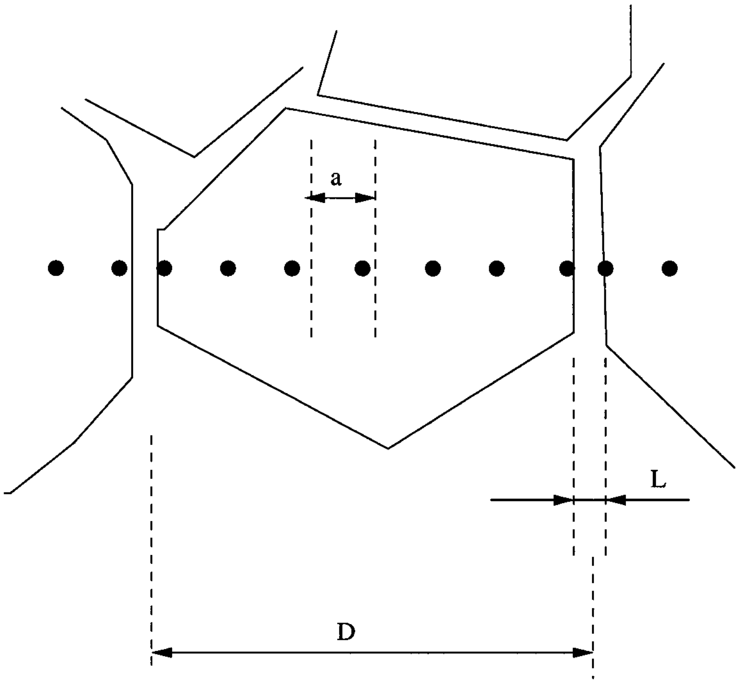

Fig. 4.24 In Cu_3Au antiphase domain of the ordered phase are separated by domain walls that affect the average lattice constant.

From the reciprocal-space shift of the superstructure reflection one can get a crude estimate for the domain wall thickness. With the following notation: a-lattice constant, D-average domain size, L-average domain wall thickness, (see Fig. 4.24) the average lattice constant can be approximated by a weighted average between the nominal lattice constant and the domain wall thickness,

$$\widetilde{a} = a\frac{D}{D + (a - L)}. \tag{4.6}$$

From Eq. 4.6 it results that a value $L = a$ would let the lattice undisturbed, $\widetilde{a} = a$, a value $L < a$ would "push" the atoms closer together and as a consequence would reduce the lattice constant, $\widetilde{a} < a$, while a value $L > a$ would increase the lattice constant $\widetilde{a} > a$. With q_0 and $\widetilde{q_0}$ defined by $q_0 = \frac{2\pi}{a}$, $\widetilde{q_0} = \frac{2\pi}{\widetilde{a}}$, the Eq. 4.6 becomes

$$\widetilde{a} = a\frac{1}{1 + \frac{a-L}{D}}, \tag{4.7}$$

$$\widetilde{q_0} = q_0\left(1 + \frac{a - L}{D}\right), \tag{4.8}$$

or, with U_0 and $\widetilde{U_0}$ the nominal and the shifted position of the peak centre on the detector (in pixels),

$$\widetilde{U_0} = U_0\left(1 + \frac{a - L}{D}\right). \tag{4.9}$$

The average domain size D and the domain wall thickness L are expressed in Å and U_0 in pixels. The results of the fits (to Eq. 4.9) are shown in Fig. 4.23 for both transverse and radial scans through the disk-shaped peak.

It is obvious from these results that the fits for the peak centre in the transverse direction, sensitive mainly to the dynamics type-I walls, will lead to slightly smaller values of the fitted parameter L, hence a more important distortion to the lattice constant than than the radial scans which is sensitive only to type-2 walls. Knowing that the type-2 walls "disturb" the lattice constant more than type-I walls and even change the nearest neighbor configuration at the interface this fact may seem surprising. On the other hand, the higher density of type-I domain walls is probably the factor and that causes the overall lattice distortion by this type of domain walls to be higher.

The values obtained for the fitted parameters, L and U_0 can be seen on the graph (Fig. 4.23). The values obtained for L, the domain wall thickness, are smaller than the lattice constant a at all temperatures, which means that both type-I and type-II domain walls are "pushing" the atoms closer together hence reducing the average lattice constant. The parameter U_0, which measures the equilibrium value of the lattice constant, depends on temperature as well. Such an effect has been observed by Rogge et. at. [56]. By doing neutron scattering over a wide temperature range, with particular emphasis on temperatures near T_c. Their results show a non-linear behavior in the ordered phase at temperatures between T_c and T_c-25C. The rate of change of the lattice constant (i.e. the slope $\frac{da}{dT}$) becomes as high as 0.0003 $Å^{-1}$ near T_c. Our results confirm this temperature dependence of the lattice constant. The parameter U_0 measured from the radial scans changes by 10 pixels, which corresponds to $\sim 7 \times 10^{-4}$ $Å^{-1}$ for a temperature change of 5 C (from 375 C to 370 C).

As it can be seen from Fig. 4.23 the lattice constant distortions are very small. Even the largest measured shifts are still slightly smaller than $\sim 10^{-3}$ $Å^{-1}$. Such a small shift is smaller that the spatial resolution provided by earlier experiments on the ordering process in Cu_3Au (Ref. [33]) and this explains why it couldn't have been detected in those studies.

In summary, we have observed that in addition to creating an non-isotropic scattering from Cu_3Au undergoing an order-disorder phase transition, the two types of antiphase domain walls present in such samples also cause a shift in reciprocal space of the superlattice Bragg reflexion during the ordering process. This shift was interpreted as a distortion of the lattice constant induced by the domain walls. The model proposed in this section explains well this shift in the late stages of the process. During the ordering process, this distortion is reduced by the relaxation of both types of antiphase domain walls and the lattice constant approaches its nominal value. However, the picture seems to be more complicated during the early stages of the process. More important distortions of the lattice constant are harder to explain with such a simple model. During the early stages even the relative concentration of type-I and type-II domain walls changes, as it was shown in Fig. 4.22 and this may be related to the more important distortions of the lattice constant observed here. However, in order to have a better picture on the processes occurring during the early stages of the process, new experiments providing better time resolution are required.

4.4 "Two-time" (correlation) analysis

The main advantage in using a partially coherent X-ray beam is the detection of the so-called "speckle pattern" in the scattered radiation. The speckle pattern measures the exact structure factor and fluctuates in time as a result of the fluctuations in the scatterer. Measuring the fluctuations in the scattered intensity will provide thus, valuable information about the dynamics of fluctuations in the system under study.

In order to measure the fluctuations in the scattered intensity, $I(\mathbf{q},t)$ one needs an estimate of the "average" intensity $\langle I(\mathbf{q},t)\rangle$, which is the intensity that would be measured by an incoherent X-ray beam. To calculate an ensemble average is not always straightforward in non-equilibrium systems, and more details will be given in the next section. A typical scattering data frame at a certain time during the ordering process is shown in Fig. 4.25. The speckled aspect of the diffraction pattern which can be seen in most of the detector area, is a consequence of the coherent illumination of the sample. However, the upper-left corner has been replaced with the average (incoherent) intensity, $\langle I(\mathbf{q},t)\rangle$. From here, a normalized intensity fluctuation can be defined as,

$$D(q,t)=\frac{I(q,t)-\langle I(q,t)\rangle}{\langle I(q,t)\rangle}. \tag{4.10}$$

This is, of course, static in the sense that the fluctuations have been calculated and shown for a single frame, at a given time. In order to have a good-enough contrast to resolve the speckles, the exposure time has to be short enough. Otherwise the fluctuations reduce the speckle contrast or even cancel it completely. Even more interesting, is the measurement of fluctuations as a function of time, which is known as "intensity fluctuation spectroscopy". Of course, here as well, the exposure time has to be short enough to capture the speckle patterns.

The intensity fluctuations calculated for a row of pixels perpendicular to (h00) as a function of time are shown in Fig. 4.26. Such a plot is sometimes referred to as a "waterfall plot". It is obvious from here that some interesting dynamics take place in the system. The fluctuations slow down as the system evolves. This phenomena is called "persistence". From Fig. 4.26 one can also see that fluctuations slow down more at lower values of $\mathbf{q}$ (i.e. closer to the peak centre).

The way to analyze the fluctuations in scattered intensity was proposed by G. Brown et. al. in [9, 10]. Following their analysis of the numerical simulations describing the evolution of both model A and model B non-equilibrium systems, a correlation function can be defined by,

$$C\left(\overline{q},t_1,t_2\right)=\left\langle D\left(\overline{q},t_1\right)D^*\left(\overline{q},t_2\right)\right\rangle. \tag{4.11}$$

A contour plot of the two-time correlation functions (Eq. 4.11) following a temperature quench to 360°C is shown in Fig. 4.27. The values along the principal $t_1=t_2$ diagonal measure the coherence factor of the beam β, while a line perpendicular to the main diagonal

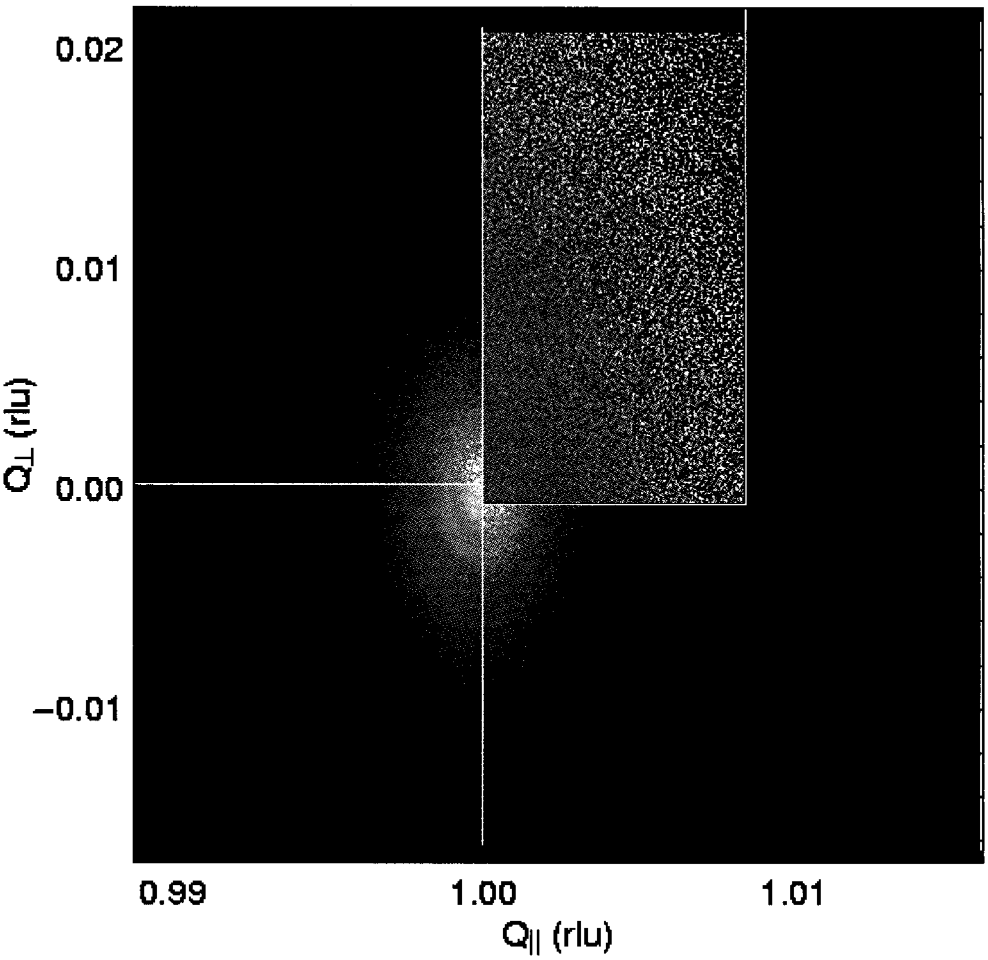

Fig. 4.25 Coherent ("speckled") scattered intensity - $I(\mathbf{q},t)$; Incoherent (average) intensity - $\langle I(\mathbf{q},t)\rangle$ (lower left inset); and normalized intensity fluctuations (Eq. 4.10) - $D(\mathbf{q},t)$ (upper middle inset).

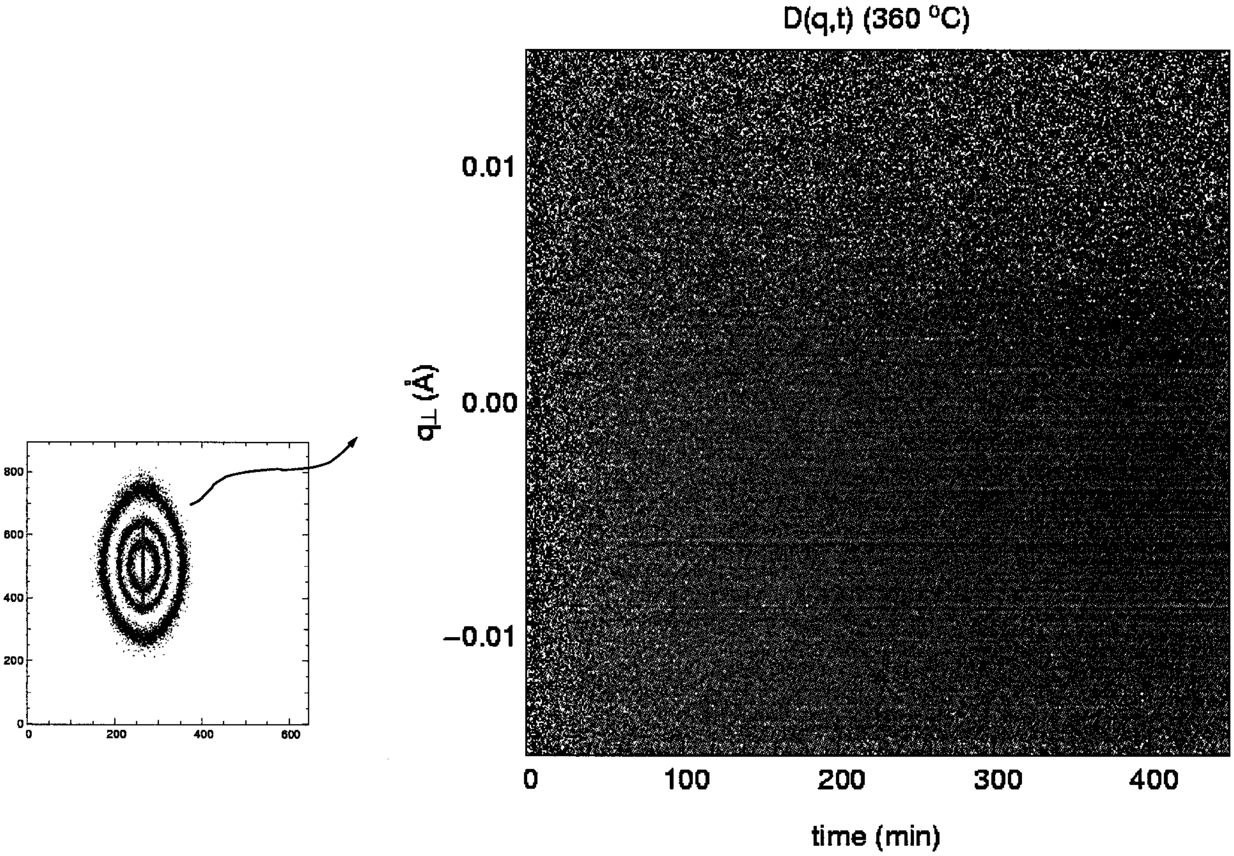

Fig. 4.26 "Waterfall" plot. Intensity fluctuations for a row of pixels (shown in the left inset), as a function of time, after a quench from the disordered phase to 360°C.

corresponds to a constant average time $\bar{t} = \frac{t_1+t_2}{2}$.

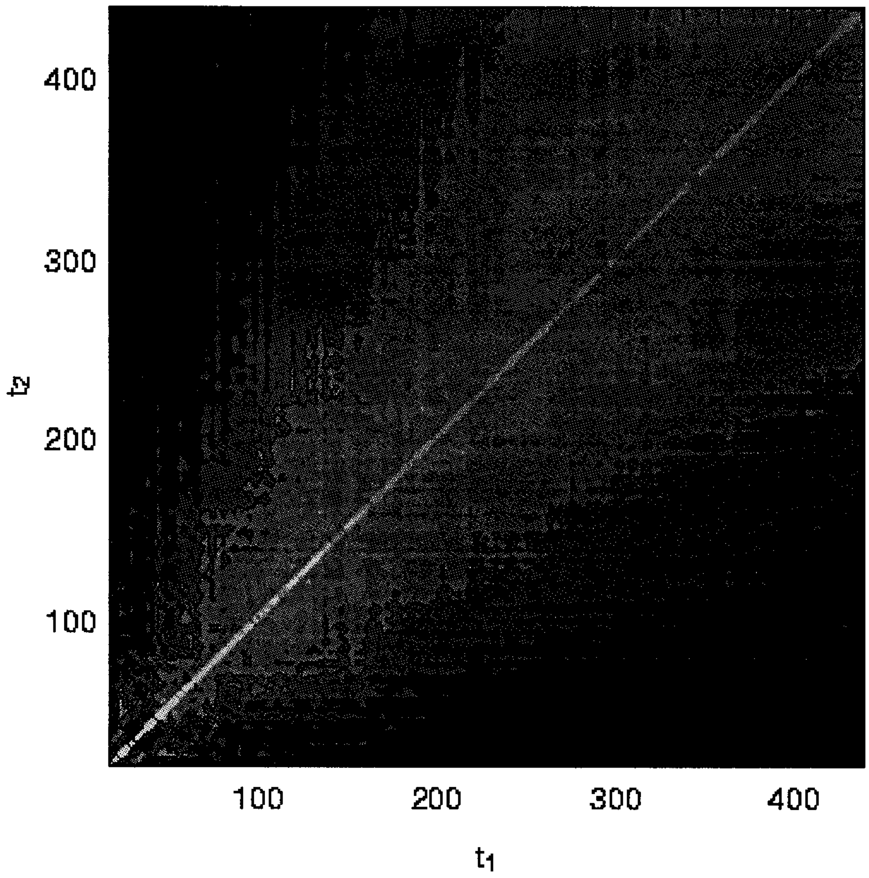

Fig. 4.27 Contour plots of the "two-time" correlation function $C(\mathbf{q}, t_1, t_2)$ during the ordering process. The temperature was of 370 °C and the scattering vector $q = |\mathbf{Q} - \mathbf{Q}_0|$ =0.00043Å^{-1}, in the radial (h00) direction.

The natural variables used to analyze the two-time correlations, are the average time $\bar{t}$ and the time difference $\delta t = t_1 - t_2$. The results of the two-time analysis will follow in Section 4.4.2. In the following section we will describe the technique employed to evaluate the average scattered intensity.

4.4.1 Average (incoherent) intensity $\langle I(\mathrm{q}, t)\rangle$

One of the main problems associated with performing XIFS measurements in non-equilibrium systems comes with the need to evaluate the average scattered intensity $\langle I(q,t)\rangle$. The average has to be viewed as an ensemble average of the fluctuating intensity $I(q,t)$ which measures the exact structure factor of the scattering material. In fact $\langle I(q,t)\rangle$ measures the structure factor that would be obtained from incoherent x-ray diffraction. In an equilibrium system $\langle I(q,t)\rangle$ is expected to be constant in time and can be evaluated simply by averaging $I(q,t)$ over a long-enough time interval. However, in a non-equilibrium system $\langle I(q,t)\rangle$ changes with time and separating the intensity fluctuations from this changing average becomes a non-trivial issue. If the scattering is isotropic, $\langle I(q,t)\rangle$ can be evaluated by averaging over intensities at constant q. This was the approach used by the authors in refs. [44, 38] who considered few-pixels wide annuli centered around the center of the Bragg peak. For our particular experiment this approach is not an option because of the anisotropy of the superlattice scattering.

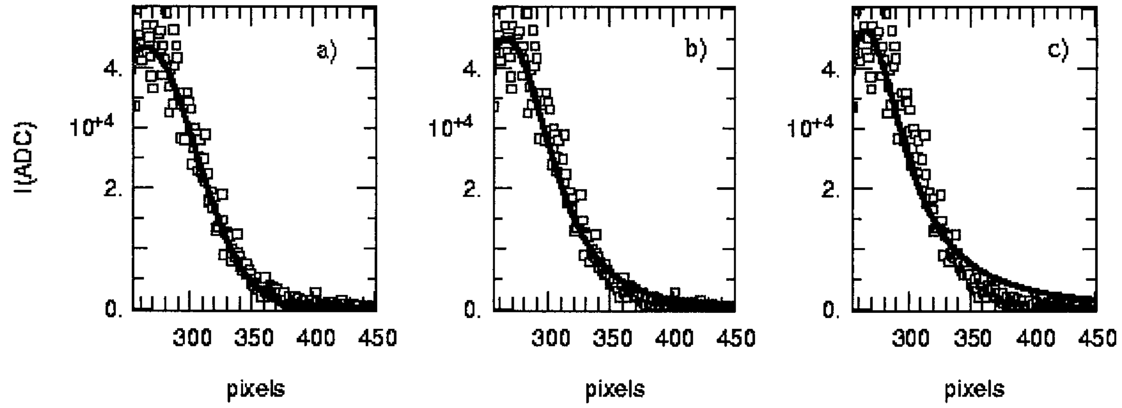

Fig. 4.28 Least square fits to the scattered intensity with: a) Gaussian; b) squared Lorentzian and c) Hendricks-Teller (Eq. 4.4)

The incoherent (average) scattered intensity $\langle I(q,t)\rangle$ could also be evaluated by least-square fitting various analytical forms for $I(q,t)$ to the measured intensities. Example fits of the scattered intensity to a 2D Gaussian (G2D) profile, a squared Lorentzian (L2) and a Hendricks-Teller (HT) form (Eq. 4.4) are shown in Fig. 4.28. As it can be seen, the fits work generally well. Surprisingly, the G2D fits seemed to work better than the both L2 and HT ones. However, as with any least-square fits, areas in a certain q-range are affected by small systematic errors. The areas affected most by the least-square fits are the tails of the diffraction peak. While the G2D fits have, as expected, too short tails, for both the HT and L2 profiles the tails are a bit too long. The systematic errors in the fits affect the measured fluctuations, especially at higher q, where the scattered intensity is low, and as it will become clear below, will affect even more the correlation functions. Very simply stated, systematic errors "correlate" very well. In order to take full advantage of the whole q-range allowed by the CCD detector, the average or incoherent intensity $\langle I(q,t)\rangle$ was calculated by using a two-dimensional Strawitzky-Golay (SG) smoothing filter [52].

The basic idea behind a SG filter is to use a polynomial form in order to least-squares fit the data in a window that is large enough that the fits are not affected by the fluctuations and small-enough that the particular polynomial form we chose doesn't bias the evaluated, fitted, quantity. In practice, we scan the entire CCD detector with a 11 x 11 pixels window, and at each location the data in the window is fitted by a two-dimensional polynomial form. The fitted value at the center of the window is considered to be the incoherent scattered intensity for that particular pixel. In Fig. 4.29 we show the SG estimate for the incoherent intensity for a horizontal line of pixels through the peak center at t=300 min after the quench at 370°C. For comparison, the corresponding G2D, L2, and HT least-square fits are shown as well.

As it can be seen, the SG filtering procedure provides a much more credible estimate for the incoherent intensity $\langle I(\mathbf{q},t)\rangle$. By assuming that the mean square deviations add in quadrature, the mean square deviation of the coherent scattered intensity σ_I can be written

$$\sigma_I = \sqrt{\sigma^2_{\langle I\rangle} + \sigma^2_{speck}}. \tag{4.12}$$

Here $\sigma_{\langle I\rangle}$ represents the error of the Savitzky-Golay estimate of the average intensity and σ_{speck} is the variance in the scattered intensity due to speckles. From Fig. 4.29 one can estimate $\sigma_{\langle I\rangle}$ to be at least an order of magnitude smaller than the variance of the scattered intensity σ_I and therefore assuming that the variance in the scattered intensity is totally due to speckles is a valid approximation. All the results of the two-time analysis presented in the following sections have used the SG estimate for the average intensity.

4.4.2 Two-time analysis: results

With the average intensity $\langle I(q,t)\rangle$ evaluated by a Savitzky-Golay filter, two-time correlation functions were calculated for several values of $\mathbf{q}$ along both radial and transverse directions and for three different temperatures (360°C, 370°C and 375°C) using Eq. 4.11.

Here as well, the non-isotropic scattering imposes severe restrictions on the area of the CCD detector that can be used to calculate the averages. In homogeneous systems, the correlation function is expected to depend only on the absolute value $q = |\mathbf{q}|$ and circular

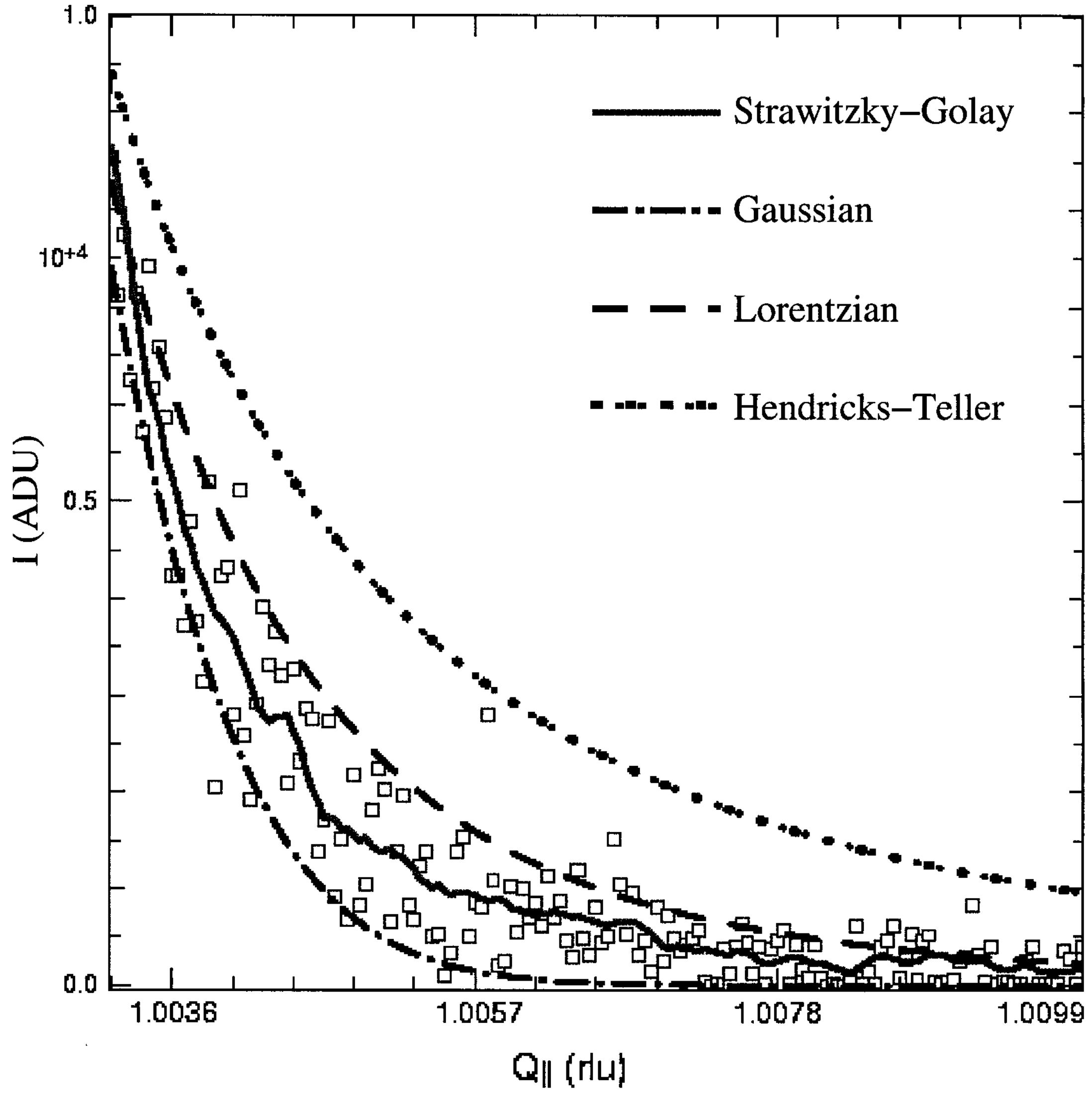

Fig. 4.29 Various estimates for the incoherent scattering $\langle I(q,t)\rangle$. Savitzky-Golay filters and least-square fits with Gaussian, squared Lorentzian and Hendricks-Teller functions.

averages can be used to improve statistics. This is not the case in our system. To calculate the correlation functions, the intensity fluctuation correlations were averaged over relatively small areas of a few pixels (10 x 10, 10 x 20 or 20 x 30 for high q values) all consider to have similar time dependence.

As it was explained in Chapter 2 (Eq. 2.33) and was first pointed out by Brown et. al. [9], the intensity correlation functions measure two-time two-point correlations functions in the order parameter which is the density of ordered material. The intensity covariance or two-time correlation functions can easily be calculated from the experimental data as products of the intensity fluctuations for a given **q** at two different times (averaged over several pixels in order to improve statistics). This function measures two-time correlations of the density fluctuations. Contour plots calculated using Eq. 4.11 are shown in Fig. 4.30 for two different q values along a radial direction ($q_{||} = Q - Q_0 \simeq 0.001$ Å $^{-1}$ and $q_{||} \simeq 0.003$ Å $^{-1}$) and three different temperatures. A similar set of images can be obtained for values of **q** along transverse scans. Correlation functions for scattering vectors of $q_{\perp} \simeq 0.006$ Å^{-1} and $q_{\perp} \simeq 0.008$ Å^{-1} are shown in Fig. 4.31.

These results for the two-time correlation functions show some interesting features. First, there is a **q** dependence of the two-time dynamics. For both radial(Fig. 4.30) and transverse (Fig. 4.31) scans, the corelation times become shorter at larger wavelengths. Also there is an important temperature-dependence, which is more difficult to quantify from these plots but will be addressed later. However, the most striking and somehow unexpected features shown by the contourplots, are the large "incubation times". In all the graphs, the $t_1 = t_2 = 0$ origin represents the moment of the quench, yet the correlation times start to increase only after times ranging from 20-30 min up to 50 min. These times are shown by the white symbols in Figures 4.30 and 4.31. The complex time evolution of the correlation functions is a consequence of the evolution of the system towards the equilibrium (ordered) state. In an equilibrium system, they are constant in time and the contour plots would consist of lines parallel to the $t_1 = t_2$ diagonal.

Following the analysis of [9] the two-time correlation functions are expressed in terms of a natural set of variables, the average time $\bar{t} = (t_1 + t_2)/2$ and the time difference $\delta t = |t_1 - t_2|$. A constant value of $\bar{t}$ corresponds (see Fig. 4.30) to a line perpendicular to the $t_1 = t_2$ diagonal and δt measures the distance from the equal time diagonal (in units of time) along such a line. The large $\bar{t}$ asymptotic limit of the normalized correlation function can be obtained in an explicit form [9]. For a three-dimensional system, the predicted form

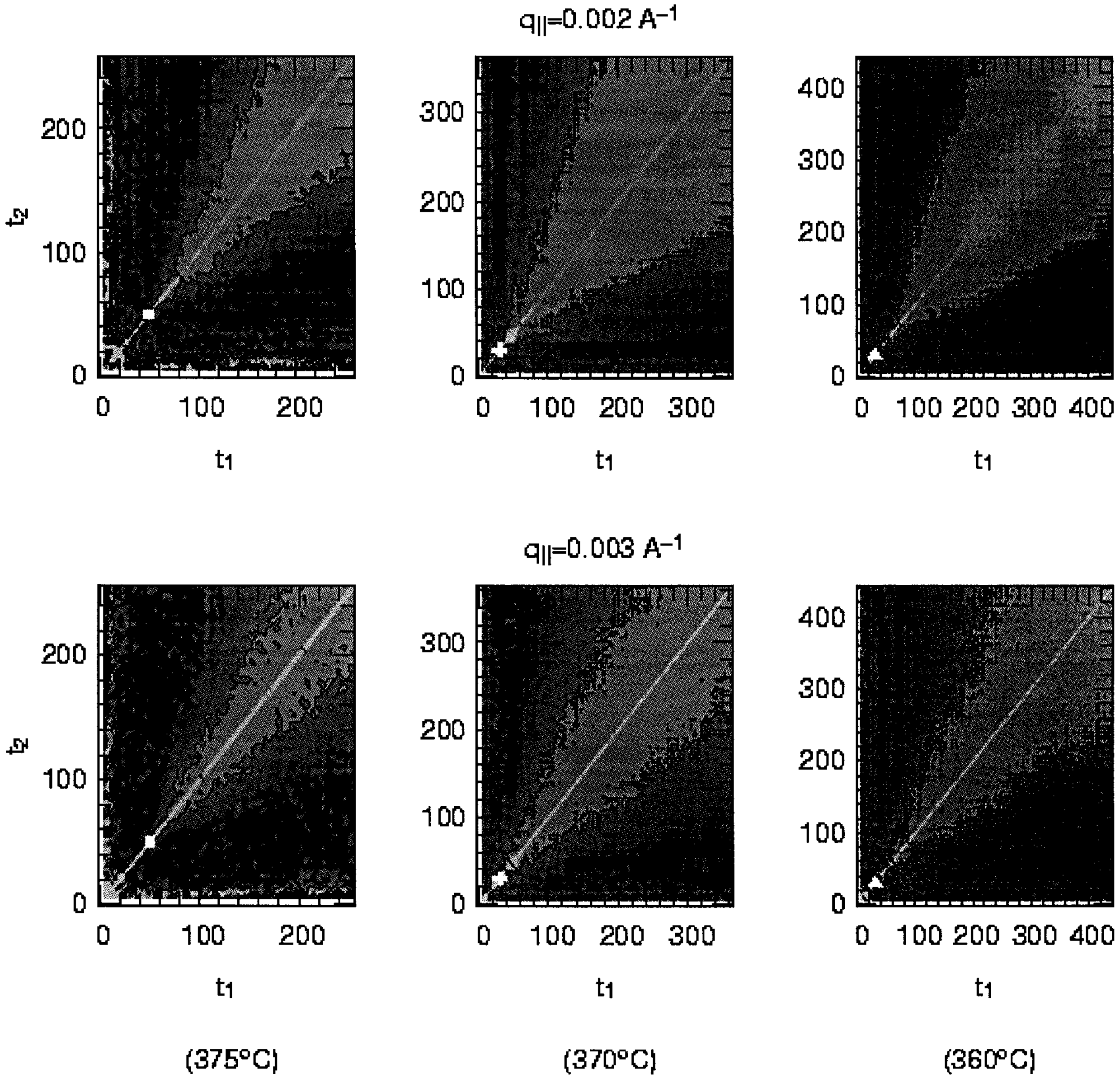

Fig. 4.30 Contour plots of the two-time correlations functions for two different q values along (h00) (radial scans) at three different temperatures; levels are 0.001, 0.002, 0.004, 0.008 and 0.0016; the black contours correspond to a level of 0.004 which is roughly half the coherence factor $\beta \simeq 0.008$.

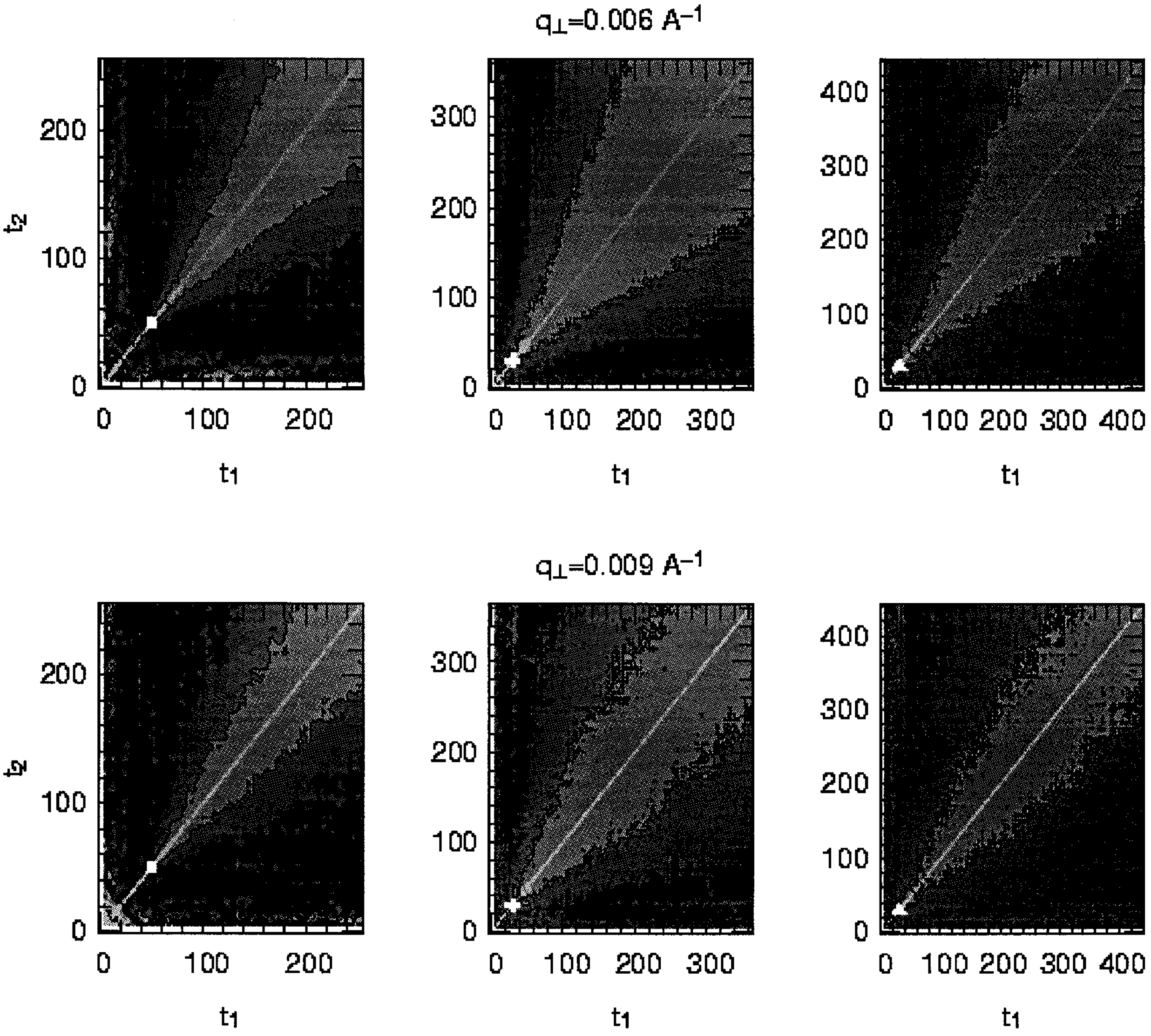

$q_\perp$=0.006 A^{-1}

$q_\perp$=0.009 A^{-1}

(375°C) (370°C) (360°C)

Fig. 4.31 Contour plots of the two-time correlations functions for two different q values along a transverse scan at three different temperatures; levels are 0.001, 0.002, 0.004, 0.008 and 0.0016; the black contours correspond to a level of 0.004 which is roughly half the coherence factor $\beta \simeq 0.008$.

is,

$$C_{norm}(z) = \left(z^2 K_2(z)/2\right)^2 . \tag{4.13}$$

The scaling variable is $z = A\delta t/\bar{t}^{1/2}$, where A makes the variable dimensionless and $K_2(z)$ is a modified Bessel function of the second kind. This form can be approximated [38] by $C_{norm}(z) \simeq e^{-2z}\left(1 + z + z^2/4 - z^3/12\right)^2$, valid for $z < 3$. The value of z for which C_{norm} falls to 0.5 can be calculated numerically, $C_{norm}(z_{1/2} = 1.2597) = 0.5$. In practice the measured correlation functions are fitted to the form

$$C(\delta t, \tau) = \beta C_{norm}(z_{1/2} * \frac{\delta t}{T}). \tag{4.14}$$

The two parameters in the fit are β, the coherence factor and T, the characteristic time for the two-time correlations. Values of the correlation function along the $t_1 = t_2$ diagonal contain a term from the Poisson noise in photon counting and a term from the coherence in the beam. As the Poisson noise is present only in the equal-time correlations, previous XIFS experiments in non-equilibrium systems [38] have calculated the diagonal terms by averaging the neighboring elements. In this analysis, the diagonal elements were simply omitted in the fits, and the parameters β and τ were calculated by using only the non equal-time correlations.

The coherence factor β was thus indirectly measured from the fits of the two-time intensity autocorrelation functions. From Fig. 4.32, it can be seen that the degree of coherence of the X-ray beam used in these experiments was roughly 0.8%. This was certainly lower than what we expected considering the source characteristics and the characteristics of the X-ray spectrometer and at this point it is not clear if this is due to vibrations in the experimental set-up which was not designed specifically for experiments with coherent X-rays, or if it is due, for instance, to some fast dynamics taking place in the sample. However, even with a coherence factor of $\beta \sim 1\%$, the speckle contrast is roughly $\sqrt{0.01} = 10\%$. This relatively high contrast proved to be sufficient to obtain the results reported in this chapter.

The fitted two-time correlation times T can be seen in Fig. 4.33, as a function of the average time, for several values of the scattering vector q. The temperature is 360 °C.

Similar with "one-time" quantities such as the scattered intensity or the width of the Bragg peak, the two-time correlation function can be rescaled to an universal form if the

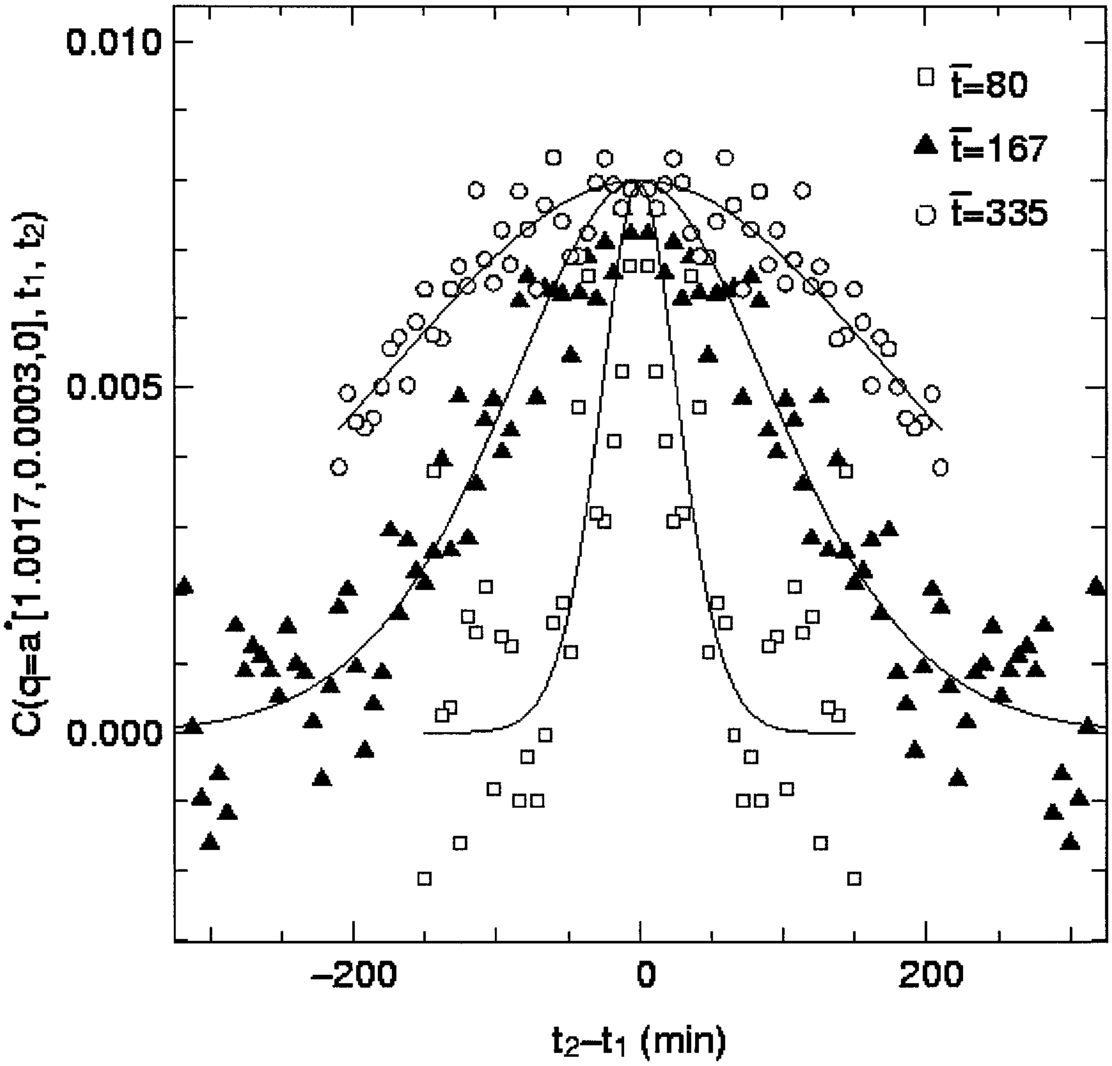

Fig. 4.32 Fits of the two-time correlation functions with Eq. 4.13 for three values of the average time $\bar{t} = (t_1 + t_2)/2$.

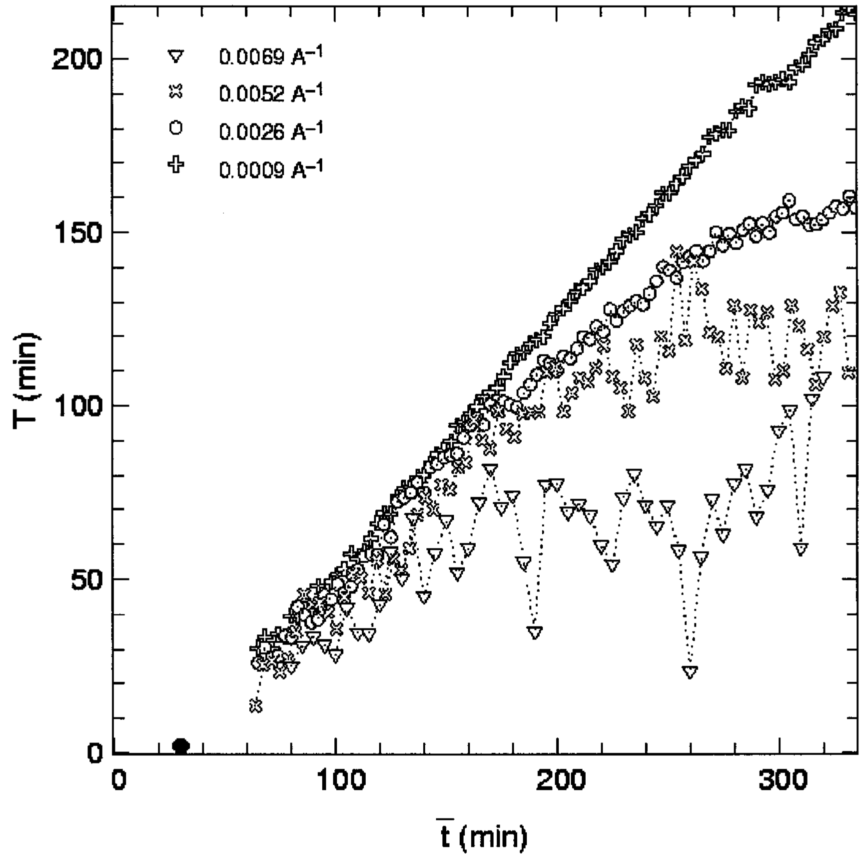

Fig. 4.33 Fitted correlation as a function of the average time for some values of **Q** along the [100] direction (radial scan).

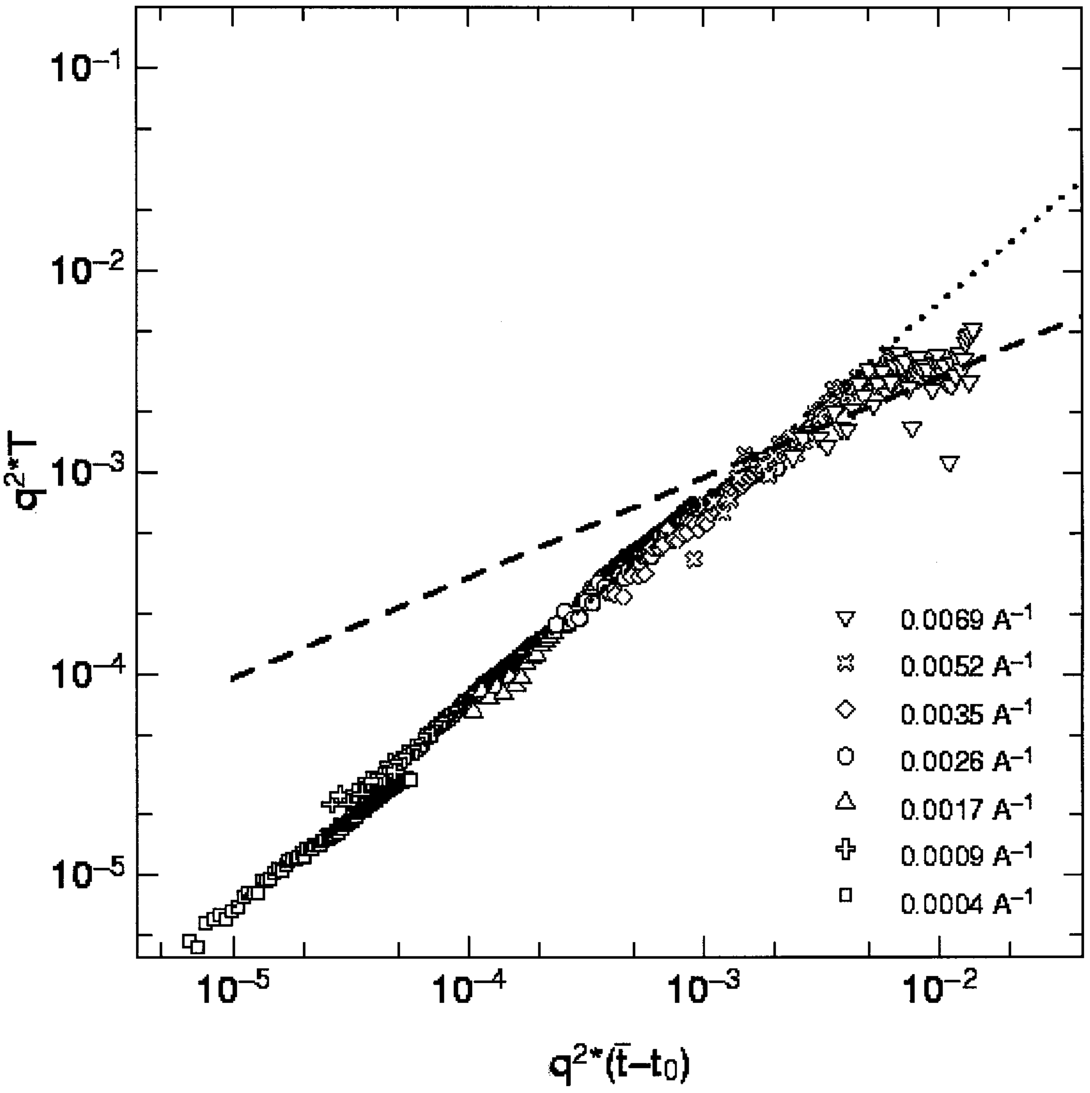

Fig. 4.34 Rescaled fitted correlation times for all q values along the [100] direction (radial scan). The non-scaled correlation times for some values of q are shown in Fig. 4.33. The dotted line has a slope of 1 and the dashed line a slope of 1/2.

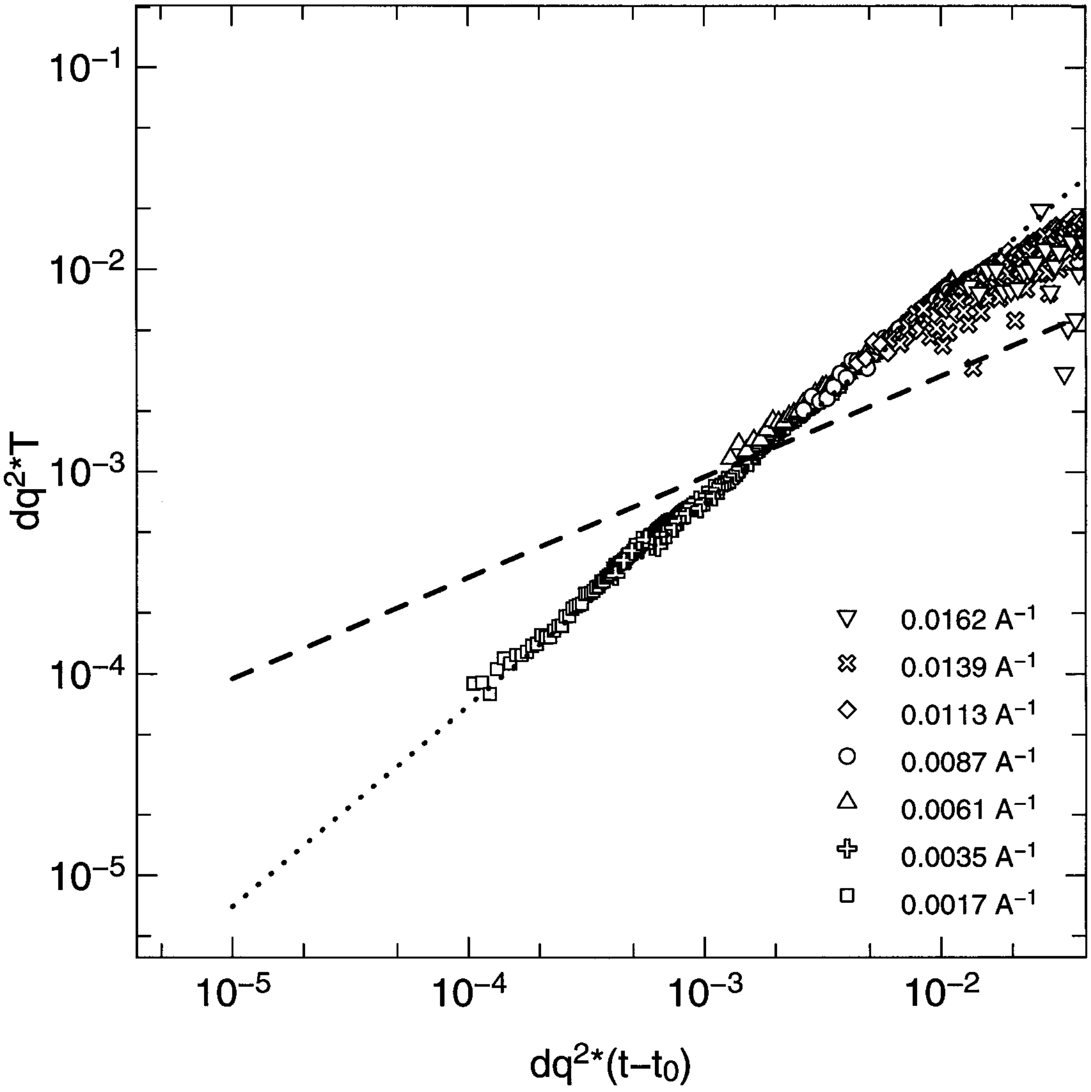

Fig. 4.35 Rescaled fitted correlation times for values of the scattering vector **Q** along a direction perpendicular to [100] (transverse scan). The dotted line (slope of 1) and the dashed line (slope of 1/2) are at exactly the same positions as those in Fig. 4.34. The inset shows the non-scaled correlation times for some values of **Q**.

involved times are rescaled. The characteristic time, $\tau = Tq^2$ follows an universal curve if plot against a rescaled average time $\bar{t}q^2$. For model A, the small and large t asymptotic limits should be [9, 10] $\tau \sim \bar{t}$ respectively $\tau \sim \bar{t}^{1/2}$. The measurements from a radial scan through the [100] superlattice peak after a quench at 360°C are shown in Fig. 4.34. The dotted line has a slope of 1 and the dashed line a slope of 1/2. the time scales covered in these experiments extend over a few decades $\left(10^{-5} \le \bar{t}q^2 \dot{\le} 10^{-1}\right)$. Experimentally, we are limited by the area over which the intensity is sufficiently large to allow a good estimate of the corresponding incoherent intensity and speckle fluctuations and by the maximum time for which the spectrometer is stable or even the maximum beam time available in an experimental run. In this study we measured the speckle fluctuations after quenches at 375°C, 370°C and 360°C for 4h, 6h and respectively 8h. In order to increase the range for the rescaled time and to improve statistics, the use of a spectrometer better optimized for coherent X-ray diffraction will have the highest impact because this would allow the use of a larger q-area.

The same analysis was done for all values of q along a transverse scan through the Bragg peak (Fig. 4.35). The transverse scans measure the dynamics of type-I domain walls. The dotted lines (slope 1) and the dashed lines (slope 1/2) in Fig. 4.34 and Fig. 4.35 are drawn at the same positions. One can see how the only difference between the rescaled correlation function plots is that the "kink", or transition from a linear dependence $T \sim \bar{t}$ to a power law dependence $T \sim \bar{t}^{1/2}$, happens a little bit later for a radial scan. This is probably due to the higher density of type-I domain walls. It is not surprising that it takes a longer time until the system relaxes to the point where the increase in the two-time correlation function "slows down" because of a reduced thermodynamic force (free energy difference)

An important aspect is that, in order to make the scaling form work, the average time $\bar{t}$ was not measured from the moment of the quench, but rather from the moments marked by the white symbols in Figures 4.30 and 4.31. Without this shifting of the time origin, the rescaled correlation times do not collapse as well on an universal curve and is also temperature dependent. Even in Figures 4.30 and 4.31 it can be seen that, for a given wavevector, the two time correlation functions are lowest at 375°C and they are approximately constant (and higher) in the reach 360°C - 370°C temperature range. However, by shifting the time origin to the temperature-dependent characteristic times marked in Fig. 4.30, the two-time correlation functions can be rescaled to a temperature-independent form. As it can be seen these characteristic times represent the moments when the fluctuations start being persistent and, to our experimental accuracy, they contain all the temperature-dependence in the system. The the two-time scaling shown in Fig. 4.34 for radial scans and in Fig. 4.35 for transverse scans were obtained from scattering data following the 360°C quench, but the data from the 375°C and 360°C quenches collapse well on the same master curve as it can be seen in Fig. 4.36. The position of the two straight lines with slopes 1 and 1/2 are the same in all the graphs showing the rescaled two-time correlation functions obtained from radial and transverse scans at the three different temperatures. Although some deviations can be seen, especially at 375°C, one can conclude that, within our experimental accuracy, this forms are temperature-independent and all the temperature dependence is contained by the "incubation times" t_0.

The temperature dependence of the incubation times t_0 can be seen in Fig. 4.37 and be compared with the temperature dependence of the characteristic times for "one-time" kinetics, shown in Fig. 4.19. The temperature dependence for both "one-time" and "two-times" kinetics, is a result of the competition between an increased thermodynamic force (free energy difference) associated with a lower final temperature and a reduced atomic mobility. As it was pointed out in Section 4.3, in the 360-370°C temperature range, the kinetics of the domain growth is diffusion limited. The rate of growth is slower for a deeper quench. The temperature-dependence of the "two-time" kinetics, seems to be, however, qualitatively different. The optimal temperature, leading to the fastest increase in the two-time correlation functions seems to be somewhere between 360°C and 370°C. At higher temperatures (375°C) the kinetics seem to be already limited by the thermodynamic force (free energy difference). In both cases, the difference in free energy vanishes at the critical temperature and both the one-time and the two-time dynamics are expected to become infinitely slow. This different behavior could perhaps be explained by the fact that the autocorrelation functions of the scattered intensity measure the dynamics of the order parameter which is determined by both the bulk and the surface contributions to the free energy, while the kinetics of growth of the average domain size is determined mainly by the reduction of the surface free energy associated with the antiphase domain walls.

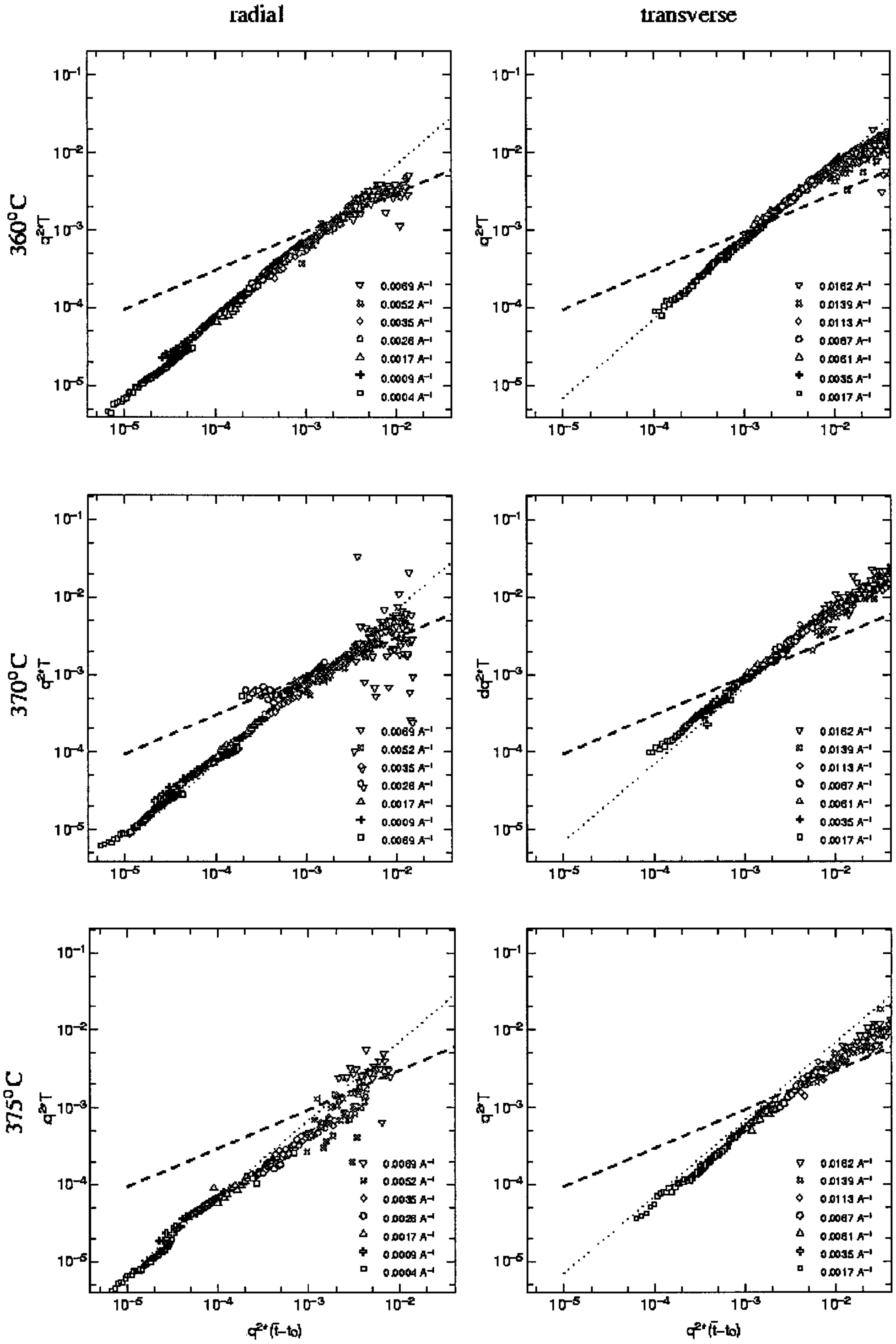

Fig. 4.36 Rescaled two-time correlation times vs. rescaled average time for three temperatures and both radial and transverse scans.

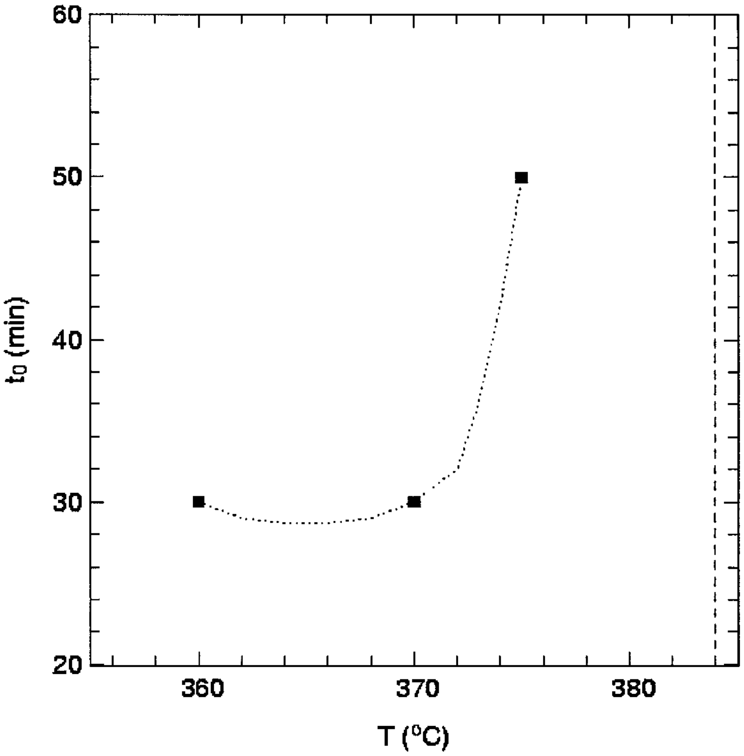

Fig. 4.37 Temperature dependence for the "two-time" kinetics - characteristic time t_0 ("incubation" times) as a function of the ordering temperature.

Chapter 5

Conclusions and outlook

In conclusion, the results presented in Chapter 4 are the first experimental confirmation of the scaling of the two-time correlation functions in a first-order phase transition with non-conserved order parameter (model A). The coherent X-ray scattering data was recorded during quenches from the high-temperature, disordered phase in Cu_3Au to three different temperatures below the critical point. This allowed us to obtain information about the temperature-dependence for the kinetics of both "one-time" quantities such as the scattered amplitude or the average domain size, and of "two-time" quantities such as the autocorrelation functions of the scattered intensity. The experimental results are in good agreement with the scaling laws for the two-time kinetics proposed in previous theoretical work. At the same time the data suggests some interesting behavior in the early stages of the process. It is generally accepted that the scaling picture describes correctly only the late, coarsening stages of the process when the ordered domains are well formed. From the experimental data presented in this thesis as well as from other experimental results on the early-stage dynamics in Cu_3Au [40], and theoretical predictions on the dynamics of such processes [27] one can expect the early, nucleation and growth stages of the ordering process to last for times of the order of seconds or tenths of seconds, which is below the time resolution obtained in the experiments presented here.

The data shown in Fig. 5.1 supports this assumption. The integrated intensity, which measures the order parameter is a good estimate for the total concentration of ordered material and, as it can be clearly seen, reaches a constant value in times which may be shorter than the time it took to record the first CCD frame. An exception is the data

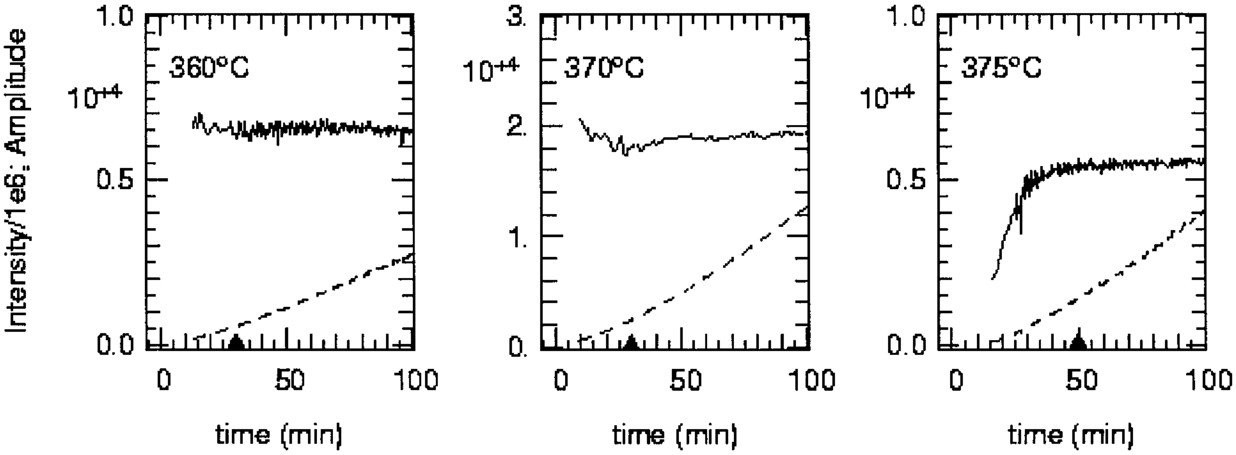

Fig. 5.1 Scattered amplitude and integrated intensity during the early stages of the ordering process. The symbols on the lower axes indicate the characteristic time for two-time correlations, t_0.

at 375° where this process seems to be a bit slower, but even at this temperature, the estimated time required for the sample to reach the coarsening regime is much shorter than any other measured time.

This picture would suggest that the scaling regime is reached very quickly after the temperature quench and that the time dependence for both one-time and two-time quantities should follow the scaling behavior. From this point of view the "incubation times" for the two-time scaling that were reported in the previous chapter are a surprise. These times can be seen in Fig. 5.1 as well (symbols on the lower axis).

If the early-stage (nucleation and growth) regime cannot explain these deviations from the scaling behavior, this could suggest that another, not yet understood relaxation process may exist in the intermediate stages of the ordering process. The shift of the peak centre and the aspect ratio of the Bragg peak, obtained from the "one-time"analysis (Section 4.3) seems to point in the same direction and suggest the existence of another relaxation mechanism. The model describing the shift of the peak centre in reciprocal space by considering domain wall induced distortions of the lattice constant (Section 4.3.2) cannot explain well enough the process during the early and "intermediate" stages, for times ranging from the moment of the quench, t=0 up to the the incubation times t_0. In fact the fits for the position of the peak centre shown in Fig. 4.23 were done for times ranging from the incubation times t_0 up to the late stages of the quenches. Similarly, the incubation times are represented by the symbols on the lower axis in Fig. 4.22 and this suggests that at earlier times the relative concentration of type I and type II domain walls change and do not follow a thermal distribution. At some level even the data proving the $\sim t^{1/2}$ growing law (Fig. 4.15) shows some subtle deviations from the scaling behavior in the early stages

These observations, all "point" in the same direction and suggests that some relaxation mechanisms which are not yet understood may take place during the "intermediate time" regime, from t=0 to t=t_0. This raises also some important questions about the meaning of the "two-time" analysis presented in Section 4.4.2 during these stages. The whole scaling picture tested by our analysis is based on calculating intensity autocorrelation functions at a single wavevector, $\mathbf{q} = |\mathbf{Q} - \mathbf{Q_0}|$. In our analysis, the small shifts of $\mathbf{Q_0}$ reported in Section 4.3.2 have been accounted for, but the deeper question remains unanswered:
How does the scattered intensity at a vector $\mathbf{q}$ *autocorrelate in time, in a system where* Q_0 *is rapidly changing? What do those correlations mean?*

Fortunately, with the high-brilliance X-ray sources like the the APS and the fast temperature control technique presented in Chapter 3, experiments to probe those regimes are possible and are in fact being planned. In order to obtain better long-wavelength resolution and better statistics on the early-time kinetics, X-ray focusing optics such as Fresnel zone plates can be used. Recent unpublished results indicate that the flux per speckle is also increased by focusing the beam. The use of a focusing zone plate in conjunction with a beam with a higher degree of coherence than was used in the experiments described in Chapter 4 of this thesis will allow much better measurements during the initial stages of the ordering process and may answer some of the questions raised by the present study.

On a broader scale, this thesis presents an application of diffraction with coherent X-rays to study dynamics in a non-equilibrium system. This a very new field of study and the XIFS method offers tremendous possibilities in studying numerous systems with different dynamics. From this point of view, the science of soft condensed matter which is understood in a very broad sense as the physics of non-crystalline materials with complex structures and complex interactions [62], has already provided some applications for XIFS studies of equilibrium dynamics [34, 57, 42] and is likely to provide new applications for studies of non-equilibrium dynamics. As is pointed out by Terentjev [62] the internal degrees of freedom of such complex systems are often very slow. Whether the system is a "polymer brush" , a system of proteins or a liquid crystal, it can often be brought into states which are far away from their equilibrium from which they evolve, sometimes very slowly, towards equilibrium or quasi-equilibrium states. The "key phrase" for possible applications for the

XIFS technique is “slow dynamics”. In this thesis we studied dynamics in metallic alloys on time scales of minutes or tenths of minutes. Reaching the technological limits of this technique, Kim et. al. have studied equilibrium dynamics in liquid crystals down to 50ns. This is the time range accessible with todays synchrotron light sources and soft condensed matter systems seem to be ideal candidates for new and interesting XIFS studies of non-equilibrium dynamics.

Appendix A

Thermal Model

In order to understand the thermal configuration in the “hotplate” oven used in the study of the order-disorder phase transition in Cu_3Au, the temperature distribution as a function of the distance along a direction perpendicular to the plane of the heater and time - $T(x,t)$ - was calculated, using a simple one-dimensional model.

The model is schematically shown in Fig. A.1. The boron nitride (BN) heater, W buffer later and Cu_3Au sample are mounted on a cooled copper post held at a constant temperature T_0 by a water-cooling circulating system.

The time-dependent, one-dimensional heat equation can be written,

$$\frac{d^2T}{dx^2} - \frac{\rho c}{k}\frac{\partial T}{\partial t} = -\frac{q}{k}. \tag{A.1}$$

The notations are the usual ones introduced in Section 3.2.2. The power flux q, $\left([q] = \frac{W}{m^2}\right)$ is determined by the boundary conditions.

In order to keep the model as simple as possible, and still to “capture” all the important features of the system, five different finite elements have been considered across the layered structure. The BN heater was considered as one uniform temperature (T_1) block, while both W and Cu_3Au (referred to hereafter as the “Cu” layer) were modeled by considering two finite elements for each of them: T_2 and T_3 for the W block, T_4 and T_5 for the sample. Knowing the temperature distribution across the systems, means, in this simplified, finite element model, knowing a set of five temperatures: T_1,...,T_5.

With these specifications, we can write the complete set of equations describing the five element finite difference model for the “hotplate oven”. The thermal contact resistances at

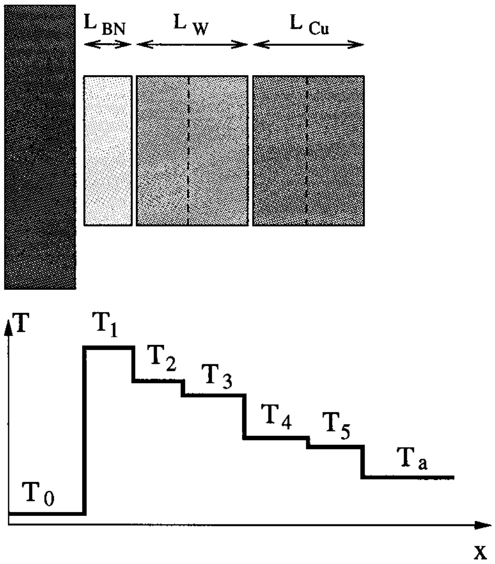

Fig. A.1 Thermal model for the "hotplate oven".

the three metal-metal interfaces are defined as R_0, R_1, R_2, the electric power supplied by the BN heater is P, and with the rest of notations obvious, we can write:

$$\begin{aligned}
\frac{P}{A} - \frac{T_1-T_0}{R_0} - \frac{T_1-T_2}{R_1} &= \rho_{BN}c_{BN}L_{BN}\frac{\Delta T_1}{\Delta t} \\
\frac{T_1-T_2}{R_1} - k_W\frac{T_2-T_3}{L_W} &= \frac{\rho_W c_W L_W}{2}\frac{\Delta T_2}{\Delta t} \\
k_W\frac{T_2-T_3}{L_W} - \frac{T_3-T_4}{R_2} &= \frac{\rho_W c_W L_W}{2}\frac{\Delta T_3}{\Delta t} \\
\frac{T_3-T_4}{R_2} - k_{Cu}\frac{T_4-T_5}{L_{Cu}} &= \frac{\rho_{Cu}c_{Cu}L_{Cu}}{2}\frac{\Delta T_4}{\Delta t} \\
k_{Cu}\frac{T_4-T_5}{L_{Cu}} - h(T_5-T_a) &= \frac{\rho_{Cu}c_{Cu}L_{Cu}}{2}\frac{\Delta T_5}{\Delta t} + \sigma\varepsilon(T_5^4 - T_a^4)
\end{aligned} \tag{A.2}$$

In order to obtain a system of equations numerically stable for any combination of finite elements $\Delta t, \Delta x$, the so-called "implicit method" [24] was used to approximate the spatial and the time derivatives. All the derivatives on the left-hand side of the equations are approximated by using the "new" temperatures. In the absence of a non-linear radiation term, this leads to a tri-diagonal linear system. In order not to complicate the system too much while still taking into consideration the effects of radiation (which can be non-negligible in the temperature range of interest), we calculate the power lost via black body radiation by using the "old" temperature.

To simplify the equations, we introduce the adimensional Biot and Fourier [4] numbers:

$$
\begin{array}{l}
\frac{1}{F_{BN0}} = \frac{\rho_{BN} c_{BN} L_{BN} R_0}{\Delta t};\ \frac{1}{F_{W1}} = \frac{\rho_W c_W L_W R_1}{2\Delta t};\ \frac{1}{F_{W2}} = \frac{\rho_W c_W L_W R_2}{2\Delta t} \\
\frac{1}{F_{Cu2}} = \frac{\rho_{Cu} c_{Cu} L_{Cu} R_2}{2\Delta t};\ \frac{1}{F_{Cuh}} = \frac{\rho_{Cu} c_{Cu} L_{Cu}}{2h\Delta t} \\
B_{W1} = \frac{k_W R_1}{L_W};\ B_{W2} = \frac{k_W R_2}{L_W};\ B_{Cu2} = \frac{k_{Cu} R_2}{L_{Cu}};\ B_{Cuh} = \frac{k_{Cu}}{hL_{Cu}}
\end{array}
\tag{A.3}
$$

With these notations, the discretized heat equation becomes:

$$
\left[\begin{array}{c} \\ \\ A+I \\ \\ \\ \end{array} \right] * \begin{bmatrix} T_1 \\ T_2 \\ T_3 \\ T_4 \\ T_5 \end{bmatrix} = \begin{bmatrix} T_1(-\Delta t) + F_{BN0} T_0 + F_{BN0} \frac{R_0 P}{A} \\ T_2(-\Delta t) \\ T_3(-\Delta t) \\ T_4(-\Delta t) \\ T_5(-\Delta t) + F_{Cuh} T_a + F_{Cuh} \left(T_5^4(-\Delta t) - T_a^4 \right) \end{bmatrix}, \tag{A.4}
$$

where I is the unity matrix and A is given by:

$$
A = \begin{bmatrix}
F_{BN0}\left(1 + \frac{R_0}{R_1}\right) & -F_{BN0}\frac{R_0}{R_1} & 0 & 0 & 0 \\
-F_{W1} & F_{W1}\left(1 + B_{W1}\right) & -F_{W1}B_{W1} & 0 & 0 \\
0 & -F_{W2}B_{W2} & F_{W2}\left(1 + B_{W2}\right) & -F_{W2} & 0 \\
0 & 0 & -F_{Cu2} & F_{Cu2}\left(1 + B_{Cu2}\right) & -F_{Cu2}B_{Cu2} \\
0 & 0 & 0 & -F_{Cuh}B_{Cuh} & F_{Cuh}\left(1 + B_{Cuh}\right)
\end{bmatrix}. \tag{A.5}
$$

This is the "tri-diagonal" linear system that provides the discrete temperature distribution in the system as a function of time.

To calibrate the model, we use the Marquardt nonlinear fitting algorithm from ref. [5]. In our model (Eq. A.4) we fit for six parameters - three thermal resistance, the convection coefficient h and two parameters describing a temperature dependent heat capacity for the third layer ("sample") $c(T) = c_0 + c_1 T$.

A six-parameter non-linear fit is difficult to achieve even with a numerically stable model. To simplify the procedure, a "divide and conquer" strategy is adopted and the algorithm is separated into two fits with fever parameters each. To do this, we take advantage of a second thermocouple, measuring the temperature of the W block T_w. This can be identified with T_3 in the model - $T_3 = T_W$. Knowing this temperature allows a simpler fit, for only three parameters - the Fourier and Biot number for the Cu layer as well as a convection coefficient, by using a simple model, which only calculates the temperature distribution across the Cu layer by taking into account the readings of both thermocouples.

The finite difference model for the homogeneous heat equation (no heat source), describing the sample in contact with the W block at temperature T_W and the gaseous atmosphere at temperature T_a is described below.

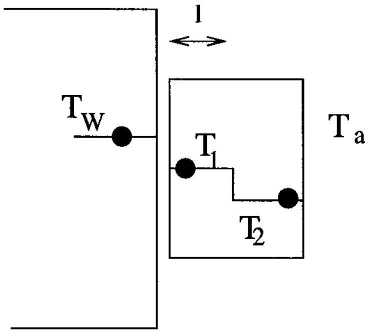

Fig. A.2 Model for the sample in contact with two interfaces. The thermal resistance R describes the contact with the W block and the convection coefficient h describes the interaction with the gaseous atmosphere held at "ambient temperature" T_a.

With the following notations for the system in Fig. A.2, k - thermal conductivity (Cu) - $\left[\frac{W}{mK}\right]$, c - specific heat (Cu) - $\left[\frac{J}{kgK}\right]$, ρ - density (Cu) - $\left[\frac{kg}{m^3}\right]$, R - thermal resistance (W-Cu interface) - $\left[\frac{Km^2}{W}\right]$, h - convection coefficient (Cu-air interface) - $\left[\frac{W}{m^2K}\right]$, the steady-state temperature distribution can be solved analytically if one neglects the radiation term:

$$\begin{array}{c} \frac{1}{R}(T_W - T_1) = k\frac{T_1 - T_2}{l} \\ k\frac{T_1 - T_2}{l} = h(T_2 - T_a) \end{array} \rightarrow \begin{array}{c} (1 + B_R)T_1 - B_R T_2 = T_W \\ -B_h T_1 + (1 + B_h)T_2 = T_a \end{array}. \tag{A.6}$$

Here, $B_h = \frac{k}{hl}$ and $B_R = \frac{kR}{l}$ are the Biot numbers for the two interfaces. The steady-state solution for the sample temperature (T_2) is:

$$T_{sam} = T_2 = \frac{B_h}{1 + B_h + B_R} T_W + \frac{1 + B_R}{1 + B_h + B_R} T_0. \tag{A.7}$$

The complete model, describing the time evolution of the sample temperature T_2 is,

$$\begin{cases} \frac{1}{R}(T_W - T_1) - k\frac{T_1 - T_2}{l} = \frac{\rho l c}{2\Delta t}(T_1 - T_1(-\Delta t)) \\ k\frac{T_1 - T_2}{l} - h(T_2 - T_0) - \sigma\varepsilon\left(T_2^4 - T_0^4\right) = \frac{\rho l c}{2\Delta t}(T_2 - T_2(-\Delta t)) \end{cases} \tag{A.8}$$

By defining the Fourier numbers $\frac{1}{F_R} = \frac{\rho l c R}{\Delta t}$; $\frac{1}{F_h} = \frac{\rho l c}{h\Delta t}$, and the Biot numbers $B_h =$

$\frac{k}{hl}$; $B_R = \frac{kR}{l}$, the equations can be written in a simpler form:

$$\begin{array}{l} (T_W - T_1) - B_R(T_1 - T_2) = \frac{1}{F_R}(T_1 - T_1(-\Delta t)) \\ B_h(T_1 - T_2) - (T_2 - T_0) - \frac{\sigma\varepsilon}{h}(T_2^4 - T_0^4) = \frac{1}{F_h}(T_2 - T_2(-\Delta t)) \end{array}, \tag{A.9}$$

$$\left\{ \begin{array}{l} (1 + F_R + F_R B_R)T_1 - F_R B_R T_2 = T_1(-\Delta t) + F_R T_W \\ -F_h B_h T_1 + (1 + F_h + F_h B_h)T_2 = T_2(-\Delta t) + F_h T_0 - F_h \frac{\sigma\varepsilon}{h}(T_2^4 - T_0^4) \end{array} \right. \tag{A.10}$$

Thus, the final set of equations describing the sample in contact with the W block through the thermal resistance R and in thermal contact with the gaseous atmosphere through the convection coefficient h, can be written in matrix form:

$$\begin{bmatrix} 1 + F_R + F_R B_R & -F_R B_R \\ -F_h B_h & 1 + F_h + F B_h \end{bmatrix} \begin{bmatrix} T_1 \\ T_2 \end{bmatrix} = \begin{bmatrix} T_1(-\Delta t) + F_R T_W \\ T_2(-\Delta t) + F_h T_0 - F_h \frac{\sigma\varepsilon}{h}(T_2^4 - T_0^4) \end{bmatrix}. \tag{A.11}$$

With all the parameters in Eq. A.11 obtained from the nonlinear least-squares fitting procedure for the "simple model" (Fig. A.2), the "full model" (Eq. A.4) can now be used in order to fit the remaining parameters. This procedure has been successfully applied to obtain least-squares fits such the one shown in Fig. 3.11.

Appendix B

Scattering Geometry

The geometry of the X-ray spectrometer used to study the order-disorder phase transition in Cu_3Au is shown in Fig. B.1. In the Cartesian coordinate system shown in the figure, the incident X-ray beam, $\mathbf{k}$ comes in the $-\mathbf{y}$ direction. The scattering angle is $\widehat{\mathbf{k},\mathbf{k}'} = 2\theta$ and the scattering plane $(\mathbf{k}, \mathbf{k}')$ makes an angle of χ with the horizontal plane $(\mathbf{y}, \mathbf{z})$. The sample was cut to expose the (100) surface, which is perpendicular to the scattering plane and makes an angle θ with both the incident $(\mathbf{k})$ and the scattered $(\mathbf{k}')$ waves. The orientation of the $(0k0)$ and $(00l)$ axes was not determined but this is not important because the reciprocal space of the Cu_3Au structure is symmetric with respect to the $(h00)$ axis. Here, the $(0l0)$ direction in reciprocal space has been assumed to lie in the $(\mathbf{x}, \mathbf{y})$ plane only to be able to calculate the magnitude of the transverse projection of scattering vectors $q_\perp = \sqrt{l^2 + k^2}$ which doesn't depend on the exact orientation of the $(0k0)$ and $(00l)$ vectors.

The energy of the X-ray photons used in the experiments described in this thesis is E=7.66keV, which corresponds to a wavelength of λ=1.61Å or wavevector k_0=3.9 Å^{-1}. The centre of the [100] peak in Cu_3Au was found at an angle $2\theta = 24.48°$, which corresponds to a scattering wavevector $q_0 = 2k_0\sin\theta \cong 2k_0\sin(12.24°) = 1.6565$ Å^{-1}.

The area detector is placed at a distance R_0 from the scattering centre. A point on the CCD detector is determined by the vector $\overrightarrow{R_f}$:

$$\overrightarrow{R_f} = \overrightarrow{R}_0 + u\widehat{U} + r\widehat{R}. \tag{B.1}$$

Here, $\overrightarrow{R_0}$ is the vector pointing to the centre of the detector and $u\widehat{u} + r\widehat{r}$ is the vector pointing from the centre of the detector to the point. The coordinates of a point on a

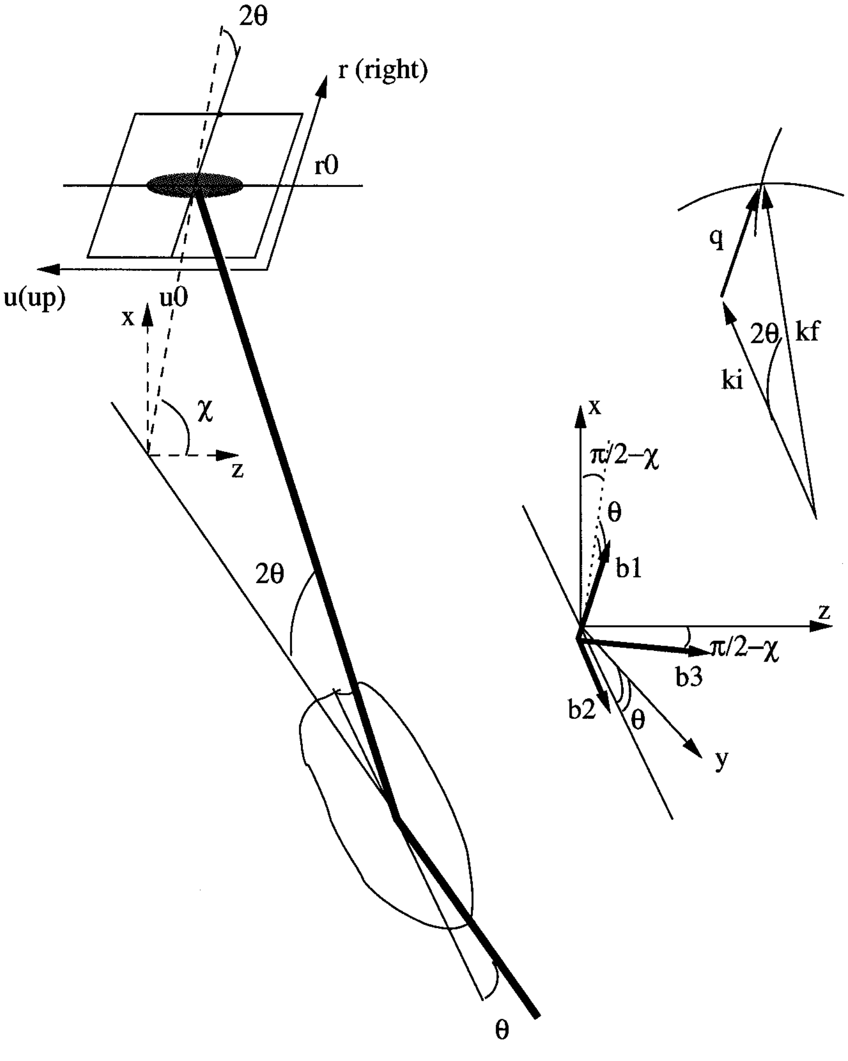

Fig. B.1 Geometry of the X-ray spectrometer.

detector are determined by the coordinates u along the "up" axis and r along the "right" axis, $\widehat{u}$ and $\widehat{r}$ being the unit vectors along these directions.

With these notations, the Cartesian coordinates of the unit vectors along the $\overrightarrow{r}$, $\overrightarrow{u}$ and $\overrightarrow{R_0}$ directions can be written

$$\begin{aligned} \widehat{r} = & \ [cos2\theta sin\chi, sin2\theta, cos2\theta cos\chi] \\ \widehat{u} = & \ [cos\chi, 0, -sin\chi] \\ \widehat{R_0} = & \ [sin2\theta sin\chi, -cos2\theta, sin2\theta cos\chi] \end{aligned} \quad . \tag{B.2}$$

From here, the unit vector in the scattering direction $\overrightarrow{R_f}$ can be written as

$$\widehat{R}_f = \frac{R_0}{R_f}\begin{bmatrix} sin2\theta\, sin\chi \\ -cos2\theta \\ sin2\theta\, cos\chi \end{bmatrix} + \frac{\Delta u}{R_f}\begin{bmatrix} cos\chi \\ 0 \\ -sin\chi \end{bmatrix} + \frac{\Delta r}{R_f}\begin{bmatrix} cos2\theta\, sin\chi \\ sin2\theta \\ cos2\theta\, cos\chi \end{bmatrix}, \tag{B.3}$$

where R_f is given by $R_f = \sqrt{R_0^2 + u^2 + r^2}$. In the xyz coordinate system, the incoming photons have a wavevector

$$\overrightarrow{k}_i = \frac{2\pi}{\lambda}[0, -1, 0], \tag{B.4}$$

while the photons scattered elastically in the $\overrightarrow{R_f}$ directions, are characterized by a wavevector $\overrightarrow{k_f}$ given by

$$\overrightarrow{k}_f = \frac{2\pi}{\lambda}\widehat{R}_f \tag{B.5}$$

From here, the scattering wavevector becomes

$$\overrightarrow{k}_f - \overrightarrow{k}_i = \frac{2\pi}{\lambda R_f}\begin{bmatrix} R_0 sin2\theta sin\chi + r cos2\theta sin\chi + u cos\chi \\ R_f - R_0 cos2\theta + r sin2\theta \\ R_0 sin2\theta cos\chi + r sin2\theta cos\chi - u sin\chi \end{bmatrix} . \tag{B.6}$$

A rotation by an angle θ about the Oz axis followed by a rotation by an angle χ about the Oy axis will yield the reciprocal-space coordinates of the scattering vector:

$$\begin{pmatrix} cos\theta & sin\theta & 0 \\ -sin\theta & cos\theta & 0 \\ 0 & 0 & 1 \end{pmatrix} \begin{pmatrix} sin\chi & 0 & cos\chi \\ 0 & 1 & 0 \\ -cos\chi & 0 & sin\chi \end{pmatrix} \begin{pmatrix} q_x \\ q_y \\ q_z \end{pmatrix} = 2\pi \frac{2sin\theta}{\lambda} \begin{pmatrix} q_1 \\ q_2 \\ q_3 \end{pmatrix} \tag{B.7}$$

The reciprocal space components expressed in reciprocal lattice units (rlu) (i.e. scattering vector in units of $\frac{2\pi}{a}$, with a being the lattice constant) can be seen in Fig. B.2 for two rows of pixels on the CCD detector, along the "right" (horizontal lines) and "up" (vertical lines) directions. As it can be seen, a horizontal scan provides a "quasi-radial" scan, in the sense that the reciprocal component q_1 is varying by almost an order of magnitude more than the q_2 component, while the third, q_3 component is practically constant. A vertical scan through the CCD detector provides a transverse scan in reciprocal space. The only non-constant component during such a scan is q_3.

The "q per pixel" factor resulting from either radial or transverse scans is of 6.86×10^{-5} Å^{-1}/pixel. This value was used in all the calculations presented in this thesis.

Example Centre of the scattering peak: $u = 0$, $r = 0$, $R_f = R_0$, with the angle $\chi = \pi/2$:

$$\overrightarrow{k}_f - \overrightarrow{k}_i = \frac{2\pi}{\lambda} \left[sin(2\theta), 1 - cos(2\theta), 0\right], \tag{B.8}$$

which, in reciprocal space, becomes:

$$\frac{2\pi}{\lambda} \begin{pmatrix} cos\theta & sin\theta & 0 \\ -sin\theta & cos\theta & 0 \\ 0 & 0 & 1 \end{pmatrix} \begin{pmatrix} sin(2\theta) \\ 1 - cos(2\theta) \\ 0 \end{pmatrix} = 2\pi \frac{2sin\theta}{\lambda} \begin{pmatrix} 1 \\ 0 \\ 0 \end{pmatrix} = \frac{2\pi}{a} \begin{pmatrix} 1 \\ 0 \\ 0 \end{pmatrix} \tag{B.9}$$

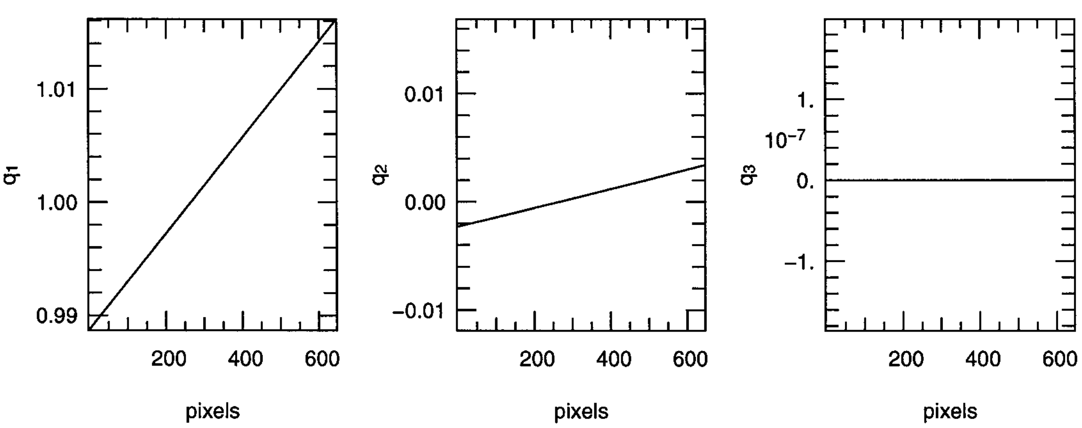

Radial scans (horizontal lines on the CCD detector)

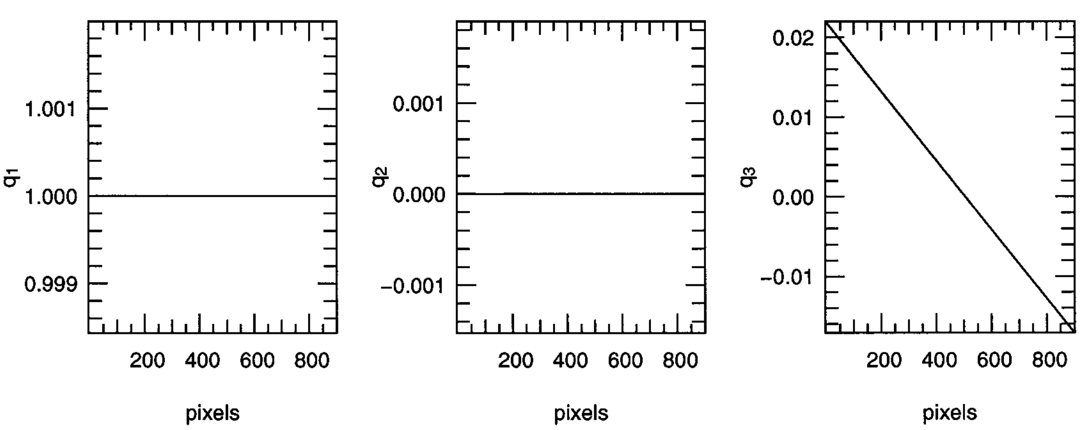

Transverse scans (vertical lines on the CCD detector)

Fig. B.2 Components of the scattering vector (q_1, q_2, q_3) along horizontal (first row) and vertical (second row) rows of pixels passing through the center of the [100] superlattice peak.

References

[1] Jens Als-Nielsen. *Elements of Modern X-ray Diffraction.* John Wiley & Sons, Inc., New York, 2002.

[2] Z. Altounian, Tu Guo-hua, and J.O. Strom-Olsen. Crystallization characteristics of ni-zr metallic glasses from ni20zr80 to ni70zr30. *J. Appl. Phys.*, 54:3111, 1983.

[3] N.W. Ashcroft and N.D. Mermin. *Solid State Physics.* Saunders College, Philadelphia, 1976.

[4] Adrian Bejan. *Heat Transfer.* John Wiley & Sons, Inc., 1993.

[5] P.R. Bevington. *Data Reduction and Error Analysis for the Physical Sciences.* McGraw Hill, 1969.

[6] M. Born and E. Wolf. *Principles of Optics.* Pergamon, Oxford, 1970.

[7] S. Brauer, G.B. Stephenson, M. Sutton, R. Brüning, E. Dufresne, S.G.J. Mochrie, G. Grübel, J. Als-Nielsen, and D.L. Abernathy. X-ray intensity fluctuation spectroscopy observations of critical dynamics in Fe_3Al. *Phys. Rev. Lett.*, 74:2010–2013, 1995.

[8] S.F. Brauer. *The kinetics of rapid crystallization of metallic glasses.* PhD thesis, McGill University, 1992.

[9] G. Brown, P.A. Rikvold, M. Sutton, and M. Grant. Speckle from phase-ordering systems. *Phys. Rev. E*, 56:6601, 1997.

[10] G. Brown, P.A. Rikvold, M. Sutton, and M. Grant. Evolution of speckle during spinodal decomposition. *Phys. Rev. E*, 60:5151, 1999.

[11] B.D. Butler and J.B. Cohen. The structure of Cu_3Au above the critical temperature. *J. Appl. Phys.*, 65:2214, 1989.

[12] Z.H. Cai, B. Lai, W.B. Yun, and I. McNulty. Observation of X-ray speckle by coherent scattering at grazing incidence. *Phys. Rev. Lett.*, 73:82–85, 1994.

[13] P.M. Chaikin and T.C. Lubensky. *Principles of Condensed Matter Physics.* Cambridge University Press, Cambridge, 1995.

[14] B. Chu. *Laser Light Scattering: Basic Principles and Practice.* Academic Press, Boston, Toronto, second edition, 1991.

[15] R. Coïsson. Spatial coherence of synchrotron radiation. *Appl. Optics*, 34:904–908, 1995.

[16] S.B. Dierker, R. Pindak, R.M. Fleming, I.K. Robinson, and L. Berman. X-ray photon correlation spectroscopy study of Brownian motion of gold colloids in glycerol. *Phys. Rev. Lett.*, 75:449–452, 1995.

[17] H. Dosch, L. Mailänder, H. Reichert, and J. Peisl. Long-range order near the $Cu_3Au(001)$ surface by evanescent X-ray scattering. *Phys. Rev. B*, 43:13172–13186, 1991.

[18] E. Dufresne. *Intensity Fluctuation Spectroscopy with Coherent X-rays.* PhD thesis, McGill University, 1995.

[19] Eric M. Dufresne, Teamour Nurushev, Roy Clarke, and Steven B. Dierker. Concentration fluctuations in the binary mixture hexane-nitrobenzene with static and dynamic x-ray scattering. *Phys. Rev. E*, 65:061507, 2002.

[20] K. Dutton, S. Thompson, and B Barraclough. *The Art of Control Engineering.* Addison-Wesley, 1997.

[21] Dennis Millis (ed.). *Third-Generation Hard X-Ray Synchrotron Radiation Sources: Source Properties, Optics, and Experimental Techniques.* John Wiley & Sons, Inc., New York, 2002.

[22] Andrei Fluerasu and Mark Sutton. Linux driver for the keithley kpci 3108 i/o card. Technical report, Centre for the Physics of Materials, McGill, March 2001. (internal document).

[23] Andrei FLuerasu and Mark Sutton. Kalman-predictive-proportional-integral-derivative temperature control. In *Temperature Symposium 2002*, 2002.

[24] Cezar Fluerasu. *Electrotermie.* Polytechnic University Bucharest, 1990.

[25] N. Goldenfeld. *Lectures on Phase Transitions and the Renormalization Group.* Addison-Wesley Publishing, New York, 1992.

[26] J.W. Goodman. *Statistical Optics.* John Wiley & Sons, Inc., New York, first edition, 1985.

[27] Martin Grant. Non equilibrium statistical mechanics. Technical report, Centre for the Physics of Materials, McGill, Summer 2002. (course notes).

[28] Sol M. Gruner, Mark W. Tate, and Eric F. Eikenberry. Chrage-coupled device area x-ray detectors. *Rev. Sci. Instrum.*, 73:2815–2842, 2002.

[29] J.D. Gunton, M. San Miguel, and P.S. Sahni. The dynamics of first-order phase transitions. In C. Domb and J.L Lebowitz, editors, *Phase Transitions and Critical Phenomena*, volume 8, pages 267–467. Academic Press, London, 1983.

[30] T. Hashimoto, K. Nishimura, and Y. Takeuchi. Dynamics of transitional ordering process in Cu_3Au alloy from disordered state to ordered state. *J. Phys. Soc. Jpn.*, 45:1127–1135, 1978.

[31] P.C. Hohenberg and B.I. Halperin. Theory of dynamic critical phenomena. *Rev. Mod. Phys.*, 49:435, 1977.

[32] R.F. Shannon Jr, C.R. Harkless, and S.E. Nagler. Effect of extra Cu on ordering kinetics in thin films of Cu_3Au. *Phys. Rev. B*, 38:9327, 1988.

[33] R.F. Shannon Jr., S.E. Nagler, C.R. Harkless, and R. M. Nicklow. Time-resolved X-ray scattering study of ordering kinetics in bulk single-crystal Cu_3Au. *Phys. Rev. B*, 46:40–53, 1992.

[34] Hyunjung Kim, A. Rhm, L. B. Lurio, J. K. Basu, J. Lal, D. Lumma, S. G. J. Mochrie, and S. K. Sinha.

[35] C. Kittel. *Introduction to Solid State Physics.* John Wiley & Sons, Inc., New York, sixth edition, 1986.

[36] Z. W. Lai. Theory of ordering dynamics for $\mathrm{cu}_3\mathrm{au}$. *prb*, 41:9239, 1990.

[37] B. Lengeler. Coherence in x-ray physics. *Naturwissenschaften*, 88:249–260, 2001.

[38] F. Livet, F. Bley, R. Caudron, E. Geissler, D. Abernathy, C. Detlefs, G. Grübel, and M. Sutton. Kinetic evolution of unmixing in an alli alloy using x-ray intensity fluctuation spectroscopy. *Phys. Rev. E*, 63:36108, 2001.

[39] F. Livet, F. Bley, J. Mainville, R. Caudron, S. G. J. Mochrie, E. Geissler, G. Dolino, D. Abernathy, G. Grübel, and M. Sutton.

[40] K.F. Ludwig, Jr., G.B. Stephenson, J.L. Jordan-Sweet, J. Mainville, Y.S. Yang, and M. Sutton. Nucleated and continous ordering in $\mathrm{Cu}_3\mathrm{Au}$. *Phys. Rev. Lett.*, 61:1859, 1988.

[41] L.B. Lurio, D. Lumma, P. Falus, M.A. Borthwick, S.G.J. Mochrie, J.F. Pelletier, M. Sutton, L. Regan, A. Malik, and G.B. Stephenson. Absence of scaling ... *Phys. Rev. Lett.*, 84:785, 2000.

[42] Anders Madsen, Jens Als-Nielsen, and Gerhard Grübel. Viscosity of a liquid cryststal near the nematic-smectic a phase transition. *Phys. Rev. Lett.*, 90:085701.

[43] Anders Madsen, Oleg Konovalov, Aymeric Robert, and Gerhard Grübel. Surface ordering in a concentrated suspension of colloidal particles investigated by x-ray scattering methods. *Phys. Rev. E*, 64:061406, 2001.

[44] A. Malik, A.R. Sandy, L.B. Lurio, G.B. Stephenson, S.G.J. Mochrie, I. McNulty, and M. Sutton. Coherent x-ray study of fluctuations during domain coarsening. *Phys. Rev. Lett.*, 81:5832, 1998.

[45] P. Maybeck. *Stochastic Models, Estimation, and Control*, volume 1. Academic Press, Inc., 1000.

[46] J. Miao, P. Charalambous, J. Kirz, and D. Sayre. Extending the methodology of x-ray crystallography to allow imaging of micrometre-sized non-crystalline specimens. *Nature*, 400:342.

[47] J. Miao, K. O. Hodgson, and D. Sayre. An approach to three-dimensional structures of biomolecules by using single-molecule diffraction images. *Proc. Nat. Acad. Sci.*, 98:6641.

[48] S. G. J. Mochrie, A. M. Mayes, A.R. Sandy, M. Sutton, S. Brauer, G.B. Stephenson, D. L. Abernathy, and G. Grübel. Dynamics of block copolymer micelles revealed by x-ray intensity fluctuation spectroscopy. *Phys. Rev. Lett.*, 78:1275, 1997.

[49] S.E. Nagler, R.F. Shannon, Jr., C.R. Harkless, and M.A. Singh. Time-resolved X-ray scattering study of ordering and coarsening in Cu_3Au. *Phys. Rev. Lett.*, 61:718–721, 1988.

[50] Y. Noda, S. Nishihara, and Y. Yamada. Critical behavior and scaling law in ordering process of the first order phase transistion in Cu_3Au alloy. *J. Phys. Soc. Jpn.*, 53:4241–4249, 1984.

[51] J. F. Pelletier, M. Sutton, Z. Altounian, S. Saini, L. B. Lurio, A. R. Sandy and. Lumma, M. A. Borthwick, P. Falus, S. G. J. Mochrie, and G. B. Stephenson. A time-resolved x-ray scattering spectrometer to study phase transitions and crystallization processes in metallic alloys. *AIP Conf. Proc.: SRI99: 11th US National Synchrotron Radiation Instrumentation, P. Pianetta, J. Arthur, and S. Brennan, eds.*, 521:188, 2000.

[52] W. H. Press, S. A. Teukolsky, W. T. Vettering, and B. P. Flannery. *Numerical Recipes in C.* Cambridge University Press, Cambridge, second edition, 1992.

[53] P.N. Pusey. Statistical properties of scattered radiation. In H.Z. Cummins and E.R. Pike, editors, *Photon Correlation Spectroscopy and Velocimetry*, page 45. Plenum, New York, 1977.

[54] H. Reichert, P.J. Eng, H. Dosch, and I.K. Robinson. Thermodynamics of surface segregation profiles at $Cu_3Au(001)$ resolved by X-ray scattering. *Phys. Rev. Lett.*, 74:2006, 1995.

[55] I. K. Robinson, I. A. Vartanyants, G. J. Williams amd M. A. Pfeifer, and J. A. Pitney. Reconstruction of the shapes of gold nanocrystals using coherent x-ray diffraction. *Phys. Rev. Lett.*, 87:195505, 2001.

[56] R.B. Rogge, B.D. Gaulin, E.C. Svensson, E.D. Hallman, and W. Wei. Neutron scattering near the order-disorder transition in cu_3au: Evidence for a lower spinodal temperature. *Can. J. Phys.*, 73:779–791, 1995.

[57] Irakli Sikharulidze, Igor P. Dolbnya, Andrea Fera, Anders Madsen, Boris Ostrovskii, and Wim H. de Jeu. Smectic membranes in motion: Approaching the fast limits of x-ray photon correlation spectroscopy. *Phys. Rev. Lett.*, 88:115503.

[58] S. K. Sinha, M. Tolan, and A. Gibaud. Effects of partial coherence on the scattering of x rays by matter. *Phys. Rev. B*, 57:2740, 1998.

[59] G.B. Stephenson. photodiode linear psd detector. *Nucl. Inst. and Meth. A*, 266:447, 1988.

[60] M. Sutton, S.G.J Mochrie, T. Greytak, S.E. Nagler, L.E. Berman, G.A. Held, and G.B Stephenson. Observation of speckle by diffraction with coherent x-rays. *Nature*, 352:608, 1991.

[61] Mark Sutton. Coherent x-ray diffraction. In Dennis Millis, editor, *Third-Generation Hard X-Ray Synchrotron Radiation Sources: Source Properties, Optics, and Experimental Techniques.* John Wiley & Sons, Inc., New York.

[62] Eugene M. Terentjev. Soft matter dynamics: Searching for equilibrium. *Nature Materials*, 1:149–150, 2002.

[63] T. Thurn-Albrecht, W. Steffen, A. Patkowski, G. Meier, E. W. Fischer, G. Grubel, and D. L. Abernathy. Photon correlation spectroscopy of colloidal palladium using a coherent x-ray beam. *Phys. Rev. Lett.*, 77:5437, 1996.

[64] B.E. Warren. *X-Ray Diffraction.* Dover Publications, Inc., New York, 1990.